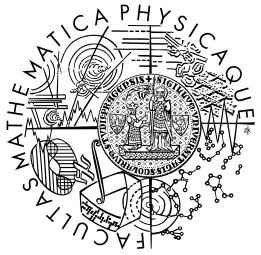

FACULTY
OF MATHEMATICS
AND PHYSICS
Charles University

DOCTORAL THESIS

Martin Váňa

A model of resonant collisions of electrons with molecules and molecular ions

Institute of Theoretical Physics

Supervisor of the doctoral thesis: RNDr. Karel Houfek Ph.D
Study programme: Physics
Study branch: Theoretical Physics

Prague 2017

I declare that I carried out this doctoral thesis independently, and only with the cited sources, literature and other professional sources.

I understand that my work relates to the rights and obligations under the Act No. 121/2000 Sb., the Copyright Act, as amended, in particular the fact that the Charles University has the right to conclude a license agreement on the use of this work as a school work pursuant to Section 60 subsection 1 of the Copyright Act.

In ..... date ..... signature of the author

Title: A model of resonant collisions of electrons with molecules and molecular ions

Author: Martin Váňa

institute: Institute of Theoretical Physics

Supervisor: RNDr. Karel Houfek Ph.D , Institute of Theoretical Physics

Abstract:

A two-dimensional model of the resonant electron-molecule collision processes with one nuclear and one electronic degree of freedom introduced by Houfek, Rescigno and McCurdy [Phys. Rev. A **73**, 032721 (2006)] and a similar two-dimensional model of the dissociative recombination with potential proposed by Hamilton [Ph.D. thesis, University of Colorado, (2003)] are formulated within the time-dependent framework and solved numerically using the finite-element method with the discrete variable representation basis, the exterior complex scaling method and the generalized Crank-Nicolson method. On the model of electron-molecule collisions we illustrate how the time-dependent calculations can provide a deep insight into the origin of oscillatory structures in the vibrational excitation cross sections if one evaluates the cross sections not only at sufficiently large time to obtain the final cross sections, but rather at several characteristic times which are given by the evolution of the system. With use of the time-dependent calculations we demonstrate the complex nature of the dissociative recombination model dynamics and we propose the interpretation of the recombination process mechanism. We also propose few techniques for explanation of the sharp structures in the dissociative recombination cross sections and we study the populations of its final states for the first time in theoretical calculations. Numerical results are presented for N_2-like, NO-like, and F_2-like models of the electron-molecule collisions and H_2^+-like model of the dissociative recombination. The results are compared with ones obtained within time-independent approach and in the electron-molecule case also within the local complex potential approximation.

Keywords: electron-molecule collisions resonance molecular ions vibrational excitation dissociative attachment dissociative recombination

I would like to thank my suprevisor RNDr. Karel Houfek Ph.D. for his guidance and the tremendous amount of time and energy invested in this research. I would also like to thank Mgr. Roman Čurík Ph.D. for his countless advises, Mgr. David Hvizdoš for his collaboration on the time-independent calculations, doc. RNDr. Martin Čížek Ph.D. for occasional help with general theory and coleagues Mgr. Jiři Eliášek Ph.D. and Mgr. Anton Khirnov for their advisory in the area of programming. Last but not least I would like to thank the Institute of Theoretical Physics for supporting this research.

I would like to dedicate this thesis to my family, especially to my wife and to my father.

Contents

Introduction

In the recent decades a demand for the estimation of accuracy and validity of theoretical predictions arose from the scientific community, e.g. pubulished by Editors [2011]. Such a demand is quite reasonable in the domain of atomic and molecular physics. Since the dynamics in systems larger than a simple hydrogen atom leads to a many-body Schrödinger equation, only the approximative techniques may be applied to obtain the theoretical predictions. The eventual disagreement of the theoretical predictions with the experimental results often originates from the inaccuracy or even invalidity of the approximations used in the calculation.

In the paper Houfek et al. [2006], a simple two-dimensional model of resonant electron collisions with diatomic molecules was introduced to study in detail validity of various approximate approaches for treating the nuclear dynamics that plays an important role during these collisions, especially if one is interested in processes such as vibrational excitation (VE) of a molecule by an electron impact

$$\mathrm{e}^- + \mathrm{AB}(v_i) \;\rightarrow\; \mathrm{e}^- + \mathrm{AB}(v_f)\,, \tag{1}$$

and dissociative electron attachment (DA)

$$\mathrm{e}^- + \mathrm{AB}(v_i) \;\rightarrow\; \mathrm{A} + \mathrm{B}^-\,. \tag{2}$$

The model has two degrees of freedom, the internuclear distance R and the electron distance r, with the potential energy chosen in such a way to reproduce qualitatively the complex potential energy curve of a certain negative molecular ion when fixed-nuclei calculations are performed. Three models for the molecules N_2, NO, and F_2 were constructed in Houfek et al. [2006] and Houfek et al. [2008a]. The validity of the local complex potential (LCP) approximation to the nuclear dynamics for these three systems was discussed in Houfek et al. [2006] and the more elaborate nonlocal theory of the nuclear dynamics Domcke [1991] was considered later in Houfek et al. [2008a]. It was shown that the nonlocal theory is much more accurate than the local complex potential approximation and works well for all three studied systems.

In papers Houfek et al. [2006] and Houfek et al. [2008a], the time-independent approach was used to solve the two-dimensional model of the electron-molecule collisions and to calculate the cross sections of the processes (1) and (2) within the full model and also within the LCP and nonlocal approximations.

A similar two-dimensional model can be constructed for low-energy collisions of electrons with hydrogen cations H_2^+ using the potentials introduced by Hamilton [2003]. The potentials were originally intended for modelling the dynamics of *photoionization* and *photodissociation* processes using the two-dimensional R-matrix calculation. It was later suggested by C.W. McCurdy, T.N. Rescigno and C.H. Greene [personal communication, 2008] that these potentials could be also used for a model of the dissociative recombination (DR) process

$$\mathrm{e}^- + \mathrm{AB}^+(v_i) \;\rightarrow\; \mathrm{A} + \mathrm{B}\,, \tag{3}$$

and possibly also the vibrational excitation process similar to (1). The model has the same degrees of freedom and it differs from the electron-molecule collision

model, apart from the shape of the interaction potential, in the presence of the long-range Coulomb interaction between the electron and the hydrogen molecular cation. This dissociative recombination model was solved in collaboration with Hvizdoš [2016] in the time-independent approach to the model dynamics. As in the electron-molecule case this model can be also used for testing the approximations, e.g. the *frame transformation* (Chang and Fano [1972]) method based on the *quantum defect theory*. By its design the model of dissociative recombination enables to distinguish the final states in the possible recombination channels, which is unlike any other theory of dissociative recombination. For more details on the dissociative recombination see e.g. Florescu-Mitchell and Mitchell [2006] or Larsson and Orel [2008].

The goal of this thesis is to solve the two-dimensional problem for both the electron-molecule collisions model and the model of dissociative recombination using the time-dependent approach to get a deeper insight into the dynamics of the processes (1) and (2) in the electron-molecule case and (3) in the recombination model of H_2^+. We also compare the results of the time-dependent approach to the model dynamics of electron-molecule collision with the time-dependent LCP approximation.

We should note that time-dependent calculations for the same two-dimensional model of electron-molecule collisions were performed also by Shandilya et al. [2012] but their cross sections disagree with the previous results of the time-independent calculations. For example, the structures in the VE cross sections are much narrower than they should be (see Fig. 3.7). We should stress here that both the time-dependent and time-independent approaches in the quantum mechanics are equivalent for systems with the time-independent Hamiltonian. If a given problem is in both approaches formulated consistently and solved properly the final results (the cross sections in our case) must be the same as it is demonstrated in this thesis. Therefore, we disagree with the claim of Shandilya et al. [2012] that "these features [narrower oscillatory structures in the VE cross sections] could be genuine and fresh experiments with better resolution are required to settle this issue". Furthermore, the 2D model introduced in Houfek et al. [2006] was not developed and constructed for direct comparison with experiments although the cross sections obtained from the 2D model resemble the experimental ones.

The results of the time-dependent calculations enabled us to discuss in details the origin of structures in the VE cross sections of the electron-molecule collisions. In the literature, see e.g. Domcke [1991], Čurík and Čársky [2012] and references therein, the cross sections are usually obtained within the time-independent framework and an explanation of the origin of these features is very often provided only within the *boomerang* model by Herzenberg [1968], Birtwistle and Herzenberg [1971], Dubé and Herzenberg [1979]. This simple model assumes that the *boomerang* structures in the cross sections result from the interference of two processes, a direct decay of the resonant state of the negative molecular ion without nuclear motion and a time-delayed release of the electron after one vibrational motion of the nuclei. But such interference leads to a very regular interference pattern in the VE cross sections and for a full explanation of details of these structures, especially of highly asymmetrical peaks, it is necessary to consider interference of several processes due to repeated vibrational motion. Within the time-independent picture the detailed discussion of the resulting cross sec-

tions can be sometimes quite complicated Houfek et al. [2008b]. Here we propose a simple method how to determine the origin of these features which is based on comparing the cross sections with contributions integrated up to a certain distinctive time given by the dynamics of the system, in this case after each period of the vibrational motion of the negative molecular ion, as discussed in the Sec. 3.4. The results of the time-dependent approach to the dynamics of electron-molecule collisions model along with the interpretation of the cross section structures were also published in Váňa and Houfek [2017].

Another goal of this thesis is to calculate the cross sections of the individual dissociative recombination channels. Currently there is no other theory which allows to distinguish the final states of the dissociative recombination from each other and calculating their populations. However in general experiments such populations are already being measured, e.g. measurements of the dissociative recombination with LiH^+ by Krohn et al. [2001].

As in papers Houfek et al. [2006] and Houfek et al. [2008a] we give all relations and values in tables and figures in atomic units, in which

$$\hbar = m_e = e = \frac{1}{4\pi\epsilon_0} = 1. \tag{4}$$

Internuclear distances are given in units of the Bohr radius $a_0 = 5.291\,772 \times 10^{-11}$ m, cross sections in units of $a_0^2 = 2.800\,285 \times 10^{-21}$ m^2, and energies in units of hartrees, where 1 hartree $= 4.359\,748 \times 10^{-18}$ J. The atomic unit of time is 1 a.u. $= 2.418\,884 \times 10^{-17}$ s $\simeq 0.024$ fs.

1. Theoretical background

This chapter contains a few notes on the general scattering theory, a detailed description of presented models, their solutions in both time-dependent and time-independent approaches and a brief description of an approximative method used for comparison with the electron-molecule collision model.

1.1 Multichannel scattering

Before introducing the models we summarize a few important relations from the general scattering theory. The purpose of this section is simply to provide a solid background to relations presented later in the text. For further details see e.g. Taylor [1991].

If we start with a system consisting of two or more subsystems with some internal degrees of freedom, then the process of scattering may be generally formulated as mapping of some initial state of the system, where subsystems are separated, to a set of possible final states, for example

$$\begin{aligned} \mathrm{AB} + \mathrm{C} &\longrightarrow \mathrm{AB}^* + \mathrm{C}, \\ &\longrightarrow \mathrm{AC} + \mathrm{B}, \\ &\longrightarrow \mathrm{A} + \mathrm{B} + \mathrm{C}, \\ &\quad \ldots \text{ etc.} \end{aligned} \tag{1.1}$$

where the A, B, C stand as labels of system components. In the following text we will confine ourselves to cases where only two subsystems are present in the initial and all of the final states. The initial and final states are labeled by channels and we assume that they are asymptotically described by their channel Hamiltonians H_0^γ, where γ labels the channel. We denote the initial state as $|\psi_{\mathrm{in}}^\alpha\rangle$, where α denotes the chosen initial channel. If there would be no interaction between subsystems, the evolution of the state in the channel α would be provided by the evolution operator $U_0^\alpha(t)$ derived from the unperturbed Hamiltonian H_0^α as

$$U_0^\alpha(t) = e^{-iH_0^\alpha t} \tag{1.2}$$

To any initial state $|\psi_{\mathrm{in}}^\alpha\rangle$ at $t = 0$ in the channel α corresponds the actual physical state $|\psi_\alpha^+\rangle$ at $t = 0$ which may be produced by evolving the initial state backwards in time by the channel evolution operator $U_0^\alpha(t)$ and then evolving it back by the evolution operator $U(t)$ derived from the full problem Hamiltonian H,

$$|\psi_\alpha^+\rangle = \lim_{t\to-\infty} U^\dagger(t)U_0^\alpha(t)|\psi_{\mathrm{in}}^\alpha\rangle, \tag{1.3}$$

Similarly we can define the actual physical state $|\psi_\beta^-\rangle$ for any final state $|\psi_{\mathrm{out}}^\beta\rangle$ in the final channel β. We define the Møller operators as

$$\Omega_\pm^\gamma = \lim_{t\to\pm\infty} U^\dagger(t)U_0^\gamma(t) = \lim_{t\to\pm\infty} e^{iHt}e^{-iH_0^\gamma t}. \tag{1.4}$$

The Møller operators are isometric

$$\Omega_\pm^{\gamma\dagger}\Omega_\pm^\gamma = 1, \tag{1.5}$$

and in the absence of bound states also unitary (see Taylor [1991])

$$\Omega_{\pm}^{\dagger} = \Omega_{\pm}^{-1}. \tag{1.6}$$

Starting with the initial energy eigenstates $|\psi_{\alpha,E}\rangle$ we can produce the actual states with energy E by

$$|\psi_{\alpha,E}^{\pm}\rangle = \Omega_{\pm}^{\gamma}|\psi_{\alpha,E}\rangle. \tag{1.7}$$

Crucial to the following text is the definition of the scattering operator

$$S_{\alpha\to\beta} = \Omega_{-}^{\beta\dagger}\Omega_{+}^{\alpha}, \tag{1.8}$$

and therefore

$$\langle\psi_{\beta,E}^{-}|\psi_{\alpha,E}^{+}\rangle = \langle\psi_{\beta,E}|\Omega_{-}^{\beta\dagger}\Omega_{+}^{\alpha}|\psi_{\alpha,E}\rangle = \langle\psi_{\beta,E}|S|\psi_{\alpha,E}\rangle, \tag{1.9}$$

with the elements of the S matrix satisfying (thanks to the conservation of energy)

$$\langle\psi_{\beta,E'}|\Omega_{-}^{\beta\dagger}\Omega_{+}^{\alpha}|\psi_{\alpha,E}\rangle = S_{\alpha\to\beta}(E)\delta(E-E'). \tag{1.10}$$

We should emphasize that all of the information about the scattering process is given by the $S_{\alpha\to\beta}(E)$ matrix elements.

1.2 Two-dimensional model of resonant electron molecule collisions

In this section we give a brief description of the two-dimensional model as it was introduced by Houfek et al. [2006] and Houfek et al. [2008a]. The model has two degrees of freedom, one nuclear R and one electronic r. Its full Hamiltonian reads

$$H = -\frac{1}{2\mu}\frac{\partial^2}{\partial R^2} - \frac{1}{2}\frac{\partial^2}{\partial r^2} + V(R,r), \tag{1.11}$$

where μ denotes the reduced molecular mass and $V(R,r)$ is the model potential

$$V(R,r) = V_0(R) + \frac{l(l+1)}{2r^2} + V_{\text{int}}(R,r), \tag{1.12}$$

where l denotes the electron angular momentum chosen to correspond to the incoming electron partial wave with the largest contribution to the cross section in a real system, $V_0(R)$ is the potential energy describing vibrational motion of the neutral molecule when the electron is at large distances, i.e.

$$V_0(R) = \lim_{r\to\infty} V(R,r), \tag{1.13}$$

and $V_{\text{int}}(R,r)$ describes the interaction between the two degrees of freedom given by two functions $\lambda(R)$ and $\alpha(R)$ as

$$V_{\text{int}}(R,r) = \lambda(R)e^{-\alpha(R)r^2}, \tag{1.14}$$

chosen to obtain various models each similar to a different real system. The molecular potential is approximated by the Morse potential

$$V_0(R) = D_0\left(e^{-2\alpha_0(R-R_0)} - 2e^{-\alpha_0(R-R_0)}\right), \tag{1.15}$$

where D_0 controls the depth of the potential well, α_0 its width and R_0 its position. The model does not consider rotational excitation of the molecule, thus no centrifugal barrier of the form $\frac{J(J+1)}{2\mu R^2}$ corresponding to the angular momentum quantum number J is present in the molecular potential, though it is straightforward to generalize the model to include them.

For three models introduced in Houfek et al. [2006] and Houfek et al. [2008a] it is not necessary to consider α as a function of R, thus we put

$$\alpha(R) = \alpha_c. \tag{1.16}$$

At last we specify the function $\lambda(R)$, which was chosen in such a way to have a bound electronic state for large internuclear distances R and a resonant state for small R. For all models investigated in this paper it has the following form

$$\lambda(R) = \lambda_\infty + \frac{\lambda_0}{1 + e^{\lambda_1(R-R_\lambda)}}, \tag{1.17}$$

$$\lambda_0 = (\lambda_c - \lambda_\infty)(1 + e^{\lambda_1(R_c-R_\lambda)}). \tag{1.18}$$

The parameter λ_∞ controls the potential as $R \to \infty$, the parameter λ_c determines the value of $\lambda(R)$ at the crossing point R_c of the potential curve $V_0(R)$ and the potential energy curve $E_{\mathrm{res}}(R)$ (see Eq. (1.63) below) corresponding to the internuclear distance where the resonant state becomes a bound state.

Table 1.1: Constants and potential parameters for the N_2-like, NO-like and F_2-like models given in atomic units, so that the resulting potential is in hartrees.

constant	N_2-like	NO-like	F_2-like
μ	12 766.36	13 614.16	17 315.99
l	2 (d-wave)	1 (p-wave)	1 (p-wave)
D_0	0.75102	0.2363	0.0598
α_0	1.15350	1.5710	1.5161
R_0	2.01943	2.1570	2.6906
λ_∞	6.21066	6.3670	18.8490
λ_1	1.05708	5.0000	3.2130
R_λ	-27.9833	2.0843	1.8320
λ_c	5.38022	6.0500	18.1450
R_c	2.40500	2.2850	2.5950
α_c	0.40000	1.0000	3.0000

1.2.1 Channel Hamiltonians and eigenstates

Before we introduce both the time-independent and time-dependent approaches to the model dynamics, it is convenient to introduce the unperturbed Hamiltonians for the vibrational excitation (VE) and dissociative attachment (DA) channels, which are

$$H_0^{\mathrm{VE}} = -\frac{1}{2}\frac{\partial^2}{\partial r^2} + \frac{l(l+1)}{2r^2} - \frac{1}{2\mu}\frac{\partial^2}{\partial R^2} + V_0(R), \tag{1.19}$$

$$H_0^{\mathrm{DA}} = -\frac{1}{2}\frac{\partial^2}{\partial r^2} - \frac{1}{2\mu}\frac{\partial^2}{\partial R^2} + V_{\mathrm{b}}(r), \tag{1.20}$$

where the potential $V_{\rm b}(r)$ is given by the limit

$$V_{\rm b}(r) = \lim_{R\to\infty} V(R,r). \tag{1.21}$$

The first Hamiltonian $H_0^{\rm VE}$ describes the system when the molecule is in a certain vibrational state and the electron is far from the molecule. The second Hamiltonian $H_0^{\rm DA}$ describes the system when the electron is attached to one component of the molecule and the components are far from each other.

As in Houfek et al. [2008a], we define the unperturbed energy-normalized ($E = k^2/2$) electronic continuum states with the angular momentum l as

$$\mathcal{J}_k^l(r) = \sqrt{\frac{2k}{\pi}} r j_l(kr), \tag{1.22}$$

where j_l is the spherical Bessel function of the first kind (see Abramowitz and Stegun [1972] for details), and the unperturbed energy-normalized ($E = K^2/2\mu$) molecular-anion continuum state as

$$\mathcal{E}_K(R) = \sqrt{\frac{2\mu}{\pi K}} \sin(KR). \tag{1.23}$$

The energy-normalized incident eigenstate of $H_0^{\rm VE}$ with the total energy $E = E_{v_i} + k_i^2/2$ is then given by

$$\varphi_{v_i}^{\rm in}(E,R,r) = \chi_{v_i}(R)\mathcal{J}_{k_i}^l(r), \tag{1.24}$$

where $\chi_{v_i}(R)$ is the initial vibrational state of the molecule, the solution of

$$\left(-\frac{1}{2\mu}\frac{\partial^2}{\partial R^2} + V_0(R)\right)\chi_{v_i}(R) = E_{v_i}\chi_{v_i}(R). \tag{1.25}$$

The energy-normalized outgoing eigenstate for the final vibrational state v_f is

$$\varphi_{v_f}^{\rm out}(E,R,r) = \chi_{v_f}(R)\mathcal{J}_{k_f}^l(r) \tag{1.26}$$

and the outgoing eigenstate in the DA channel with the total energy $E = E_{\rm b} + K^2/2\mu$ is

$$\varphi_{\rm DA}^{\rm out}(E,R,r) = \mathcal{E}_K(R)\phi_{\rm b}(r), \tag{1.27}$$

where $\phi_{\rm b}(r)$ denotes the electronic bound state in the potential $V_{\rm b}(r)$ (we currently assume there is only one such state which is true for all models of electron molecule collisions investigated in this thesis).

1.3 Time independent solution

With the Hamiltonian (1.11), the system e^-+AB at a given energy E is described by the solution of the Schrödinger equation

$$H\Psi_E^+(R,r) = E\Psi_E^+(R,r) \tag{1.28}$$

where $\Psi_E^+(R,r)$ satisfies appropriate boundary conditions. We are interested in vibrational excitation and dissociative attachment, and for these two processes the

initial state of the model system $\Psi^0_{v_\mathrm{i}}(R,r)$ is given by (1.24). To solve Eq. (1.28), we partition the full wave function, Ψ^+_E, into incident and scattered parts,

$$\Psi^+_E(R,r) = \Psi^0_{v_\mathrm{i}}(R,r) + \Psi_\mathrm{sc}(R,r)\,. \tag{1.29}$$

The unknown scattered part of the wave function, $\Psi_\mathrm{sc}(R,r)$, then satisfies a driven Schrödinger equation

$$(E-H)\Psi_\mathrm{sc}(R,r) = V_\mathrm{int}(R,r)\Psi^0_{v_\mathrm{i}}(R,r)\,, \tag{1.30}$$

and the boundary conditions for which are

$$\Psi_\mathrm{sc}(R,r) \underset{r\to\infty}{\longrightarrow} \sum_{v_\mathrm{f}} f^\mathrm{VE}_{v_\mathrm{i}\to v_\mathrm{f}}\chi_{v_\mathrm{f}}(R)\sqrt{\frac{2k_\mathrm{f}}{\pi}}\,r h^{(1)}_l(k_\mathrm{f}r)\,, \tag{1.31}$$

$$\Psi_\mathrm{sc}(R,r) \underset{R\to\infty}{\longrightarrow} f^\mathrm{DA}_{v_\mathrm{i}}\phi_\mathrm{b}(r)\sqrt{\frac{2\mu}{\pi K_\mathrm{DA}}}\,R h^{(1)}_0(K_\mathrm{DA}R) \tag{1.32}$$

where $h^{(1)}_l$ is the spherical Hankel function (see Abramowitz and Stegun [1972]). Note that we do not consider the situation where both $R\to\infty$ and $r\to\infty$.

The scattering amplitude for vibrational excitation, $f^\mathrm{VE}_{v_\mathrm{i}\to v_\mathrm{f}}$, and for dissociative attachment, $f^\mathrm{DA}_{v_\mathrm{i}}$, are related to the T matrices for these processes which we will define below.

The sum in Eq. (1.31) runs over all open vibrational excitation channels, for which $\chi_{v_\mathrm{f}}(R)$ is the final vibrational state of the molecule with energy E_{v_f} and k_f denotes the final momentum of the electron. Eq. (1.32) is the asymptotic condition for the dissociative attachment channel (if it is open). We suppose here that the model potential in Eq. (1.12) supports only one bound state, $\phi_\mathrm{b}(r)$, of the electron as $R\to\infty$,

$$\left(-\frac{1}{2}\frac{\partial^2}{\partial r^2} + \frac{l(l+1)}{2r^2} + V_\mathrm{b}(r)\right)\phi_\mathrm{b}(r) = E_\mathrm{b}\phi_\mathrm{b}(r)\,, \tag{1.33}$$

which is appropriate for all models of electron-molecule collisions we will treat here. The binding energy, E_b, is related to the electron affinity, E_a, of the atom B by $E_a = -E_\mathrm{b}$. The relative momentum, K_DA, of A and B^- in the dissociative attachment channel is given by

$$E = \frac{K^2_\mathrm{DA}}{2\mu} + E_\mathrm{b}\,. \tag{1.34}$$

Finally, we give the expressions for the cross sections in terms of the T matrices defined for the vibrational excitation and dissociative attachment channels in terms of the matrix elements of the channel interaction potentials,

$$\begin{aligned} T^\mathrm{VE}_{v_\mathrm{i}\to v_\mathrm{f}}(E) &= \frac{f^\mathrm{VE}_{v_\mathrm{i}\to v_\mathrm{f}}(E)}{2k_\mathrm{ef}} = \langle\Psi^0_{v_\mathrm{f}}|V_\mathrm{VE}|\Psi^+_E\rangle \\ &= \int_0^\infty dR\int_0^\infty dr\,\Psi^0_{v_\mathrm{f}}(R,r)V_\mathrm{VE}(R,r)\Psi^+_E(R,r)\,, \end{aligned} \tag{1.35}$$

$$T^{\mathrm{DA}}_{v_\mathrm{i}}(E) = \frac{f^{\mathrm{DA}}_{v_\mathrm{i}}(E)}{2\mu k_{\mathrm{DA}}} = \langle \Psi^0_{\mathrm{DA}} | V_{\mathrm{DA}} | \Psi^+_E \rangle$$
$$= \int_0^\infty dR \int_0^\infty dr\, \Psi^0_{\mathrm{DA}}(R,r) V_{\mathrm{DA}}(R,r) \Psi^+_E(R,r)\,. \tag{1.36}$$

The unperturbed final states in the vibrational excitation channels $\Psi^0_{v_\mathrm{f}}(R,r)$ are given by (1.26), the final state in the dissociative attachment channel $\Psi^0_{\mathrm{DA}}(R,r)$ is given by (1.27), the interaction potential in the vibrational excitation channel is the interaction between the electron and molecule, given in Eq. (1.14),

$$V_{\mathrm{VE}}(R,r) = V_{\mathrm{int}}(R,r) \tag{1.37}$$

and in the dissociative attachment channel we define

$$V_{\mathrm{DA}}(R,r) = V_0(R) + V_{\mathrm{int}}(R,r) - \lim_{R\to\infty} V_{\mathrm{int}}(R,r)\,. \tag{1.38}$$

The resulting formulae for the cross sections can then be written as

$$\sigma^{\mathrm{VE}}_{v_\mathrm{i}\to v_\mathrm{f}}(E) = \frac{4\pi^3}{k_\mathrm{i}^2} \left| T^{\mathrm{VE}}_{v_\mathrm{i}\to v_\mathrm{f}}(E) \right|^2 , \tag{1.39}$$

$$\sigma^{\mathrm{DA}}_{v_\mathrm{i}}(E) = \frac{4\pi^3}{k_\mathrm{i}^2} \left| T^{\mathrm{DA}}_{v_\mathrm{i}}(E) \right|^2 . \tag{1.40}$$

1.4 Time-dependent solution

The time-dependent approach may be roughly summarized as computing the elements of the scattering matrix from the evolution of a physical state incoming from a specified channel and outgoing to all possible final channels.

As an initial state of the time evolution we take the molecule in a certain initial vibrational state $\chi_{v_i}(R)$ and the incoming electron described by a Gaussian wave packet of the width σ placed at r_0 in the asymptotic region, i.e.

$$\Psi^{\mathrm{in}}_{v_i}(R,r) = \frac{1}{(\pi\sigma^2)^{\frac{1}{4}}} \chi_{v_i}(R) e^{-\frac{(r-r_0)^2}{2\sigma^2} - ip_0 r}, \tag{1.41}$$

where p_0 denotes the mean momentum of the incoming electron. The elements of the S matrix are defined in terms of the asymptotic eigenstates (1.24), (1.26) and (1.27) of the channel Hamiltonians (1.19) and (1.20). For a given channel the eigenstates form a complete basis. In the initial vibrational excitation channel we can thus expand the wave function into the basis (1.24) as

$$\Psi^{\mathrm{in}}_{v_i}(R,r) = \int_0^\infty \eta^{\mathrm{in}}_{v_i}(\varepsilon) \chi_{v_i}(R) \mathcal{J}^l_k(r) d\varepsilon, \tag{1.42}$$

where k denotes the electron momentum given by $k = \sqrt{2\varepsilon} = \sqrt{2(E - E_{v_i})}$ with E_{v_i} being the energy of the initial vibrational state and the coefficients $\eta^{\mathrm{in}}_{v_i}(E)$ are

$$\eta^{\mathrm{in}}_{v_i}(E) = \int_0^\infty \int_0^\infty \varphi^{\mathrm{in}}_{v_i}(E,R,r)^* \Psi^{\mathrm{in}}_{v_i}(R,r) dr dR. \tag{1.43}$$

The propagation of the wave function is given by application of the unitary evolution operator

$$\psi(t+t_0) = U(t)\psi(t_0) = e^{-iHt}\psi(t_0). \tag{1.44}$$

The evolved wave function will be outgoing into all accessible channels and we need to calculate the S matrix from these outgoing waves. For this purpose we have tested three methods for the evaluation of the S-matrix elements.

1.4.1 Correlation function

The first is the correlation function approach described by Tannor and Weeks [1993]. Here we give only a brief overview and necessary formulas. The complete derivation using the spectral method or from the relations of completeness may be found in Tannor and Weeks [1993]. The method is based on the integration over time of the overlap of the evolved wave function with a test function placed in a channel of interest. In the vibrational excitation channels we assume the test functions to be a product of the final vibrational state $\chi_{v_f}(R)$ and an outgoing Gaussian wave packet in the electronic degree of freedom

$$\Phi^{\text{out}}_{v_f}(R,r) = \frac{1}{(\pi\sigma^2)^{\frac{1}{4}}}\chi_{v_f}(R)e^{-\frac{(r-r_0)^2}{2\sigma^2}+iq_0r}. \tag{1.45}$$

In the dissociative attachment channel we assume the test function to be a product of the attached electron bound state $\phi_{\text{b}}(r)$ and an outgoing Gaussian wave packet

$$\Phi^{\text{out}}_{\text{DA}}(R,r) = \frac{1}{(\pi\sigma^2)^{\frac{1}{4}}}\phi_{\text{b}}(r)e^{-\frac{(R-R_0)^2}{2\sigma^2}+iQ_0R}. \tag{1.46}$$

As mentioned above, the elements of the S matrix are defined in terms of the asymptotic eigenstates (1.26) and (1.27), thus decompositions of the test functions similar to (1.43) can be utilized. If we introduce the correlation function as an overlap of the evolved wave function with the test function in one of the possible channels

$$C_\beta(t) = \int_0^\infty\int_0^\infty (\Phi^{\text{out}}_\beta(R,r))^*\psi(R,r,t)\ dr\ dR, \tag{1.47}$$

where β stands for v_f or DA, then the S-matrix elements for both processes can be obtained from

$$S^{\text{T\&W}}_{v_i\to\beta}(E) = \frac{(2\pi)^{-1}}{\left(\eta^{\text{out}}_\beta(E)\right)^*\eta^{\text{in}}_{v_i}(E)}\int_{-\infty}^{\infty} C_\beta(t)e^{iEt}dt. \tag{1.48}$$

where E is the same for all channels and it is the total energy of the system

$$E = \frac{k_i^2}{2} + E_{v_i} = \frac{k_f^2}{2} + E_{v_f} = \frac{K^2}{2\mu} + E_{\text{b}}. \tag{1.49}$$

Although the above relations provide a proper mean to calculate the S-matrix elements, in practice one can encounter some numerical difficulties if the test functions are narrow and placed improperly. Since the test functions may in general

contain contributions of incoming as well as outgoing waves and the eigenstates (1.26, 1.27) do not distinguish the orientation of impulse, one should place the test functions closer to the interaction region than the incident wave packet (at least in the initial channel). In the following we choose a different approach considering only the outgoing part of the test functions, however we must now place the test functions further from the interaction region than the incident wave packet to guarantee there is no overlap with the incoming waves. The coefficients $\eta_{v_f}^{\mathrm{out}}(E)$ and $\eta_{\mathrm{DA}}^{\mathrm{out}}(E)$ can then be calculated as

$$\eta_{v_f}^{\mathrm{out}}(E) = \int_0^\infty \int_0^\infty \widetilde{\varphi}_{v_f}^{\mathrm{out}}(E,R,r)^* \Phi_{v_f}^{\mathrm{out}}(R,r)\, dr dR\,, \tag{1.50}$$

and

$$\eta_{\mathrm{DA}}^{\mathrm{out}}(E) = \int_0^\infty \int_0^\infty \widetilde{\varphi}_{\mathrm{DA}}^{\mathrm{out}}(E,R,r)^* \Phi_{\mathrm{DA}}^{\mathrm{out}}(R,r)\, dr dR. \tag{1.51}$$

where $\widetilde{\varphi}_{v_f}^{\mathrm{out}}(E,R,r)$ and $\widetilde{\varphi}_{\mathrm{DA}}^{\mathrm{out}}(E,R,r)$ denotes only the outgoing part of the functions (1.26, 1.27), i.e.

$$\widetilde{\varphi}_{v_f}^{\mathrm{out}}(E,R,r) = \chi_{v_f}(R)\sqrt{\frac{k_f}{2\pi}} r h_l^+(k_f r), \tag{1.52}$$

$$\widetilde{\varphi}_{\mathrm{DA}}^{\mathrm{out}}(E,R,r) = \sqrt{\frac{\mu}{2\pi K}} e^{iKR}\phi_{\mathrm{b}}(r), \tag{1.53}$$

where $h_l^+(k_f r)$ denotes the outgoing spherical Hankel function.

1.4.2 Modified correlation function

The second method for computation of the S-matrix elements is based on the previous one and can be derived simply by using the δ-function at some distance r_0 or R_0 instead of the Gaussian wave packet in the test functions (1.45, 1.46). As in the previous case we consider only the outgoing part of the δ-function decomposition and the corresponding coefficients then read

$$\eta_{v_f}'^{\mathrm{out}}(E) = \sqrt{\frac{k_f}{2\pi}} r_0 h_l^+(k_f r_0)^*\,, \tag{1.54}$$

$$\eta_{\mathrm{DA}}'^{\mathrm{out}}(E) = \sqrt{\frac{\mu}{2\pi K}} e^{-iKR_0}\,. \tag{1.55}$$

The elements of the S matrix for the vibrational excitation channels are then given by

$$S_{v_i\to v_f}^{\delta}(E) = \frac{(2\pi)^{-1}}{\left(\eta_{v_f}'^{\mathrm{out}}(E)\right)^* \eta_{v_i}^{\mathrm{in}}(E)} \int_{-\infty}^\infty \int_0^\infty dt dR\, e^{iEt} \chi_{v_f}(R)^* \psi(R,r_0,t)\,, \tag{1.56}$$

and for the dissociative attachment channel by

$$S_{v_i\to \mathrm{DA}}^{\delta}(E) = \frac{(2\pi)^{-1}}{\left(\eta_{\mathrm{DA}}'^{\mathrm{out}}(E)\right)^* \eta_{v_i}^{\mathrm{in}}(E)} \int_{-\infty}^\infty \int_0^\infty dt dr\, e^{iEt} \phi_{\mathrm{b}}(r)^* \psi(R_0,r,t)\,. \tag{1.57}$$

Note that the spatial integration is reduced to the channel internal degree of freedom thanks to the δ-function. This is the main advantage of this approach, since it is computationally much simpler. Also note that using the original approach with full decompositions into (1.26) and (1.27) would lead to zero values of $\eta_\beta^{\rm out}(E)$ at some energies, thus resulting in numerical instabilities.

1.4.3 Probability flux function

The third method of the evaluation of the S matrix may be derived from the time-independent formulation via projection of the flux on the given final state. Again we choose the outgoing waves approach and put $\widetilde{\varphi}_{v_f}^{\rm out}(R,r)$ given by (1.52) as the final state in the VE channels and $\widetilde{\varphi}_{\rm DA}^{\rm out}(R,r)$ given by (1.53) in the DA channel. The S-matrix elements can be calculated from the flux at the distance r_0, or R_0, far enough from the interaction zone. In the VE channels we obtain

$$\begin{aligned} S^{\rm F}_{v_i\to v_f}(E) &= \frac{1}{2\eta^{\rm in}_{v_i}(E)}\frac{1}{2i}\int_{-\infty}^{\infty}\int_{0}^{\infty} dt dR\, e^{iEt} \\ &\quad\times\left[(\widetilde{\varphi}^{\rm out}_{v_f})^*\left(\frac{\partial\psi(t)}{\partial r}\right)-\psi(t)\left(\frac{\partial(\widetilde{\varphi}^{\rm out}_{v_f})^*}{\partial r}\right)\right]_{r=r_0}, \end{aligned} \tag{1.58}$$

where we have omitted the spatial arguments (R,r) of the functions in the integrand for brevity. The S-matrix element for the DA channel is given by

$$\begin{aligned} S^{\rm F}_{v_i\to {\rm DA}}(E) &= \frac{1}{2\eta^{\rm in}_{v_i}(E)}\frac{1}{2i\mu}\int_{-\infty}^{\infty}\int_{0}^{\infty} dt dr\, e^{iEt} \\ &\quad\times\left[(\widetilde{\varphi}^{\rm out}_{\rm DA})^*\left(\frac{\partial\psi(t)}{\partial R}\right)-\psi(t)\left(\frac{\partial(\widetilde{\varphi}^{\rm out}_{\rm DA})^*}{\partial R}\right)\right]_{R=R_0}. \end{aligned} \tag{1.59}$$

1.4.4 The T-matrix elements and cross sections

Formulas for the cross sections depend on the wave function normalization (see Taylor [1991]). Here we used the same normalization as in the paper Houfek et al. [2008a], thus we have

$$\sigma_{v_i\to\beta}(E)=\frac{4\pi^3}{k_i^2}|T_{v_i\to\beta}(E)|^2, \tag{1.60}$$

where β stands again for v_f or DA and the T-matrix element is related to the S-matrix element by

$$T_{v_i\to\beta}(E)=\frac{S_{v_i\to\beta}(E)-\delta_{v_i,\beta}}{2\pi i}. \tag{1.61}$$

1.5 Local complex potential approximation

As in Váňa and Houfek [2017] we compare the results from the 2D model of the electron molecule collisions to a simple method called the local complex potential (LCP) approximation (Domcke [1991]). Here we summarize the time-dependent formulation of the approximation. The time-independent formulation may be

found in Houfek et al. [2006]. The LCP approximation solves the nuclear dynamics in the complex molecular anion potential $V_{\rm res}(R)$, defined as poles of the fixed-nuclei scattering matrix shifted by the neutral potential $V_0(R)$. The poles may be obtained as resonance or bound energies of the electronic Hamiltonian

$$H_{\rm el}(r;R) = -\frac{1}{2}\frac{\partial^2}{\partial r^2} + V(R,r), \tag{1.62}$$

which is parametrically dependent on the internuclear distance R. The complex potential $V_{\rm res}(R)$ can be written in the form

$$V_{\rm res}(R) = E_{\rm res}(R) - \frac{i}{2}\Gamma(R), \tag{1.63}$$

where the imaginary part is expressed using the resonance width $\Gamma(R)$. The imaginary part is nonzero only in the region where $V_0(R) < E_{\rm res}(R)$.

We assume that the molecule is in an initial vibrational state $\chi_{v_i}(R)$ and as an initial wave packet within the LCP approximation we can take the initial vibrational state modified by a square root of the resonance width (see e.g. Domcke [1991] for details)

$$\Psi_{\rm LCP}(R, t=0) = \sqrt{\frac{\Gamma(R)}{2\pi}}\chi_{v_i}(R). \tag{1.64}$$

The motion of the wave packet is given by the evolution operator (1.44) but now with the Hamiltonian given by

$$H_{\rm LCP}(R) = -\frac{1}{2\mu}\frac{\partial^2}{\partial R^2} + E_{\rm res}(R) - \frac{i}{2}\Gamma(R). \tag{1.65}$$

The elements of the T-matrix for the VE and DA processes may be expressed as (see Domcke [1991])

$$T^{\rm LCP}_{v_i\to v_f}(E) = \frac{1}{i}\int_0^\infty dt \int_0^\infty dR\; e^{iEt}\,\chi^*_{v_f}(R)\sqrt{\frac{\Gamma(R)}{2\pi}}\Psi_{\rm LCP}(R,t), \tag{1.66}$$

$$T^{\rm LCP}_{v_i\to {\rm DA}}(E) = \sqrt{\frac{K}{2\pi\mu}}\lim_{R\to\infty} e^{-iKR}\int_0^\infty dt\; e^{iEt}\Psi_{\rm LCP}(R,t). \tag{1.67}$$

and the cross sections then read

$$\sigma^{\rm LCP}_{v_i\to\beta}(E) = \frac{4\pi^3}{k_i^2}|T^{\rm LCP}_{v_i\to\beta}(E)|^2, \tag{1.68}$$

where β stands for any of $v_f = v_0, v_1, ...$ or DA, k_i denotes the momentum of the incoming electron, and E is the total energy of the system given by the equation (1.49).

1.6 Projection on a diabatic state

One of the goals of this thesis is comparison of the nuclear dynamics of the full two-dimensional model with the LCP approximation. In order to be able to

compare not only the resulting cross sections but also the evolution of the wave packets we use a projection of the 2D wave packet on a certain electronic state to obtain a function dependent only on the internuclear distance.

The LCP approximation can be derived from the more general nonlocal theory of the nuclear dynamics of the resonant electron-molecule collisions Domcke [1991] that is based on a choice of the so-called discrete electronic state and thus on separation of the electronic Hilbert space into a resonant and background part. If the projection on this discrete state is made one gets the nuclear wave function corresponding to the resonant nuclear motion. Several possibilities how to choose the discrete state were discussed in the paper Houfek et al. [2008a]. We decided to project the 2D wave packet onto the *physical choice* of the discrete state $\phi_d(R, r)$ described in Houfek et al. [2008a], the energy of which is very close to the real part of the local complex potential. The detailed discussion of the nonlocal theory is out of the scope of this thesis and for details we refer to the papers cited above.

The *physical choice* of the discrete state is obtained as eigenstates of the fixed-nuclei electronic Hamiltonian corresponding to the bound state for larger internuclear distances and the resonance for smaller internuclear distances. Since the discrete state must be from the $L^2(\mathbb{R})$ Hilbert space for each R the resonance eigenstates have to be smoothly suppressed for larger electronic distances. As the suppressing function we have used

$$f(r) = 1 - \frac{1}{1 - e^{-(r-r_d)}}, \tag{1.69}$$

where r_d is the middle point of the region where the functions are suppressed. For further use we define a projection onto the discrete state as the integration of the overlap of the two-dimensional wave function with the discrete state over the electronic coordinate, i.e.

$$\Psi_d(R, t) = \int_0^\infty dr\ \Psi(R, r, t)\phi_d^*(R, r). \tag{1.70}$$

The discrete state is parametrically dependent on R due to dependence of the electronic Hamiltonian (1.62) on the internuclear distance.

1.7 Model of dissociative recombination

As a straightforward extension of the model of electron-molecule collisions introduced in Sec. 1.2 we introduce the model of electron collision with the simplest diatomic cation H_2^+ with the potential proposed by Hamilton [2003]. We will use this model to investigate the process of dissociative recombination (3). The original two-dimensional model has to be modified, apart from changing the interaction potential, by adding the Coulomb interaction potential for the incoming electron.

The full Hamiltonian of the model can be divided in three parts

$$H(R, r) = H_0^{\text{ion}}(R) + H_0^{\text{el}}(r) + V_{\text{int}}(R, r). \tag{1.71}$$

Table 1.2: Parameters of the model for the $e^- + H_2^+$ system given in atomic units, so that the resulting potential energy is in hartrees.

Parameter	Value/a.u.
μ	918.076
l	1 (p-wave)
a_0	0.1027
α	0.69
R_0	2.0
a_1	1.6435
a_2	6.2
a_3	0.0125
a_4	1.15

The first term is the Hamiltonian of the vibrational motion of the molecular cation

$$H^{\text{ion}}(R) = -\frac{1}{2\mu}\frac{\partial^2}{\partial R^2} + V_0(R), \tag{1.72}$$

where μ is the reduced mass of the cation and the potential energy in our model is again taken simply as the Morse potential (1.15) with parameters adjusted to approximate closely the lowest electronic state of the molecular cation. For the ${}^1\Sigma_g^+$ state of H_2^+ the parameters are given in Tab. 1.2.

The second term in the full Hamiltonian (1.71) reads

$$H_0^{\text{el}}(r) = -\frac{1}{2}\frac{\partial^2}{\partial r^2} + \frac{l(l+1)}{2r^2} - \frac{1}{r} \tag{1.73}$$

and describes an incoming electron with angular momentum l attracted by the Coulomb field of the molecular ion. The last term in (1.71) is the interaction potential which provides the coupling between the nuclear and electronic degrees of freedom. For the $e^- + H_2^+$ system it is taken from Hamilton [2003] and reads

$$V_{\text{int}}(R,r) = -a_1\left(1 - \tanh\frac{a_2 - R - a_3R^4}{7}\right)\left(\tanh\frac{R}{a_4}\right)^4 \frac{e^{-\frac{r^2}{3}}}{r}, \tag{1.74}$$

with parameters given in Tab. 1.2. For large electron distances the interaction potential vanishes, but for large internuclear distances it is convenient to define the limit of the interaction potential as

$$V_{\text{int}}^{\infty}(r) = \lim_{R\to\infty} V_{\text{int}}(R,r) = -2a_1\frac{e^{-\frac{r^2}{3}}}{r}. \tag{1.75}$$

1.7.1 The channel Hamiltonians and eigenstates

As in the electron-molecule case it is convenient to write down channel Hamiltonians. For vibrational excitations the channel Hamiltonian consist of the first two terms from equation (1.71), i.e.

$$H_0^{\text{VE}} = H_0^{\text{ion}}(R) + H_0^{\text{el}}(r) \tag{1.76}$$

and describes the vibrational motion of the nuclei and the electron motion in the ion Coulomb field.

The dissociative recombination channel Hamiltonian

$$H_0^{\mathrm{DR}}(R,r) = -\frac{1}{2\mu}\frac{\partial^2}{\partial R^2} + H_0^{\mathrm{el}}(r) + V_{\mathrm{int}}^{\infty}(r), \tag{1.77}$$

describes the motion of free nuclei and the electron trapped in the Coulomb potential corrected by remaining part of the interaction potential. Note that for consistency reasons the spectrum of last two terms of the equation (1.77) should be close to the electronic spectrum of the hydrogen atom. As it was pointed out by Hamilton [2003] the spectrum is well approximated with exception of the lowest DR state which is unphysical. However, this does not harm the results as we will discuss later.

Before presenting the channel continuum states, we define the solution to the Coulomb problem. Provided the coefficient $\eta = -Z/k$, where Z stands for charge and variable $\rho = kr$ the Coulomb problem is given by the equation

$$\left(\frac{\partial^2}{\partial\rho^2} + 1 - \frac{2\eta}{\rho} - \frac{l(l+1)}{\rho^2}\right)\omega_l(\rho) = 0, \tag{1.78}$$

with regular solution $F_l(\eta,\rho)$ and irregular solution $G_l(\eta,\rho)$. The normalization is fixed by conditions for behavior in the asymptotic region

$$F_l(\eta,\rho) \xrightarrow{\rho\to\infty} \sin\left[\rho - \eta\log(2\rho) - \frac{l\pi}{2} + \arg\Gamma(l+1+i\eta)\right] + O(\rho^{-1}), \tag{1.79}$$

$$G_l(\eta,\rho) \xrightarrow{\rho\to\infty} \cos\left[\rho - \eta\log(2\rho) - \frac{l\pi}{2} + \arg\Gamma(l+1+i\eta)\right] + O(\rho^{-1}). \tag{1.80}$$

Now we can define the energy-normalized electron continuum states with angular momentum l as the regular spherical Coulomb function for the charge $Z = 1$

$$\mathcal{F}_k^l(r) = \sqrt{\frac{2}{k\pi}} r F_l(\frac{-1}{k}, kr), \tag{1.81}$$

thus the energy-normalized incident eigenstate of Hamiltonian from the Eq. (1.76) with the total energy $E = E_{v_i} + k_i^2/2$ is given by

$$\varphi_{v_i}^{\mathrm{in}}(E,R,r) = \chi_{v_i}(R)\mathcal{F}_{k_i}^l(r), \tag{1.82}$$

where $\chi_{v_i}(R)$ is again the vibrational eigenstate, the solution of Eq. (1.25).

Contrary to the dissociative attachment case, where only one channel was assumed, the dissociative recombination permits infinity of outgoing states, since there is an infinity of bound states of the hydrogen atom. In the dissociative recombination channels we assume the continuum eigenstate to be described by the same state as for dissociative attachment, i.e. $\mathcal{E}_K(R)$ given by eq. (1.23). The energy-normalized eigenstates of dissociative recombination channel Hamiltonian H_0^{DR} then reads

$$\varphi_{\mathrm{DR}_n}^{\mathrm{out}}(E,R,r) = \mathcal{E}_{K_{\mathrm{DR}_n}}(R)\xi_n(r)\,, \tag{1.83}$$

where $\xi_n(r)$ is the n-th bound state of

$$\left(-\frac{1}{2}\frac{\partial^2}{\partial r^2} + \frac{l(l+1)}{2r^2} - \frac{1}{r} + V_{\mathrm{int}}^{\infty}(r)\right)\xi_n(r) = \epsilon_n\xi_n(r)\,, \tag{1.84}$$

As it was mentioned above, in the physical reality the states $\xi_{\rm n}$ should coincide with the Rydberg states of the hydrogen atom, as well as the energies ϵ_n should coincide with the Rydberg energy levels.

1.7.2 Time-independent solution

Solving the model in the time-independent approach is very similar to the previous electron-molecule case with only slight modifications. We start with the Schrödinger equation (1.28) with the Hamiltonian (1.71). As the initial state Ψ^0_E we take the incident eigenstate (1.82) and we compute the scattered part $\Psi_{\rm sc}$ of the physical wave function Ψ^+_E given from Eq. (1.30). The first difference appears in the required boundary conditions for the scattered wave function, i.e.

$$\Psi_{\rm sc}(R,r) \underset{r\to\infty}{\longrightarrow} \sum_{v_{\rm f}} f^{\rm VE}_{v_{\rm i}\to v_{\rm f}}\chi_{v_{\rm f}}(R)\sqrt{\frac{2}{k_{\rm f}\pi}}\, r H^+_l(\frac{-1}{k_{\rm f}}k_{\rm f}r)\,, \tag{1.85}$$

$$\Psi_{\rm sc}(R,r) \underset{R\to\infty}{\longrightarrow} \sum_{\rm DR_n} f^{\rm DR_n}_{v_{\rm i}}\xi_{\rm n}(r)\sqrt{\frac{2\mu}{\pi K_{\rm DR_n}}}\, R h^{(1)}_0(K_{\rm DR_n}R), \tag{1.86}$$

where the functions $H^+_l(\frac{-1}{k_{\rm f}}, k_{\rm f}r)$ are derived from the spherical Coulomb functions in the similar way as the spherical Hankel functions from the spherical Bessel and Neumann functions (Abramowitz and Stegun [1972])

$$H^\pm_l(\eta,\rho) = G_l(\eta,\rho) \pm iF_l(\eta,\rho). \tag{1.87}$$

The elements of the T matrix in dissociative recombination channels are then given by a similar equation as (1.36),

$$\begin{aligned} T^{\rm DR_n}_{v_{\rm i}}(E) &= \frac{f^{\rm DR_n}_{v_{\rm i}}(E)}{2\mu K_{\rm DR_n}} = \langle \Psi^0_{\rm DR_n}|V_{\rm DR}|\Psi^+_E\rangle \\ &= \int_0^\infty dR \int_0^\infty dr\, \Psi^0_{\rm DR_n}(R,r)V_{\rm DR}(R,r)\Psi^+_E(R,r)\,. \end{aligned} \tag{1.88}$$

provided the channel state $\Psi^0_{\rm DR_n} = \varphi^{\rm out}_{\rm DR_n}(E,R,r)$ and the interaction potential in the dissociative recombination channel is

$$V_{\rm DR}(R,r) = V_0(R) + V_{\rm int}(R,r) - V^\infty_{\rm int}(r)\,. \tag{1.89}$$

Using the above defined energy normalization, the cross sections are then given by the same relation as in the eq. (1.40),

$$\sigma^{\rm DR_n}_{v_{\rm i}}(E) = \frac{4\pi^3\mu}{k^2_{\rm i}}\left|T^{\rm DR_n}_{v_{\rm i}}(E)\right|^2\,. \tag{1.90}$$

1.7.3 Time-dependent solution

As for the time-independent approach the time-dependent method is also very similar to the previous model of electron-molecule collisions. We choose the initial state of the system to be exactly the same, i.e. given by the eq. (1.41). We compute the coefficients of the expansion to energy-normalized channel eigenstates

as in the eq. (1.43), only as the basis we take the initial states (1.82). The only investigated method for the dissociative recombination was the correlation function approach. The test functions are defined in a similar way as in the eq. (1.46), i.e.

$$\Phi^{\mathrm{out}}_{\mathrm{DR_n}}(R,r) = \frac{1}{(\pi\sigma^2)^{\frac{1}{4}}}\xi_{\mathrm{n}}(r)e^{-\frac{(R-R_0)^2}{2\sigma^2}+iQ_0R}. \tag{1.91}$$

The decomposition coefficients then read

$$\eta^{\mathrm{out}}_{\mathrm{DR_n}}(E) = \int_0^\infty\int_0^\infty \widetilde{\varphi}^{\mathrm{out}}_{\mathrm{DR_n}}(E,R,r)^*\Phi^{\mathrm{out}}_{\mathrm{DR_n}}(R,r)\,drdR \tag{1.92}$$

provided the basis functions $\widetilde{\varphi}^{\mathrm{out}}_{\mathrm{DR_n}}$ are given as

$$\widetilde{\varphi}^{\mathrm{out}}_{\mathrm{DR_n}}(E,R,r) = \sqrt{\frac{\mu}{2\pi K_{\mathrm{DR_n}}}}e^{iK_{\mathrm{DR_n}}R}\xi_{\mathrm{n}}(r). \tag{1.93}$$

We use the correlation functions in the same form as in the eq. (1.47). Substituting the decomposition coefficients we can use the S-matrix definition (1.48). The definition of T-matrix elements (1.61) is also the same and the cross sections are defined in the same way as for the time-independent solution, see the eq. (1.90).

2. Numerical solution

To obtain the numerical solution of the dynamics of either electron-molecule collision models or dissociative recombination model in both the time-independent and time-dependent approach we have to choose a suitable discretization and assure the proper boundary conditions.

It is quite obvious that all of the studied models have to be confined to some finite region of both the electronic and the nuclear coordinate. To assure the proper boundary conditions and to avoid the reflections of the outgoing wave functions from the finite boundaries we employ the exterior complex scaling method (ECS) described by McCurdy and Stroud [1991] for both coordinates.

As the discretization method we have chosen the finite elements method combined with discrete variable representation (FEM-DVR) introduced by Rescigno and McCurdy [2000] (see also McCurdy et al. [2004] for further details).

To solve the evolution within the time-dependent formulation we use the generalized Crank-Nicolson method (van Dijk and Toyama [2007]). The following text should serve only as an overview of the method, details can be found in the cited papers.

2.1 Exterior complex scaling

In the previous chapter we have introduced the boundary conditions for the scattered wave function within the time-independent approach, i.e. for the electron-molecule collision models in (1.31) and (1.32) and for the model of dissociative recombination in (1.85) and (1.86). For the time-dependent approach to the model dynamics of the studied models the boundary conditions have to assure that no outgoing waves are reflected back from the finite boundary of the coordinates.

In both cases we use the same method based on bending the real electronic, r, and the nuclear, R, coordinate into the complex plane at some finite point r_0 and R_0, respectively, in the following manner,

$$r'(r) = \begin{cases} r, & r < r_0\,, \\ r_0 + (r - r_0)e^{i\theta_r}, & r \geq r_0\,, \end{cases} \tag{2.1}$$

$$R'(R) = \begin{cases} R, & R < R_0\,, \\ R_0 + (R - R_0)e^{i\theta_R}, & R \geq R_0\,. \end{cases} \tag{2.2}$$

As a result for $\theta \in (0, \frac{\pi}{2})$ the complex scaled region suppresses the amplitude of the outgoing waves as

$$e^{ikr'} \underset{r>r_0}{=} e^{ik(r_0+(r-r_0)e^{i\theta})} = e^{ik(r_0+(r-r_0)\cos\theta)}e^{-k(r-r_0)\sin\theta} \underset{r\to\infty}{\longrightarrow} 0. \tag{2.3}$$

Therefore we can use the Dirichlet boundary condition at some large enough distance $r_{\max}$ and $R_{\max}$, respectively. The main advantage of this method lies in the fact that on the real part of the coordinates the solution remains identical to the solution of the real problem as it was demonstrated in McCurdy and Stroud [1991]. However the proper choice of r_0 and R_0 depends on several aspects of the model which will be discussed later.

2.2 Finite elements method

The finite elements method is one of the most common methods used in computational physics. The theory behind this method is very elegant but also quite complex. Here we summarize only the absolute basics to provide consistent picture of the numerical solution. For details please see e.g. Johnson [1987].

We will demonstrate the principles of method on a one-dimensional example of the driven Schrödinger similar to (1.30). The extension to multiple dimensions or to other equations is straightforward and will be discussed in the following sections. We assume the equation

$$\left(E - V(x) + \frac{1}{2\mu}\frac{\partial^2}{\partial x^2}\right)\Psi_{\mathrm{sc}}(x) = V_{\mathrm{int}}(x)\Phi(x) \tag{2.4}$$

on a confined region Ω with the Dirichlet boundary conditions. We consider this equation in its *weak form* as

$$\begin{aligned}\int_\Omega \phi^*(x)(E - V(x))\Psi_{\mathrm{sc}}(x)\,dx \\ +\frac{1}{2\mu}\int_\Omega \frac{\partial\phi^*(x)}{\partial x}\frac{\partial\Psi_{\mathrm{sc}}(x)}{\partial x}\,dx &= \int_\Omega \phi^*(x)V_{\mathrm{int}}(x)\Phi(x)\,dx\end{aligned} \tag{2.5}$$

which must be satisfied for any testing function $\phi(x) \in \mathcal{H}_{\mathrm{D}}(\Omega)$, where $\mathcal{H}_{\mathrm{D}}(\Omega)$ consists of all continuous functions with at least piecewise continuous derivatives on Ω with the Dirichlet boundary conditions. By choosing a basis ϕ_j in $\mathcal{H}_{\mathrm{D}}(\Omega)$, we may decompose the solution $\Psi_{\mathrm{sc}}(x)$ into this basis

$$\Psi_{\mathrm{sc}}(x) = \sum_j c_j\phi_j(x). \tag{2.6}$$

By substituting the decomposition into (2.5) and by using the basis functions $\phi_i(x)$ as test functions we can get a matrix equation for the coefficients c_j

$$\sum_j (E - V_{ij} - T_{ij})c_j = b_i, \tag{2.7}$$

where

$$T_{ij} = -\frac{1}{2\mu}\int_\Omega \frac{\partial\phi_i^*(x)}{\partial x}\frac{\partial\phi_j(x)}{\partial x}\,dx, \tag{2.8}$$

$$V_{ij} = \int_\Omega \phi_i^*(x)V(x)\phi_j(x)\,dx, \tag{2.9}$$

and the right hand side is

$$b_i = \int_\Omega \phi_i^*(x)V_{\mathrm{int}}(x)\Phi(x)\,dx\,. \tag{2.10}$$

The finite elements method is based on the approximation of the infinite basis ϕ_j by a finite set of functions with a compact support, which provide computational efficiency since a lot of the matrix elements (2.8) and (2.9) may be equal to zero. To build the FEM representation we divide the coordinate to a finite set of M adjacent intervals $[x^m, x^{m+1}]$ which we refer to as *elements*. Elements may differ in their lengths which can be also used for computational efficiency.

2.3 Discrete variable representation

It is obvious that the matrix elements (2.8), (2.9) and the right-hand side (2.10) may become quite difficult to evaluate. An efficient way to simplify the evaluation of the potential matrix elements (2.9) is to use the *discrete variable representation*.

The method is based on use of a set of coordinate discretization points $x_j \in \Omega$ and a corresponding set of basis functions $\phi_j(x)$ for which the coordinate operator X is diagonal, i.e.

$$\int_\Omega x\phi_i^*(x)\phi_j(x)\,dx = \delta_{ij}x_j. \tag{2.11}$$

One way to build this representation is to diagonalize the X operator in any basis and construct a new basis from the computed eigenstates.

Another and probably more simple way is to choose the basis functions in such a way that the X operator is effectively diagonal with respect to some quadrature I_{N_q}. We use the Gauss-Lobatto quadrature of the order N_q on each element, i.e. on the m-th element $[x^m, x^{m+1}]$ we have

$$\int_{x^m}^{x^{m+1}} f(x)\,dx \simeq \sum_{n=1}^{N_\mathrm{q}} w_n^m f(x_n^m), \tag{2.12}$$

where x_n^m are the quadrature points and w_n^m are the quadrature weights. Apparently the quadrature points overlap for adjacent elements, i.e. $x_{N_\mathrm{q}}^m = x_1^{m+1}$. We define the set of coordinate discretization points x_j as the union of the quadrature points from all elements, where the overlapping points are identified and counted only once,

$$\begin{aligned} x_j &= x_n^m, & (2.13)\\ n &= \mathrm{mod}(j, N_\mathrm{q}-1)+1\,, & (2.14)\\ m &= \frac{j-n+1}{N_\mathrm{q}-1}+1\,, & (2.15) \end{aligned}$$

for $j = 1, \ldots, N_\mathrm{b}$ with $N_\mathrm{b} = M(N_\mathrm{q}-1)-1$ since we discard both first and last point of the discretization because of the Dirichlet boundary conditions.

To construct the basis functions we define the Lagrange interpolation polynomials through the quadrature points x_n^m,

$$\ell_n^m(x) = \prod_{\substack{k=1\\k\neq n}}^{N_\mathrm{q}} \frac{x-x_k^m}{x_n^m-x_k^m}, \tag{2.16}$$

for all $x \in [x^m, x^{m+1}]$ and identically zero otherwise. Important attribute of the functions $\ell_n^m(x)$ is the fact that only one of these functions on given element is nonzero in the corresponding quadrature point x_n^m. The corresponding basis functions are then constructed from $\ell_n^m(x)$ as

$$\phi_j(x) = \begin{cases} \frac{1}{\sqrt{w_{N_\mathrm{q}}^m + w_1^{m+1}}}\left(\ell_{N_\mathrm{q}}^m(x) + \ell_1^{m+1}(x)\right) & \text{for mod}\,(j, N_\mathrm{q}) = 0,\\ \frac{1}{\sqrt{w_n^m}}\ell_n^m(x) & \text{otherwise} \end{cases} \tag{2.17}$$

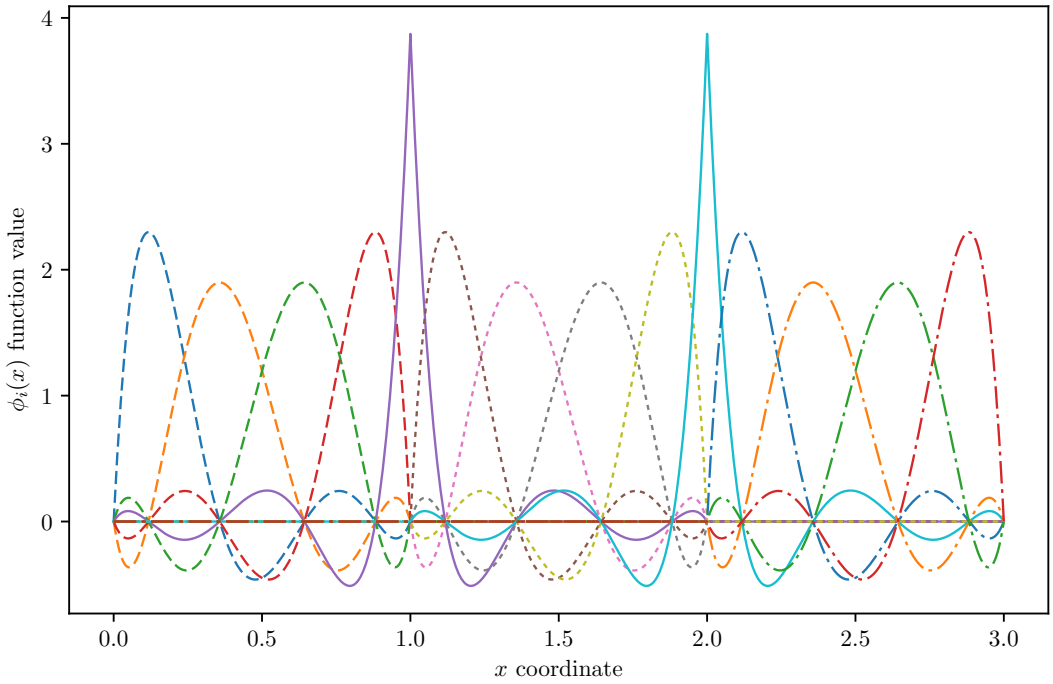

Figure 2.1: An example of the FEM-DVR basis on a sample interval $[0, 3]$ with three elements of unit size and the quadrature order $N_\mathrm{q} = 6$. The dashed, dotted and dash-dotted curves are basis functions on the first, second and third element, respectively. The solid line curves are the bridging basis functions.

where indices n, m are given by (2.14), (2.15) respectively and the normalization factors are in fact given by the quadrature weights. We show an example of the basis functions on sample discretization in Fig. 2.1. Arranging the weights to

$$w_j = \begin{cases} w^m_{N_\mathrm{q}} + w^{m+1}_1, & \text{for mod } (j, N_\mathrm{q} - 1) = 0, \\ w^m_n, & \text{otherwise,} \end{cases} \tag{2.18}$$

we may rewrite (2.11) as

$$\int_\Omega x\phi^*_i(x)\phi_j(x)dx \approxeq \sum_{k=1}^{N_b} w_k x_k \phi^*_i(x_k)\phi_j(x_k) = x_j\delta_{ij}. \tag{2.19}$$

Since the representation of X operator is diagonal, any function of x is diagonal as well and thus we may write the potential matrix elements (2.9) as

$$V_{ij} = V(x_i)\delta_{ij} \tag{2.20}$$

and similarly for the right hand side coefficients (2.10)

$$b_i = \sqrt{w_i}V_\mathrm{int}(x_i)\Phi(x_i). \tag{2.21}$$

Since the basis functions are defined as polynomials, the kinetic energy matrix (2.8) is also easy to evaluate and even though it is dense on each element, the resulting matrix is still very sparse.

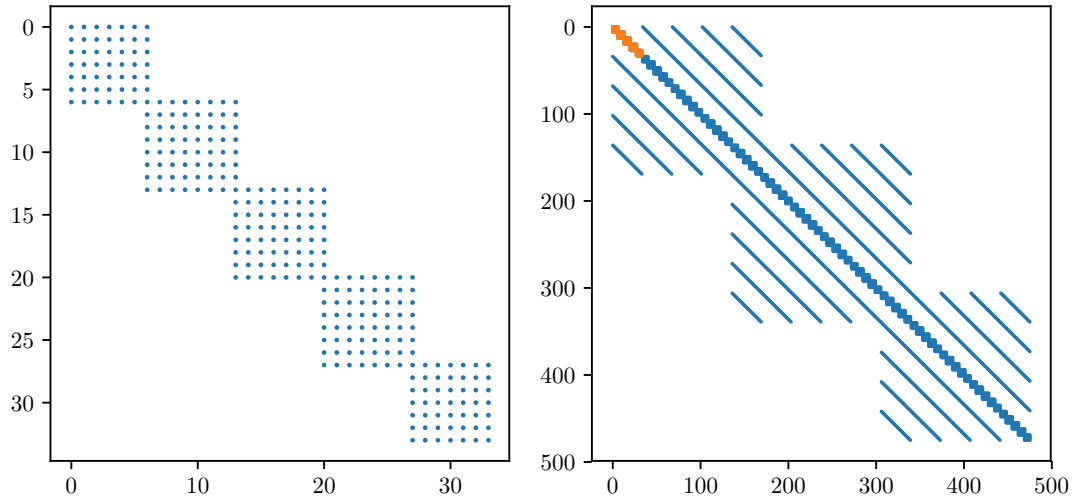

Figure 2.2: The examples of the kinetic energy matrix $\mathbf{T}$ structure in one and two dimensions. The left panel shows one-dimensional example $\mathbf{T}_x$ for x-coordinate discretization with five elements and the quadrature order $N_\mathrm{q} = 8$. The right panel shows a two-dimensional example $\mathbf{T}_\mathrm{2D}$ constructed by (2.23) with $\mathbf{T}_x$ from the previous example and $\mathbf{T}_y$ for y-coordinate discretization with three elements and the quadrature order $N_\mathrm{q} = 6$. The orange color marks the one-dimensional building block $\mathbf{T}_x$ for the first y-coordinate basis function.

Extending the FEM-DVR discretization into multiple dimensions consists of generating the multi-dimensional basis functions via outer product of the above defined one-dimensional bases, e.g. for two coordinates x, y

$$\phi_{ij}(x, y) = \phi_i(x)\phi_j(y), \tag{2.22}$$

for all $i = 1, \ldots, N_\mathrm{b}^x$ and $j = 1. \ldots, N_\mathrm{b}^y$. The matrix representation of the kinetic energy operator is then given by the sum of the tensor product of one-dimensional kinetic energy matrix representations with identity matrix in the other dimension, in our case

$$\mathbf{T}_\mathrm{2D} = \mathbf{T}_x \otimes \mathbf{1}_y + \mathbf{1}_x \otimes \mathbf{T}_y. \tag{2.23}$$

Examples of the one-dimensional kinetic energy matrix and its extension in two dimensions are shown in Fig. 2.2. Note that the actual structure of the two-dimensional matrix $\mathbf{T}_\mathrm{2D}$ depends on the ordering of the two-dimensional basis (2.22). We have chosen the natural ordering by repeating the x-coordinate basis for each y-coordinate basis function. The matrix representation of the potential terms is still diagonal in the multi-dimensional case.

2.4 Evolution operator approximation

Solving the time-dependent dynamics numerically also requires an accurate approximation of the evolution operator. For this purpose we use the generalized Crank-Nicolson method with the Padé approximant expressed as a product of

simple rational terms which are applied subsequently to the wave function,

$$\psi(t+\Delta t) = e^{-iH\Delta t}\psi(t) \approx \prod_{i=1}^{N} \frac{(1+c_j H\Delta t)}{(1-c_j^* H\Delta t)}\psi(t), \tag{2.24}$$

where c_j denotes the j-th root of the Padé approximant, N is the order of the approximation and Δt the evolution time step.

Since we use the FEM-DVR discretization, the matrices representing the Hamiltonian are very sparse, however the resulting Padé approximation does not have to keep the sparsity. For this reason it is convenient to keep the approximation in the product form (2.24) and apply the respective participants subsequently. Furthermore the application of the inversed terms $(1 - c_j^* H\Delta t)$ may be performed via specialized LU decomposition and back substitution for sparse matrices (Intel MKL, SuperLU).

Using a sufficiently small time step Δt and a sufficiently high order of the Padé approximation leads to accurate results of the evolution, see Formánek et al. [2010]. The integrations over time in (1.48), (1.56) and other equations were approximated by the Simpson rule. Since the infinite integrations over time are approximated by finite integrations we may expect inaccuracies for kinetic energies of the incoming electron very close to zero.

Note that since we use the exterior complex scaling, the matrix representing the Hamiltonian is no longer a hermitian and the evolution operator is no longer unitary for the wave function is suppressed beyond the complex scaling border.

2.5 Model parametrizations

Here we specify the parameters of the FEM-DVR-ECS discretization for all three studied models of electron-molecule collisions (N_2-like, NO-like and F_2-like) and for the dissociative recombination model of H_2^+. At the end of this section we also specify the parametrization of the time evolution. All quantities are given in atomic units.

Table 2.1: The parametrization of FEM-DVR-ECS grids for both nuclear and electronic coordinates for N_2-like and NO-like models.

N_2-like				NO-like			
electronic		nuclear		electronic		nuclear	
$n_q = 10$		$n_q = 12$		$n_q = 8$		$n_q = 14$	
r	n	R	n	r	n	R	n
5.0	5	1.0	1	1.0	1	1.0	1
7.0	1	1.5	1	3.0	1	1.6	1
10.0	1	3.0	10	6.0	1	9.0	37
90.0	20	4.0	2	10.0	1	-	-
-	-	5.0	1	90.0	1	-	-
$\theta = 35.0$		$\theta = 35.0$		$\theta = 35.0$		$\theta = 45.0$	
$n_c = 15$		$n_c = 10$		$n_c = 15$		$n_c = 10$	

For a simpler construction of the grids we have used the same quadrature order n_q on each FEM-DVR element of a given coordinate, but the order n_q

may differ for different coordinates and models. The individual lengths of the elements were chosen with respect to the shape of the potential energy surface $V(R, r)$, i.e. the density of the discretization is increased in the areas where the potential energy surface has deeper wells. The detailed images of the potential energy surfaces may be found in Chap. 3, for the N_2-like model in Fig. 3.1, the NO-like model in Fig. 3.8 and the F_2-like model in Fig. 3.15, and in Chap. 4 for the dissociative recombination H_2^+-like model in Fig. 4.1.

We have used the exterior complex scaling for both coordinates in all investigated models. The lengths of complex scaled elements were set with exponential increment, with exception of the first two elements. The positions of the element endpoints of the elements are given by increasing sequence of n_c values, given by

$$r'_m = \begin{cases} r_0 + mhe^{i\theta}, & \text{for } m = 1, 2\,, \\ r'_{m-1} + e^{\alpha(m-2)}he^{i\theta}, & \text{for } m = 3, \ldots, n_c\,, \end{cases} \tag{2.25}$$

where r_0 stands for the point of the coordinate bending into the complex plane, h is the scaled element length, α is the real exponential scaling argument, m is the element index counting from the point of bending into the complex plane, θ is the complex scaling angle and i is the imaginary unit. The real exponential scaling parameter is set uniformly for all investigated models to $\alpha = 0.2$, the scaled element length h is always the length of the last real element and r_0 is the last real element endpoint.

Table 2.2: The parametrization of the FEM-DVR-ECS grids for both nuclear and electronic coordinates for F_2-like and H_2^+-like models.

F_2-like				H_2^+-like			
electronic		nuclear		electronic		nuclear	
$n_q = 12$		$n_q = 20$		$n_q = 8$		$n_q = 8$	
r	n	R	n	r	n	R	n
1.5	6	1.8	9	1.1	10	1.0	5
2.0	1	2.0	1	4.1	10	14.05	90
4.0	1	2.5	5	20.1	16	14.5*	3
10.0	2	2.5969	4	100.1	20	-	-
90.0	20	2.7	4	1300.1	120	-	-
-	-	10.7	4	-	-	-	-
$\theta = 40.0$		$\theta = 35.0$		$\theta = 5.0$		$\theta = 22.0$	
$n_c = 15$		$n_c = 15$		$n_c = 25$		$n_c = 25$	

The parameters used in our calculations for all studied models are arranged in the Table 2.1 and Table 2.2. All grids started at the origin of the coordinates and the number of elements n next to a certain distance is the number of elements on the interval from the previous distance to the specified one. We should note that we had to increase the density of the discretization in the real region of the nuclear coordinate for the NO-like and F_2-like models to be sufficiently dense for placing the DA channel test function. The density was significantly reduced for the model of dissociative recombination of H_2^+ since we will confine ourselves on a smaller energy range, the model has significantly smaller reduced mass and its coordinate ranges are significantly larger.

For the time evolution operator we used the diagonal Padé approximation (2.24). For the electron-molecule collisions models we used the order of the Padé approximation $N = 3$ which is sufficiently accurate with the time step $\Delta t = 1.0$, which is about 0.024 fs. For the dissociative recombination model we have used a larger time step $\Delta t = 10.0$ but also a higher order of the Padé approximation $N = 5$.

2.6 Visualization of 2D complex wave function

Since the complex numbers have two components it is quite a challenge to display the whole two-dimensional wave function. The common procedure is to either split the real and the imaginary parts into separate figures or to display the probability density only, discarding the complex phase. Both possibilities are inconvenient in their own way. The result is either too complicated or the displayed information is not complete. This problem becomes even more aching within the time-dependent computations since time itself is another dimension to display. A convenient solution to the problem is to identify the complex numbers

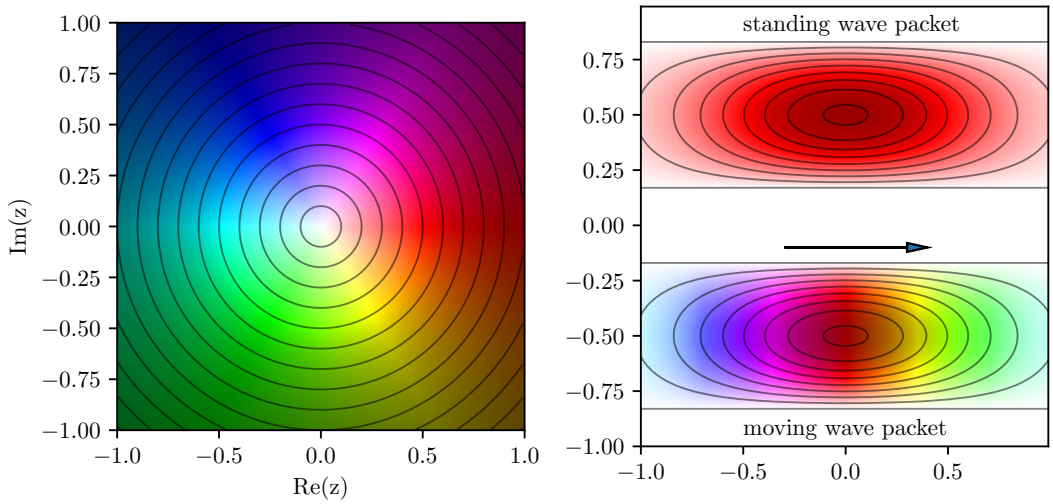

Figure 2.3: Examples of the HSV complex mapping. The left panel shows the simple legend of the HSV mapping near the origin of the complex plane. The right panel shows the examples of two Gaussian wave packets. The wave packet on top has zero horizontal impulse and is real positive, the bottom wave packet has positive horizontal impulse and it is outgoing to the right side of the figure.

with specific colors. For this purpose we have chosen a simple mapping of the complex plane to the HSV color space. The color space has three components, hue, saturation and value, each defined on the real range $[0, 1]$. Since the hue parameter is cyclic, it can be naturally assigned to an angular coordinate. Therefore we first express the complex values in polar coordinates

$$\rho = \quad |z|\,, \qquad \rho \in [0, \infty)\,, \tag{2.26}$$

$$\varphi = \arctan \tfrac{z+\bar{z}}{z-\bar{z}}, \quad \varphi \in [0, 2\pi)\,. \tag{2.27}$$

The mapping of φ to the hue parameter is done by simple rescaling. For the mapping of the radial coordinate, we are left with two remaining dimensions of the color space. We choose to divide the mapping by parameter ζ and map each part to one dimension while maintaining the other constant, at its maximum. Together we get

$$H = \frac{\varphi}{2\pi}, \tag{2.28}$$

$$S = \begin{cases} \frac{\rho}{\zeta}, & \text{for} \rho \leq \zeta, \\ 1.0, & \text{for} \rho > \zeta, \end{cases} \tag{2.29}$$

$$V = \begin{cases} 1.0, & \text{for} \rho \leq \zeta, \\ \frac{\zeta}{\rho}, & \text{for} \rho > \zeta. \end{cases} \tag{2.30}$$

This mapping assigns the white color to the origin and the black color to the infinity, which is suitable for printed plots. Swapping the definition between saturation and value inverts the scale and assigns the black color to the origin and the white color to infinity which may be more suitable for screen projections. The colors with zero saturation (gray scale) are reserved for text, markers and contours.

As an example we show the unit square region around the complex plane origin as the HSV color image in the left panel of the Fig. 2.3, which can be used as a legend to all figures displaying the wave functions as an HSV image. In the right panel of the same figure, we show two examples of simple wave functions. Closer observation of the right panel reveals one important property of the HSV color model. If the wave function represents a bound state, the HSV model displays such a state in shades of only two colors, opposite to each other with respect to the origin. Which colors are used depends solely on the complex phase factor. Since the evolution of a bound state is given only by the phase factor $e^{-i\epsilon t}$, the wave function in the HSV image will simply change these two colors uniformly. The order of the color change is given by a clockwise motion around the origin of the legend (left panel). On the other hand, if the figure represents a moving wave packet with sufficiently large momentum, the magnitude of the wave function changes slowly while the complex phase changes rapidly. Thus the parts of the wave function which are moving in a certain direction can by identified by stripes of color change.

We conclude that within this visualization we may identify the impulse distribution. The local impulse vector is perpendicular to the contour of the same color, the impulse direction is given by the color order and the impulse size is given by the frequency at which the colors change.

2.7 Few notes on the implementation

The numerical solution of the two-dimensional model was implemented in C/C++ code with use of the Intel Math Kernel Library, mainly for vector, matrix and sparse matrix calculus. The main work is done by the sparse linear solver, for which we chose the Intel Parallel Direct Sparse Solver (PARDISO). All libraries are linked in 64-bit integer arithmetics, since the total number of nonzero elements in the LU decomposition of the matrix representation of the Hamiltonian in the H_2^+-like model exceeds the upper bound for 32-bit integers.

The Bessel functions and the Coulomb functions were computed with use of the *coulcc* Fortran 77 library by Thompson and Barnett [1985]. We may note that the package provides a good accuracy with exception of very small values of the coordinate.

The HSV data were processed and plotted with use of the Python3 implementation of the Matplotlib package.

3. Models of electron-molecule collisions

In this chapter we give an overview of the results for three models introduced by Houfek et al. [2006]. We focus on describing the evolution of the two-dimensional wave functions and their comparison with the time-dependent LCP approximation and the comparison of the cross sections with the time-independent results. Probably the best way how to observe the time evolution of any system is to use animations. For the 2D models studied in this chapter such animations are provided as attachments.

The interpretation of the cross section structures follows in Sec. 3.4. The details of the numerical computations, such as the space discretization or the order of the Padé approximation to the evolution operator were already summarized in Sec. 2.5. For all three models we confine the investigated energy range to $[0, 0.2]$ a.u. in which resonant processes we are interested in take place.

3.1 N_2-like model

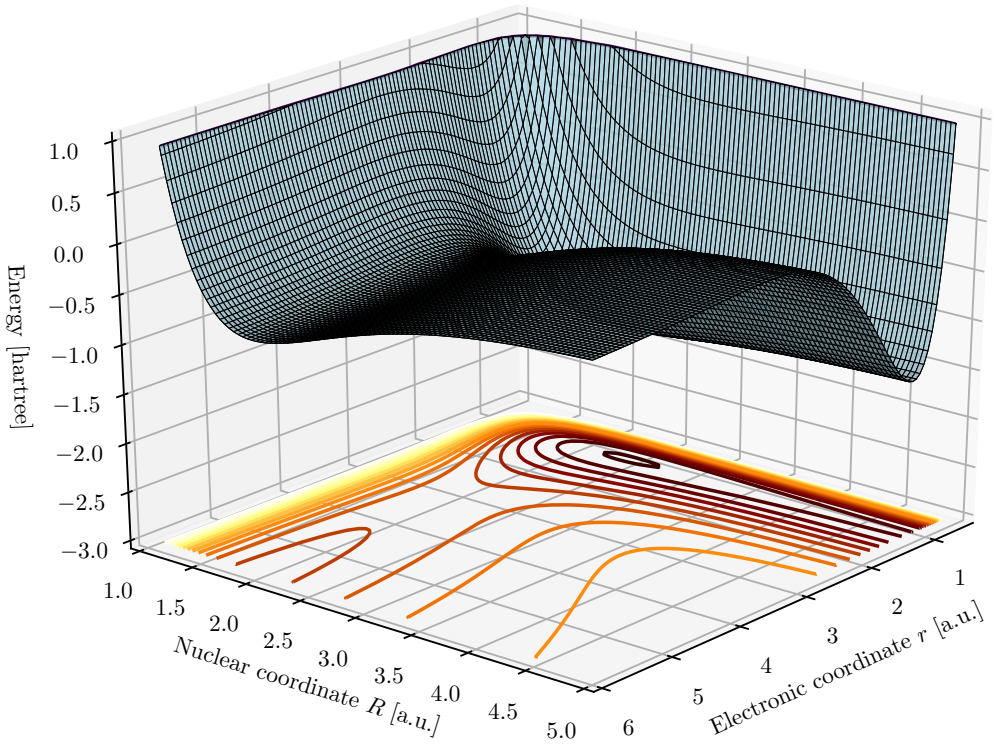

Figure 3.1: The full 2D potential energy surface of the N_2-like model shown at short distances.

The first model we will discuss is the N_2-like model. The shape of the 2D model potential in the interaction region is shown in Fig. 3.1 and the potential energy

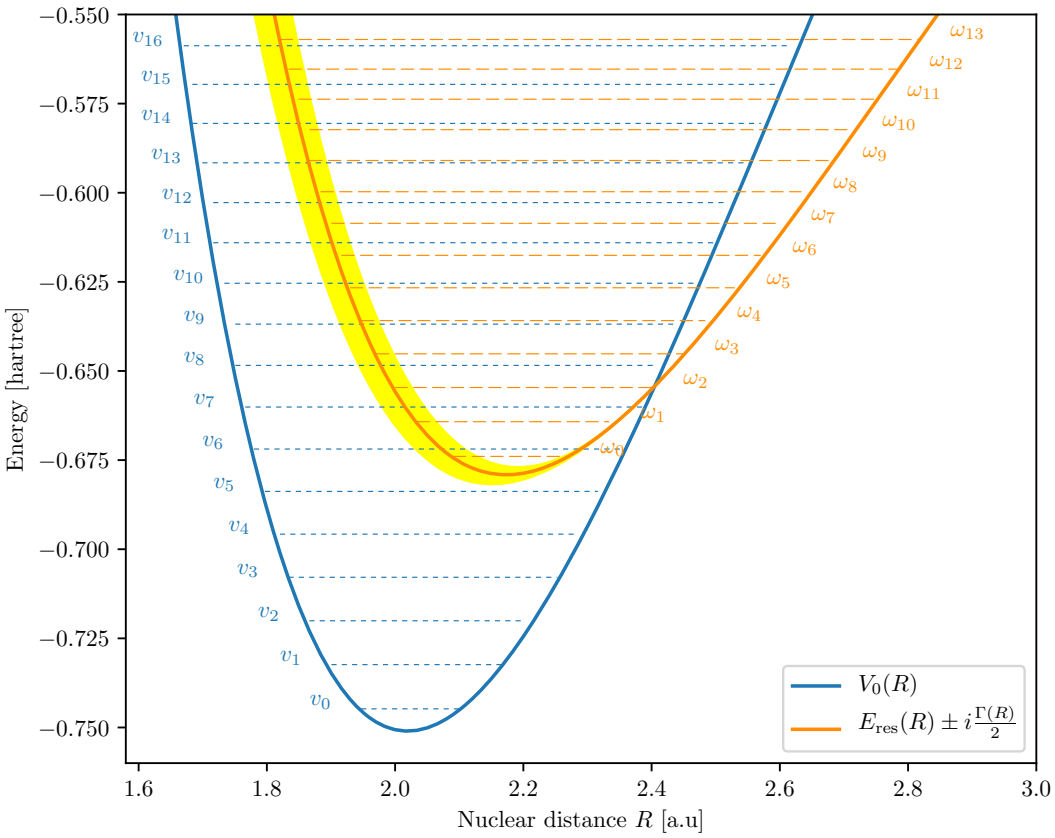

Figure 3.2: The potential energy curves of the LCP approximation for the N_2-like model. The solid blue line shows the potential $V_0(R)$ of the neutral molecule, the solid orange line is the resonant energy curve $E_{\mathrm{res}}(R)$. The yellow shaded area around the resonant energy curve shows the resonance width $\Gamma(R)$. The dashed blue lines with labels v_i represent several vibrational levels of the neutral molecule. The orange dashed lines with labels ω_i represent the resonant energy levels in the potential $E_{\mathrm{res}}(R)$.

curves of the LCP approximation obtained from the fixed-nuclei calculations for this model are shown in Fig. 3.2.

We start the evolution of the 2D model at time $t = 0$ with an incoming wave packet in the VE channel $v_i = 0$ given by (1.41) placed at $r_0 = 45$ with $\sigma = 6.0$ and $p_0 = 0.35$. Note that the mean impulse corresponds to kinetic energy of the electron $p_0^2/2 \simeq 0.06$. The width of the Gaussian wave packet is chosen in such a way that the Fourier-Bessel transform (1.43) covers the whole investigated range but quickly becomes negligible beyond. We present a few snapshots of the evolved two-dimensional wave function in Fig. 3.3 and an animation is attached as Att. 1. At the beginning of the evolution the initial wave packet moves towards the interaction region where a part of it tunnels through the potential barrier at $r \sim 2 - 5$ and is trapped in the well while the remaining part is reflected back and moves to the VE channels. At sufficiently large distances it is absorbed by the complex scaled part of the electronic coordinate to prevent reflections back to the interaction region. The trapped part of the wave packet moves slowly towards larger internuclear distances. Once it reaches distances $R \sim 2.2 - 2.6$

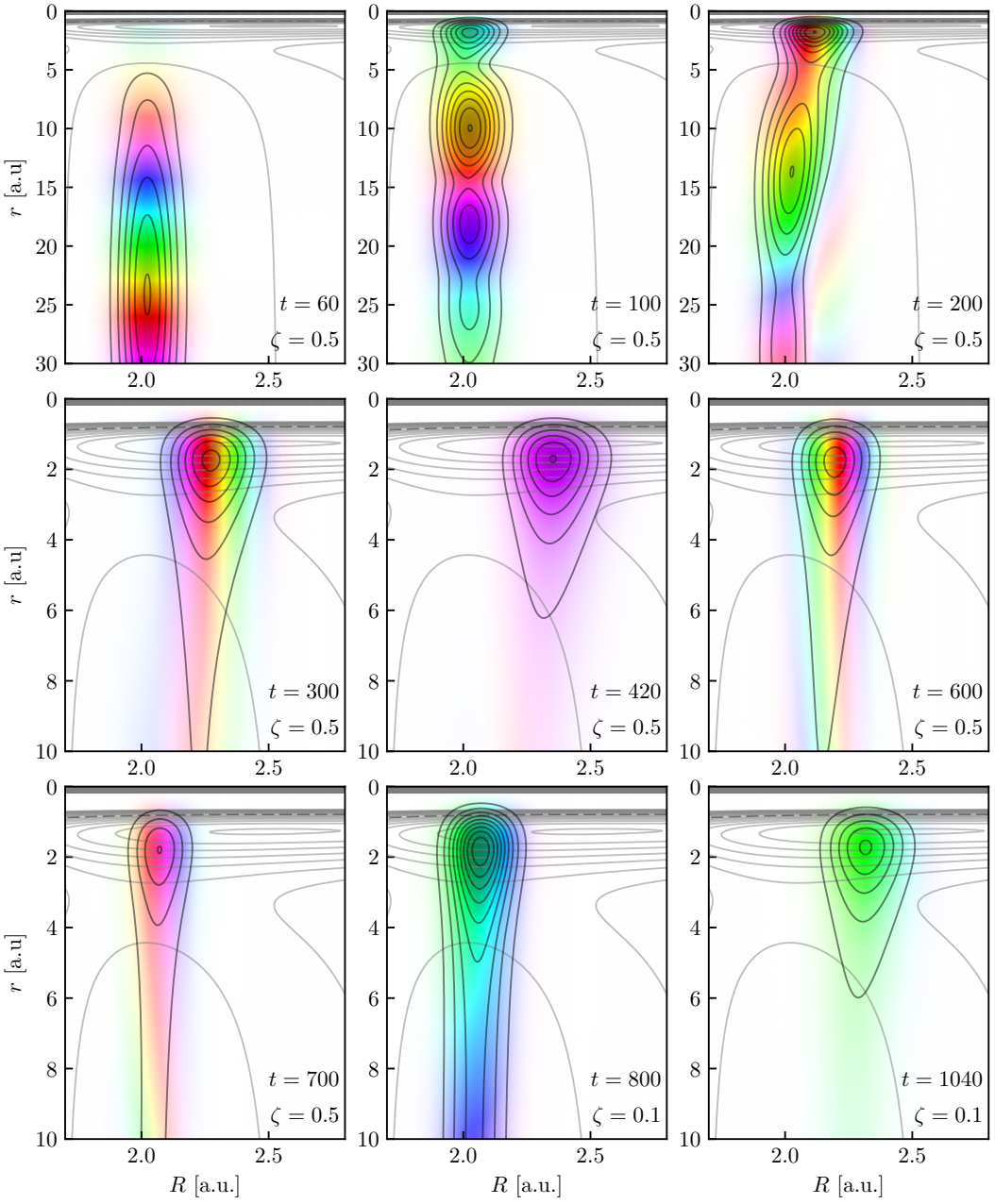

Figure 3.3: Snapshots of the evolved wave function in the HSV images. The light gray contours show the shape of the potential (see Fig. 3.1), the dark grey contours are the wave function amplitude levels and the colors show the complex phase factor scaled to magnitude ζ (see Sec. 2.6 for details). The top panels show the incoming wave packet ($t = 60$), the reflection and tunnelling through the potential barrier ($t = 100$) forming a small wave packet behind this barrier and its motion towards larger internuclear distances ($t = 200$) while the reflected part leaves the interaction region. The middle panels show in detail the motion of the trapped wave packet further along the internuclear coordinate ($t = 300$), near the maximum of the first oscillation ($t = 420$) and its motion back ($t = 600$). The bottom panels show the tunnelling back to VE channels ($t = 700$), further scaled to smaller magnitude ($t = 800$), and near the maximum of the second oscillation ($t = 1040$).

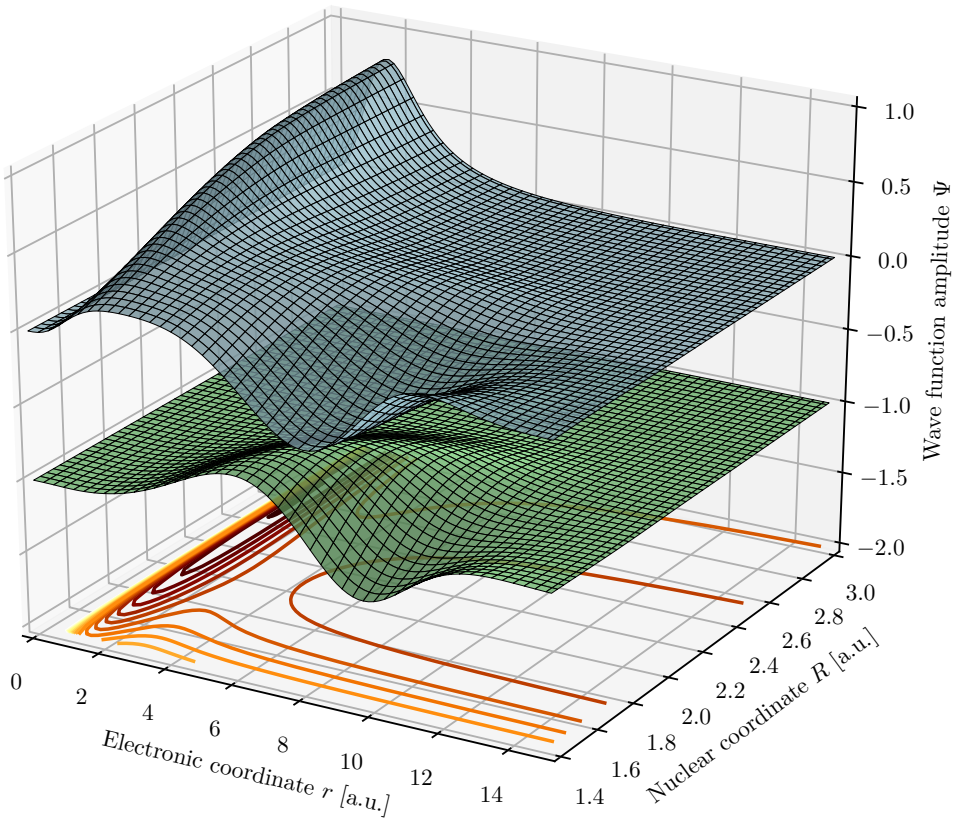

Figure 3.4: The discrete state $\phi_d(R, r)$ as described in Sec. 1.6. The blue surface is the real part and green surface is the imaginary part shifted by -1 on the z-axis. The discrete state is chosen to be real for large values of the nuclear coordinate. As it approaches interaction region the nonzero imaginary part emerges. Note that the right panel axes are rotated from Fig. 3.1 for better visibility.

it is repelled back due to the increasing potential energy. At $t \sim 420$ the wave packet reaches the maximal value of the internuclear distance around $R \sim 2.4$. Since the dissociative channel is not accessible for the given energy range the whole wave packet is reflected back towards the interaction region. This motion is often referred to as the *boomerang motion*. In the interaction region a part of the wave packet penetrates back to the VE channels and leaves the interaction region. A small part of the wave packet remains behind the barrier and repeats the motion in the nuclear coordinate.

To compare the evolution of the two-dimensional wave function with the evolution of the wave function from the LCP approximation we project the 2D wave function to the physical choice of the discrete state for each internuclear distance. The real and imaginary parts of the discrete state are shown in Fig. 3.4. Note that the imaginary part is nonzero only for internuclear distances smaller than R_c, i.e. in the region where the energy of the fixed-nuclei electronic state $E_{\text{res}}(R)$ is above the neutral molecule potential energy $V_0(R)$. In Fig. 3.5 we present the comparison of the time evolution of these projections with the LCP approximation wave function. Note that the figure provides only information about relative

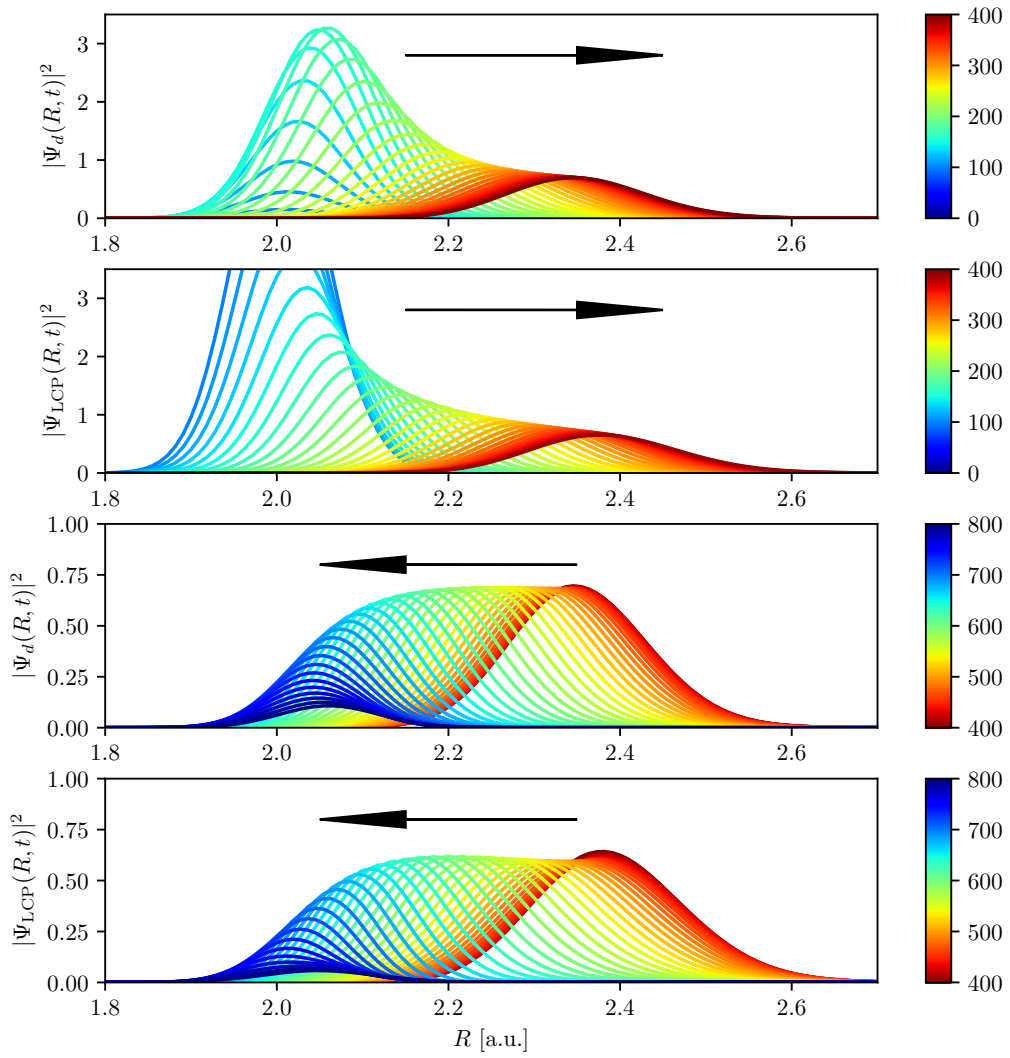

Figure 3.5: Comparison of the time-evolution of the 2D wave function projected on the discrete state with the LCP wave function. The time is marked by the color of the curve as indicated in the box on the right side of the panels. The incident wave packets were synchronized by $\Delta_t^{LCP} = 101$. The LCP wave packet was rescaled to match the projection normalisation at $t = 419$, i.e. multiplied by factor 328 (see Fig. 3.22 and the Sec. 3.4 for details).

changes in time since the LCP wave packet was rescaled and synchronized to the projections (see Sec. 3.4 for details). The significant differences occur at the beginning of the evolution, since the process of the trapping in the potential well is not included in the LCP approximation for it describes only the evolution of the trapped wave packet. The shapes of the functions are very similar otherwise.

We have set the cutoff time to $t_{\mathrm{cutoff}} = 4000\,\mathrm{a.u.} \simeq 100\,\mathrm{fs}$ since the wave function amplitude in the interaction region becomes negligible. As mentioned before we have tested three methods for evaluation of the S-matrix elements. The test functions for the Tannor & Weeks approach have to be placed far enough, not only from the interaction region but also from the initial state so their overlap is negligible. We have set the positions to $r_0 = 75$ with the mean impulse $q_0 = 0.39$

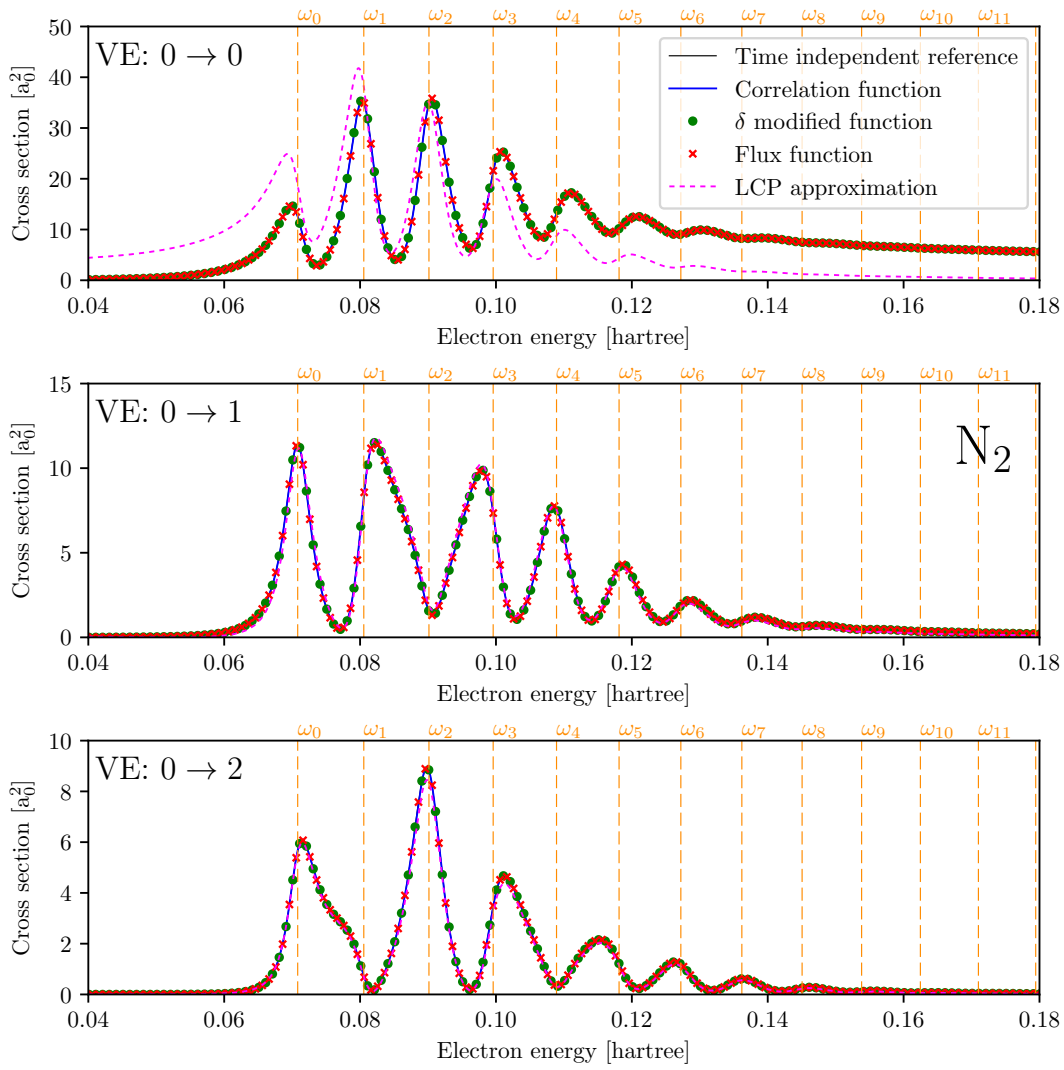

Figure 3.6: The cross sections of the elastic and two inelastic processes at the cut-off time $t_{\text{cutoff}} = 4000$ obtained by three methods of S-matrix evaluation and by the LCP approximation are compared with the time-independent approach of the 2D model. The dashed orange lines with labels ω_i marks positions of the resonant energy levels in the potential $E_{\text{res}}(R)$ (see Fig. 3.2 for details).

and the width $\sigma = 6.0$. The position of the δ-functions in the modified Tannor & Weeks approach and of the surface flux integration were both set to $r_0 = 75$ as well. The resulting cross sections for three selected VE transitions are shown in Fig. 3.6 along with the time-independent calculation and LCP approximation results. The time-dependent calculation is in very good accordance to the reference time-independent result for all three studied methods. Note that the results are converged even at channel thresholds where the energy of outgoing electron is close to zero (for example the VE $0 \to 8$ cross section in Fig. 3.6 at the threshold energy $E \simeq 0.096$ goes to zero). The only noticeable inaccuracy of the time-dependent approach appears in the elastic scattering process for very low energies (not shown in Fig. 3.6). This inaccuracy results from Eqs. (1.60) and (1.61) when evaluated numerically close to zero energy.

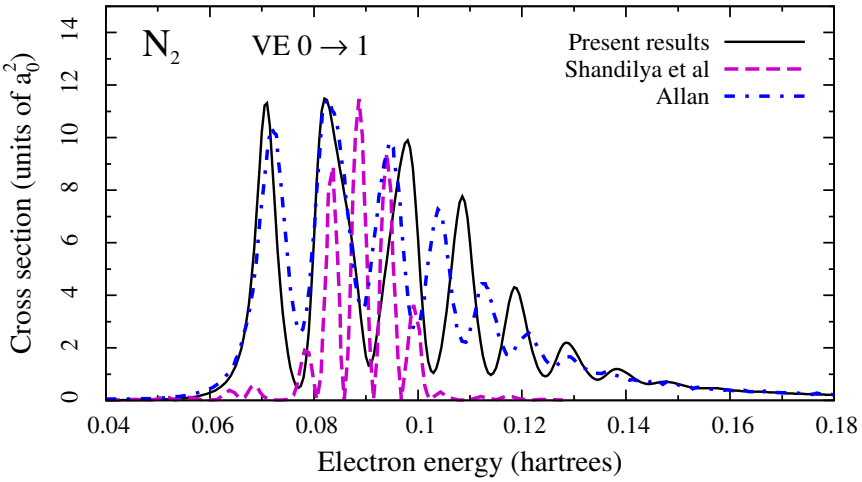

Figure 3.7: Comparison of the VE $0 \rightarrow 1$ cross section for the N_2-like model with the result of Shandilya et al. [2012] and with the experimental result of Allan [1985].

To complete the discussion of results for N_2-like model we show in Fig. 3.7 a comparison of the VE cross section for transition $0 \rightarrow 1$ calculated using the time-dependent approach presented in this thesis with the result of Shandilya et al. [2012] and with the experimental cross section of Allan [2005a] multiplied by a factor to have the same maximal value of the highest peak as our results. Although the 2D model was not meant for direct comparison with experiment one can see that the 2D N_2-like model reproduces the basic features of the cross section rather well. Lower frequency of the oscillations at higher energies is due to a slightly incorrect shape of the potential energy curve of the molecular anion N_2^- to which the model parameters were fitted. On the other hand, the cross section of Shandilya et al. [2012] differs quite significantly from our and experimental result although it should be the same as ours because the model is the same. Because our time-dependent results agree perfectly with the time-independent ones from Houfek et al. [2006] we believe that the calculations of Shandilya et al. are incorrect. We should also note here that although it is not explicitly written in the paper we suspect that Shandilya et al. [2012] also normalized their theoretical cross sections (for each VE transition *separately*) to get the same maximal value of the highest peak as in Houfek et al. [2006]) because their cross sections for all VE transitions have always the same maximal value as results in Houfek et al. [2006], which in our opinion makes further comparison of our results with their cross sections useless.

3.2 NO-like model

The second investigated case is the NO-like model. As in the previous case we show the image of the potential in the interaction zone in Fig. 3.8 and the derived potentials $V_0(R)$ and $E_{\mathrm{res}}(R)$ in Fig. 3.9. Note that the minimum of $E_{\mathrm{res}}(R)$ is now behind the crossing point of the potential curves forming an *outer well* (outside

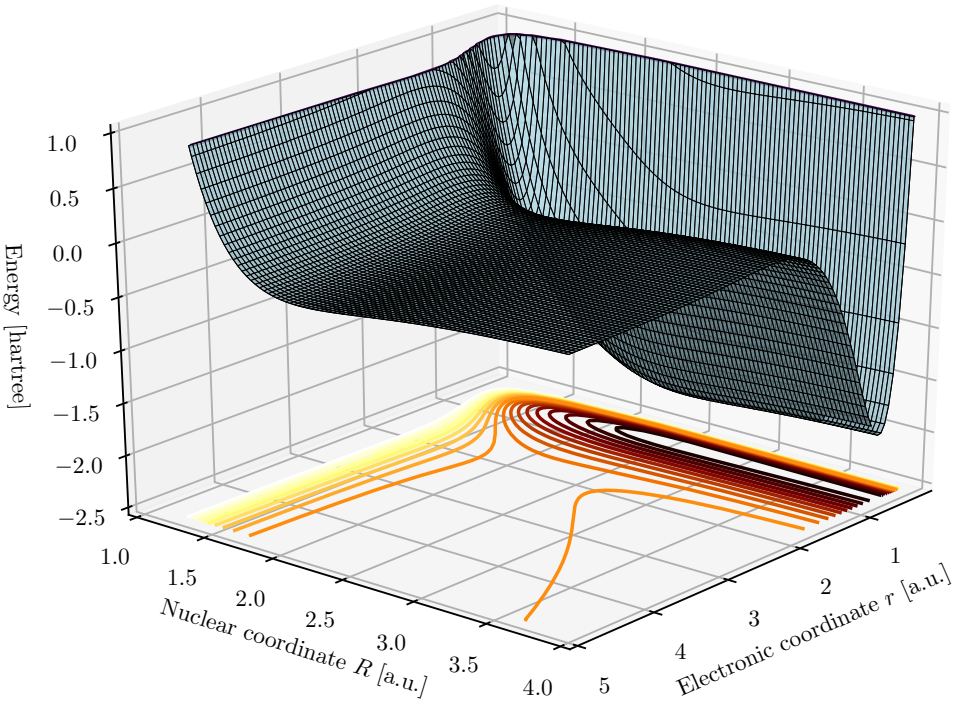

Figure 3.8: The full 2D potential energy surface of the NO-like model shown at short distances.

the autodetachment region). Therefore a longer living states in this outer well can be expected to form during the dynamics. Also note that since in this model the DA channel is open for energies $E \gtrsim 0.175$, we have to extend the discretization in the internuclear coordinate, details may be found in Sec. 2.5. As in the previous case we start the evolution with the initial state in the VE channel $v_i = 0$ with the initial position of the Gaussian wave packet placed at $r_0 = 45$, with the mean impulse $p_0 = 0.35$ and the width $\sigma = 6.0$.

The beginning of the evolution is practically the same as in the previous case. The initial wave packet reaches the interaction region where it hits the potential barrier. A part of the wave packet penetrates to the potential well and the other part is reflected to the VE channels, leaves the interaction region and being consumed by the imaginary part of the complex scaled electronic coordinate it quickly vanishes. Meanwhile the trapped wave packet starts to move in the internuclear coordinate. We present images of the evolved wave function in Fig. 3.10 and Fig. 3.11 and also an animation is attached as Att. 3. The noticeable difference from the N_2-like model appears at the end of the boomerang motion when the returning wave packet penetrates back to the VE channels. The wave packet has no longer one smooth peak in the internuclear coordinate. The second peak appears at $R \sim 2.4$ where the minimum of the potential energy curve $E_{\mathrm{res}}(R)$ is, see Fig. 3.9. The difference is even more visible during the second oscillation since the overall amplitude of the wave packet is significantly decreased by the part which already left to the VE channel space. This observation suggests that the second peak is a longer living part of the trapped wave packet.

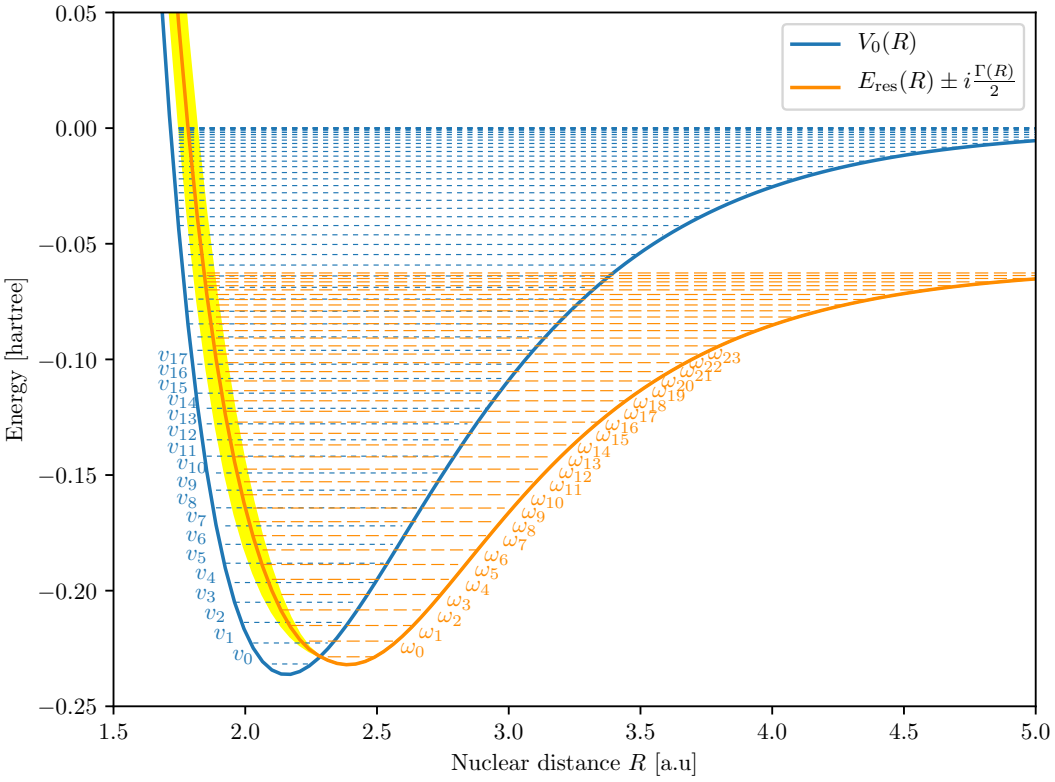

Figure 3.9: The potential energy curves $V_0(R)$ (solid blue line) and $E_{\mathrm{res}}(R)$ (solid orange line) with the resonance width $\Gamma(R)$ as the yellow shaded area around $E_{\mathrm{res}}(R)$ for the NO-like model. The dashed blue lines with several labels v_i represent vibrational levels of the neutral molecule. The orange dashed lines with labels ω_i represent the resonant energy levels in the potential $E_{\mathrm{res}}(R)$.

That the dynamics of this model slightly differs from the N_2-like model is nicely visible from the projections onto the discrete state. This state is very similar to the discrete state used in the N_2-like case, with only small differences in the interaction region where it changes slightly more rapidly with the decreasing internuclear distance. Dependence of the discrete state on the internuclear distance is shown in Fig. 3.12.

The evolution of the projections along with the LCP approximation wave function may be observed in Fig. 3.13. The top panel shows the process of initial electron capture into the resonant state and the motion of the captured part of the wave packet towards larger internuclear distances. The capture is again naturally missing in the LCP approximation. The LCP wave function was rescaled and synchronized to match the projection at the maximal internuclear distance (see again Sec. 3.4 for details). Note that the maximal mean internuclear distance is slightly different for the projection ($R_{max} \simeq 2.75$) and for the LCP approximation ($R_{max} \simeq 2.7$). However, this maximal distance for projections is strongly dependent on the parameters of the initial wave packet (the higher the mean energy of the wave packet the larger R_{max}). The second pair of panels shows the motion back to the interaction region and the process of decaying of the resonant state. Another significant difference between the projections and the LCP approximation is visible in the region around $R \approx 2.4$, magnified in the

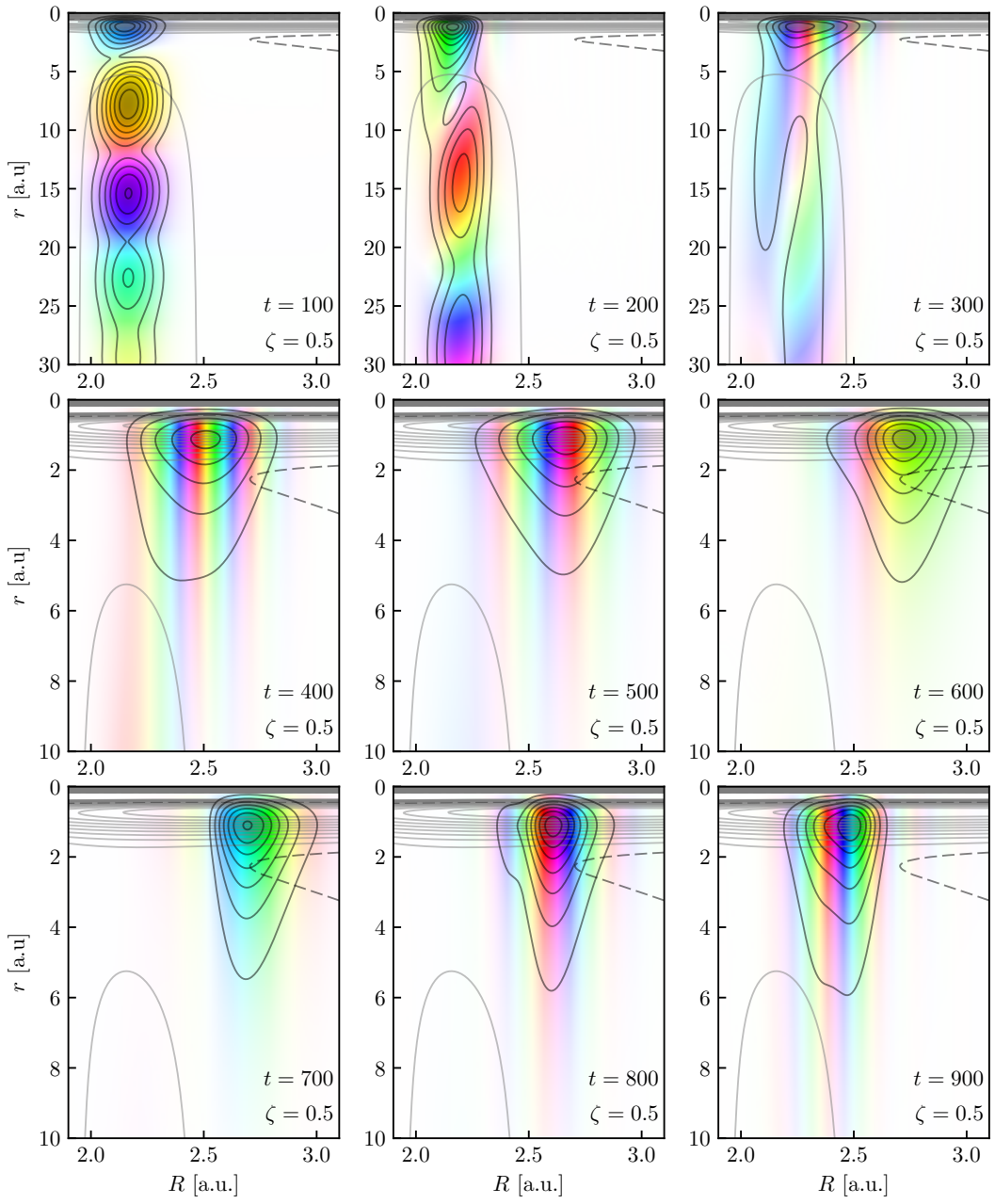

Figure 3.10: Snapshots of the evolved wave function in the HSV images. The top panels show the initial scattering ($t = 100$, $t = 200$) with tunnelling through the potential barrier, the reflection to the vibrational excitation channels and beginning of the first molecular oscillation ($t = 300$). The middle panels from top show in detail the boomerang oscillation along the nuclear coordinate ($t = 400$, $t = 500$) up to the point near the maximum of the first oscillation ($t = 600$) around $R \simeq 2.75$. The bottom panels show the motion back to smaller nuclear distances ($t = 700$, $t = 800$, $t = 900$) with visible deformation of the wave packet close to the location of the outer potential well at $R \sim 2.4$.

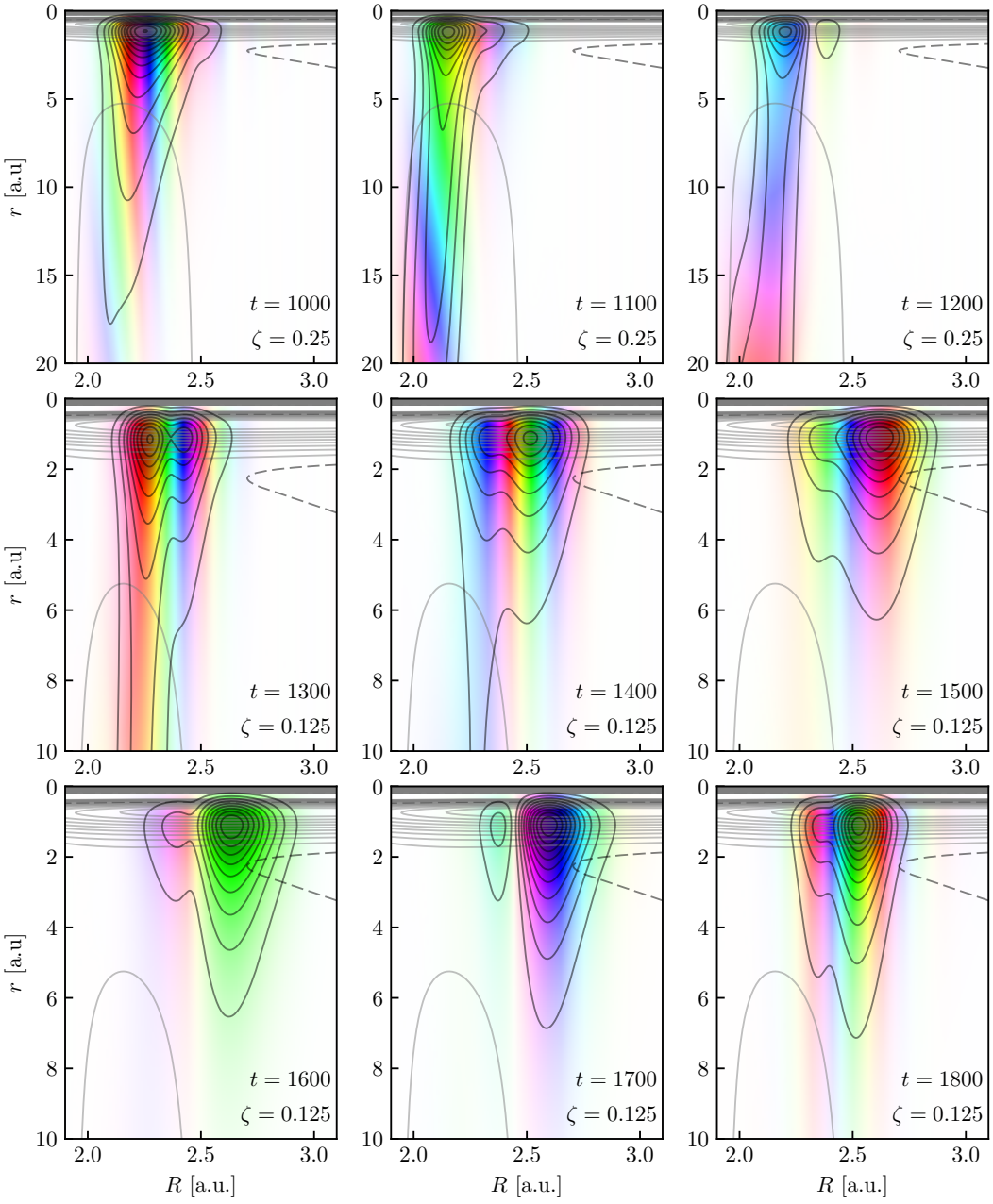

Figure 3.11: Snapshots of the evolved wave function in the HSV images, continuation from the Fig. 3.10. The top panels show the process of the tunnelling back to the vibrational excitation channels ($t = 1000$, $t = 1100$, $t = 1200$) revealing the second peak of the wave packet behind the potential barrier. The middle panels show the forward motion during the second oscillation ($t = 1300$, $t = 1400$ and $t = 1500$) displaying an even more pronounced deformation of the wave packet. The bottom panels show the wave packet close to the second turning point of the second oscillation ($t = 1600$ and $t = 1700$), where the second peak becomes practically isolated revealing the location of the outer well minimum, and again the backward motion towards smaller nuclear distances ($t = 1800$).

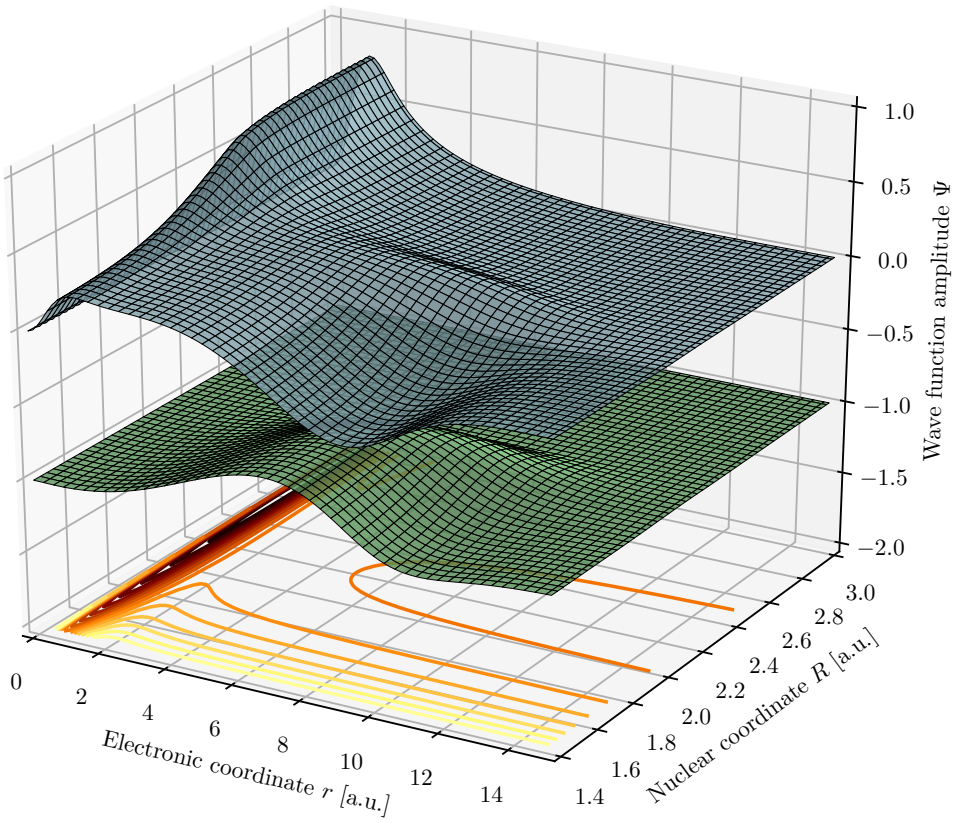

Figure 3.12: The discrete state $\phi_d(R, r)$ as described in Sec. 1.6. The blue surface is the real part and green surface is the imaginary part shifted by -1 on the z-axis. The discrete state is chosen to be real for large values of the nuclear coordinate. As it approaches interaction region the nonzero imaginary part emerges. Note that the right panel axes are rotated from Fig. 3.8 for better visibility.

third pair of panels, which points to the failure of the LCP approximation.

As the evolution continues the two-dimensional wave function decays more slowly suggesting presence of a long living state. The cutoff time was set to $t_c = 35000$ since the normalization of the two-dimensional wave function dropped enough, below 10^{-9}. We present the cross sections for a few VE channels and the DA channel obtained by all three methods described above compared to the time-independent calculation and LCP approximation in Fig. 3.14. Again the results agree with the time-independent ones for almost all investigated energies. Small distortions appear at the very low energies, as it should be expected since the time-dependent calculation would need much longer time to provide accurate results, and also in the DA cross section which is very small and all numerical inaccuracies are enhanced. Surprisingly, some of the very low energy inaccuracies may also originate from too large evolution time step Δt if the Fourier-Bessel coefficients decay too slowly with increasing energy. The very low energy contributions may be distorted by contributions of high energies for which $E_1 \Delta t \approx E_0 \Delta t + 2\pi$, where E_0 is some energy from the investigated range. This effect can be either suppressed by a different choice of the initial wave packet energy distribution or

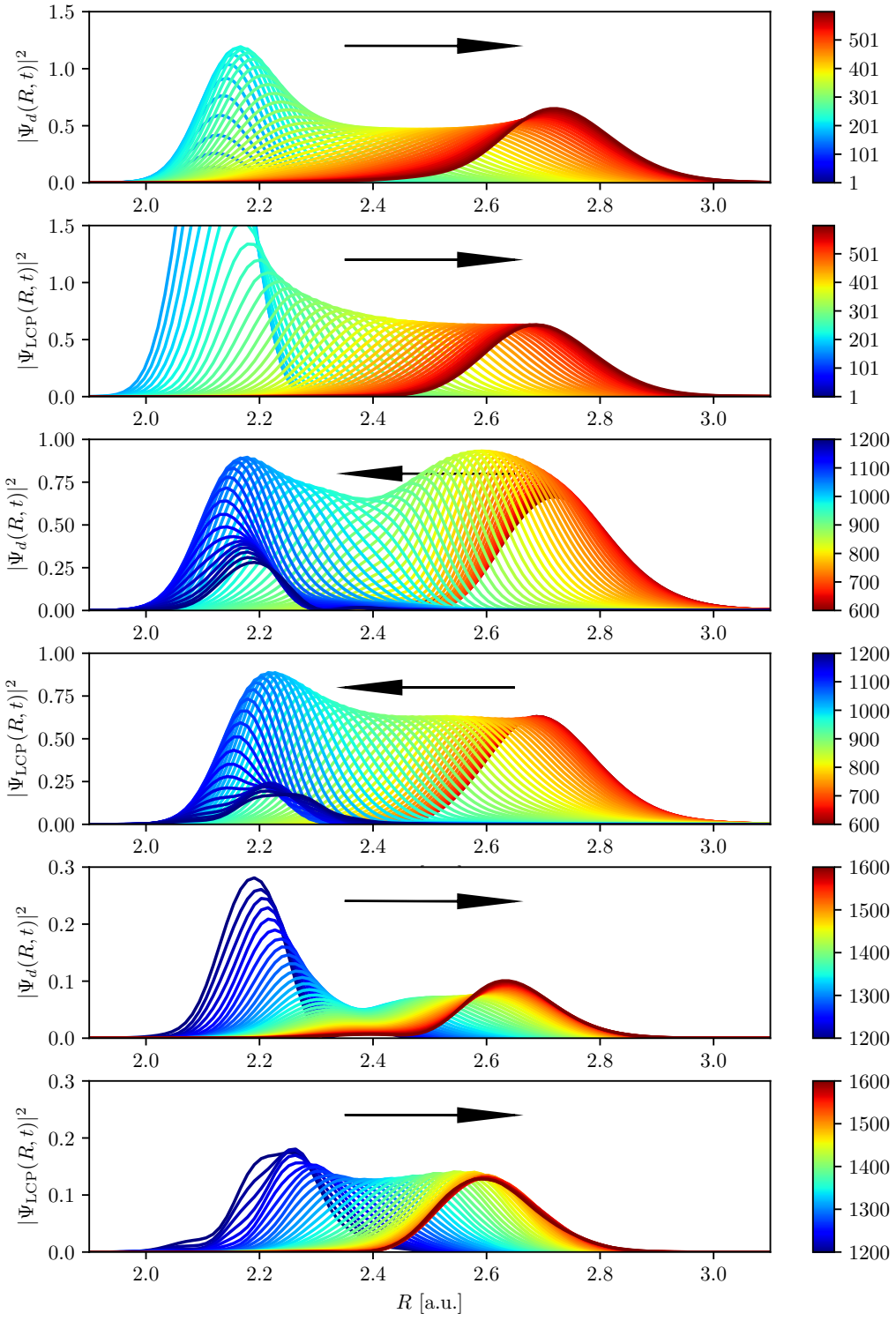

Figure 3.13: Comparison of the time evolution of the 2D wave function projected on the discrete state with the LCP wave function for the NO-like model. The LCP wave packet was synchronized with the projection by $\Delta_t^{LCP} = 176$. For better comparison we have rescaled the LCP wave packet to the projection in time $t = 637$ by factor 287 (see Fig. 3.24 and Sec. 3.4 for explanation).

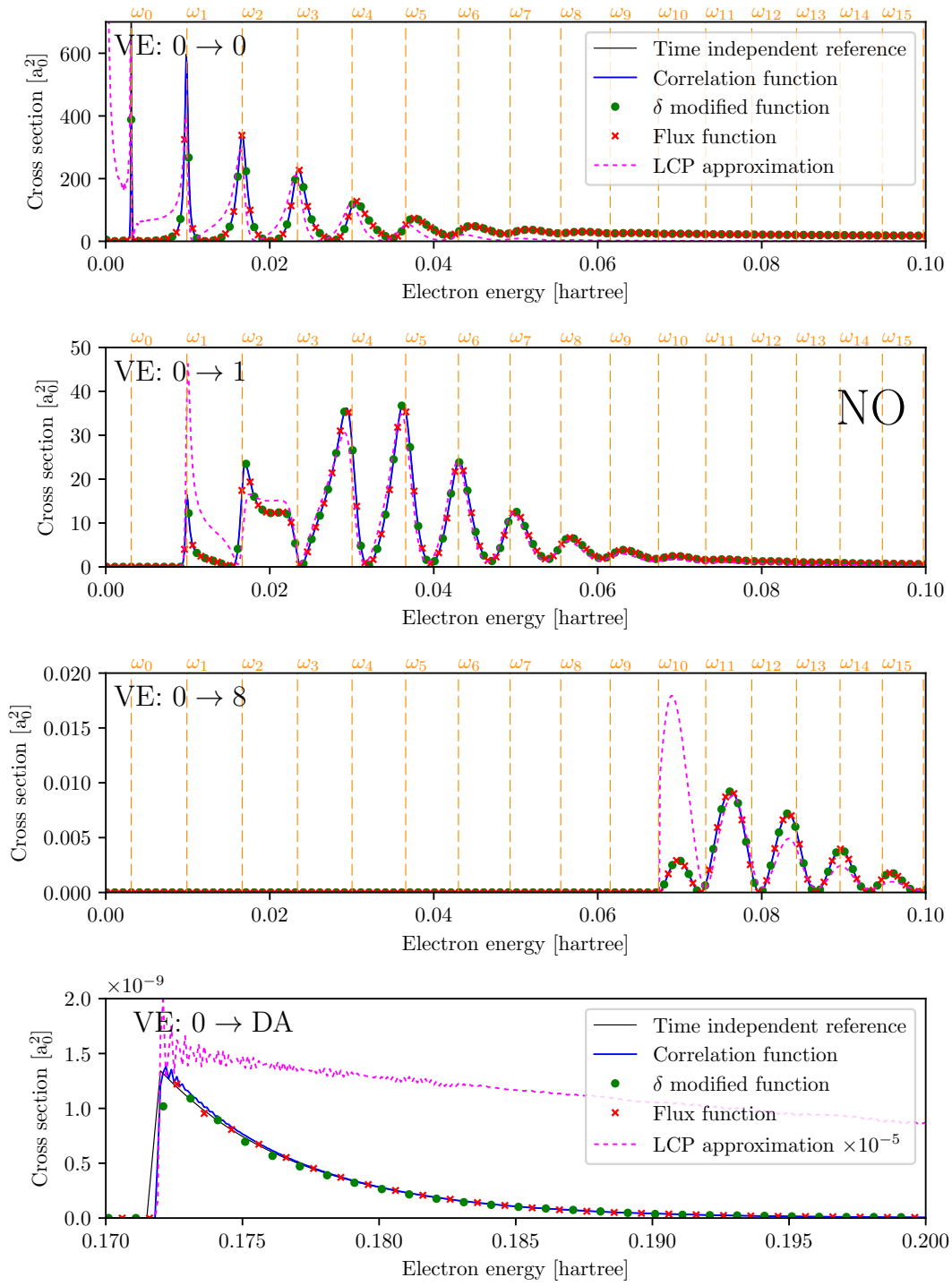

Figure 3.14: The cross sections of the elastic process, vibrational excitation $0 \to 1$ and $0 \to 8$, and the dissociative attachment for the NO-like model at the cutoff time $t_c = 35000$ obtained by three methods of the S-matrix evaluation along with the LCP approximation results compared to the time-independent approach of the 2D model.

by decreasing the time step. Even though the values of the DA cross sections are very small the results agree well with the time-independent ones for all three methods. The results could be even further improved by a better choice of the initial parameters, but since we did not expect to get any new information from such large computations we have not pursued the goal any further. We should also note that the DA cross sections may be obtained more easily if computed separately from the VE cross sections since the grid parameters and time step may be chosen differently resulting in lower computational requirements and less computational time.

3.3 F_2-like model

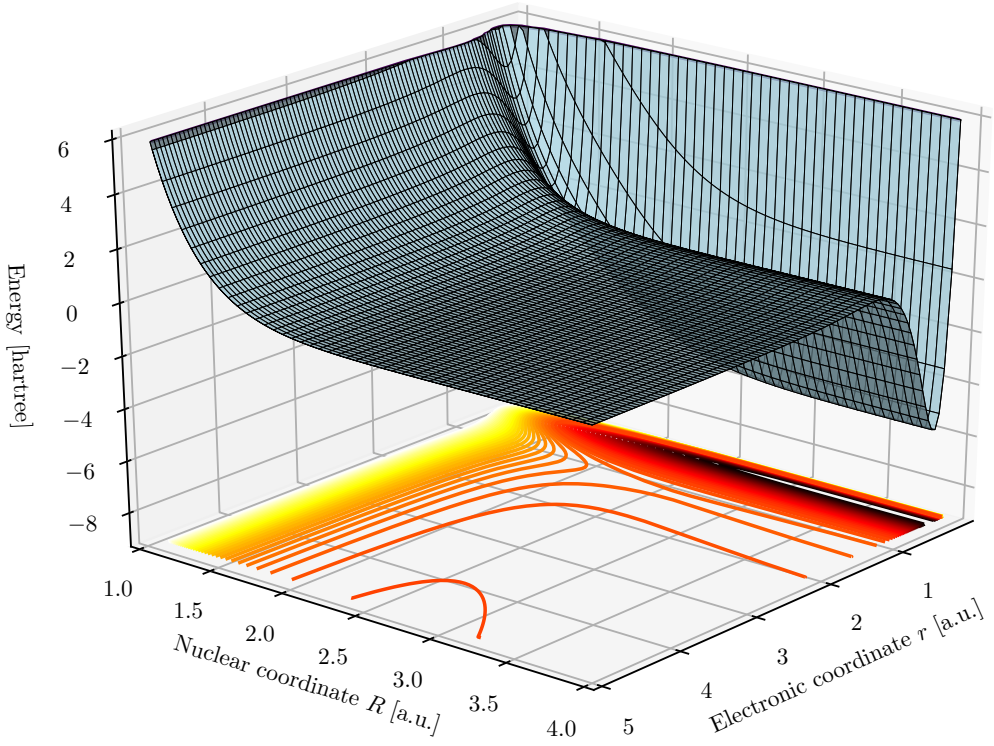

Figure 3.15: The full 2D potential energy surface of the F_2-like model shown at short distances.

The F_2-like model significantly differs from the previous two models. As one may see from Fig. 3.15 the full 2D potential forms a deep but very narrow well close to the origin of the electronic coordinate, therefore the electronic grid was refined mainly in the region $[0, 1]$. As one can see from the LCP approximation potentials in Fig. 3.16 the DA channel is accessible for all energies and the negative molecular ion potential $E_{\text{res}}(R)$ crosses the neutral molecule potential $V_0(R)$ very steeply resulting also in significant increase of nuclear coordinate grid density (see Sec. 2.5 for details).

The parameters of the initial wave packet and time evolution were set to the same values as in the NO-like model. We present a few snapshots from the

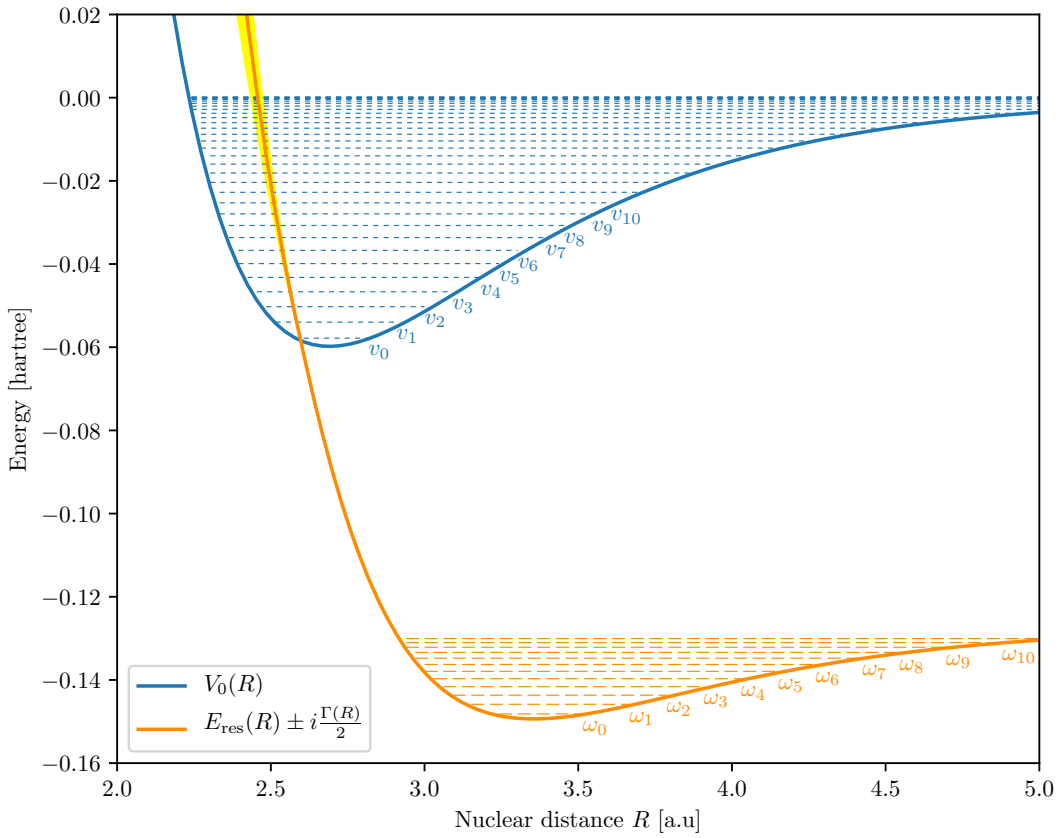

Figure 3.16: The potential energy curves $V_0(R)$ (solid blue line) and $E_{\mathrm{res}}(R)$ (solid orange line) with the resonance width $\Gamma(R)$ as the yellow shaded area around $E_{\mathrm{res}}(R)$ for the F_2-like model. The dashed blue lines with several labels by v_i marks the positions of vibrational excitation levels, the orange dashed lines with labels ω_i marks the positions of levels in resonant potential E_{res}.

evolution of the wave packet for this model in Fig. 3.17 and an animation, which is attached as Att. 5. After the wave packet hits the interaction region at $t \simeq 80$, a part of it is reflected by the potential barrier, another part penetrates through and becomes trapped creating a smooth peak close to $r \sim 0.5$ and $R \sim 2.6$.

After roughly around 50 units of evolution time a distortion of the trapped wave packet appears. Since the trapped part of the wave packet is located in the region of a steep potential slope in the nuclear coordinate, it starts to move quickly towards larger internuclear distances. At the same time the part of the wave function which is reflected to the VE channels is slowly withdrawing. Since the complex phase of the outgoing waves to the VE channels changes slowly with the nuclear coordinate and the complex phase of the waves outgoing to the DA channel changes quickly, their presence in the same region results in an interference. Once the trapped wave packet moves to larger internuclear distances the interference is no longer visible. Since there is no potential barrier in the direction of increasing internuclear distance, the wave packet cannot be reflected back and therefore it moves further to the DA channel resulting in dissociation of the molecule.

To compare the full dynamics with the LCP approximation, we again pro-

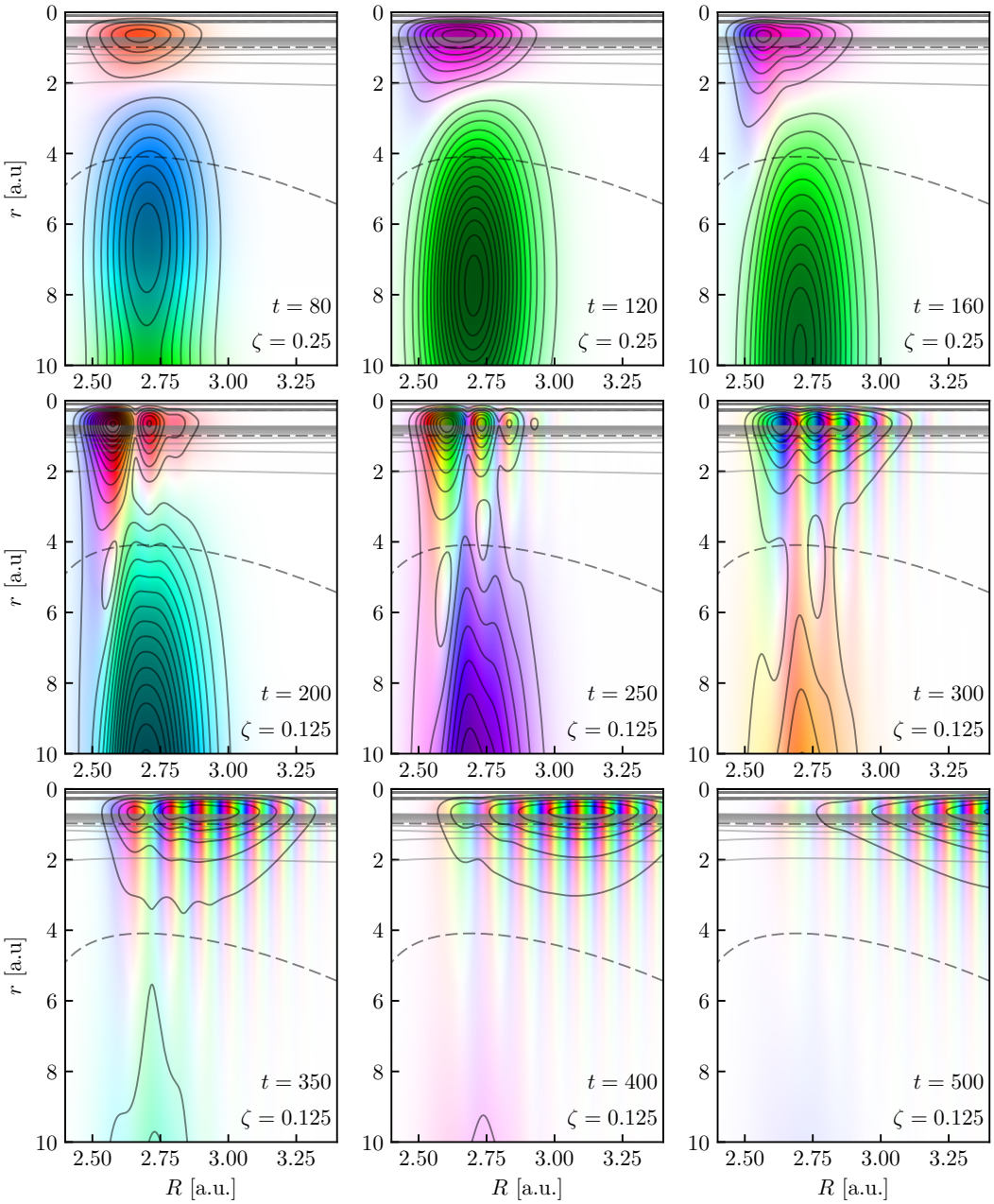

Figure 3.17: Snapshots of the evolved wave function in the HSV images. The top panels show the initial reflection of the incident wave packet ($t = 80$), which is quite similar to the NO-like case, the deformation of the trapped wave packet ($t = 120$ and $t = 160$) as the wave packet tunnels back to the vibrational excitation channels and starts to move toward the dissociative attachment channel. The middle panels show the interference between both processes forming two peaks ($t = 200$) and even more peaks as the packet moves towards larger internuclear distances ($t = 250$ and $t = 300$). Note the high complex phase frequency indicating the large impulse of the wave packet. The bottom panels show the separation of the processes ($t = 350$) decreasing the interference and smoothening of the trapped wave packet ($t = 400$ and $t = 500$) and its motion towards the dissociative attachment channel.

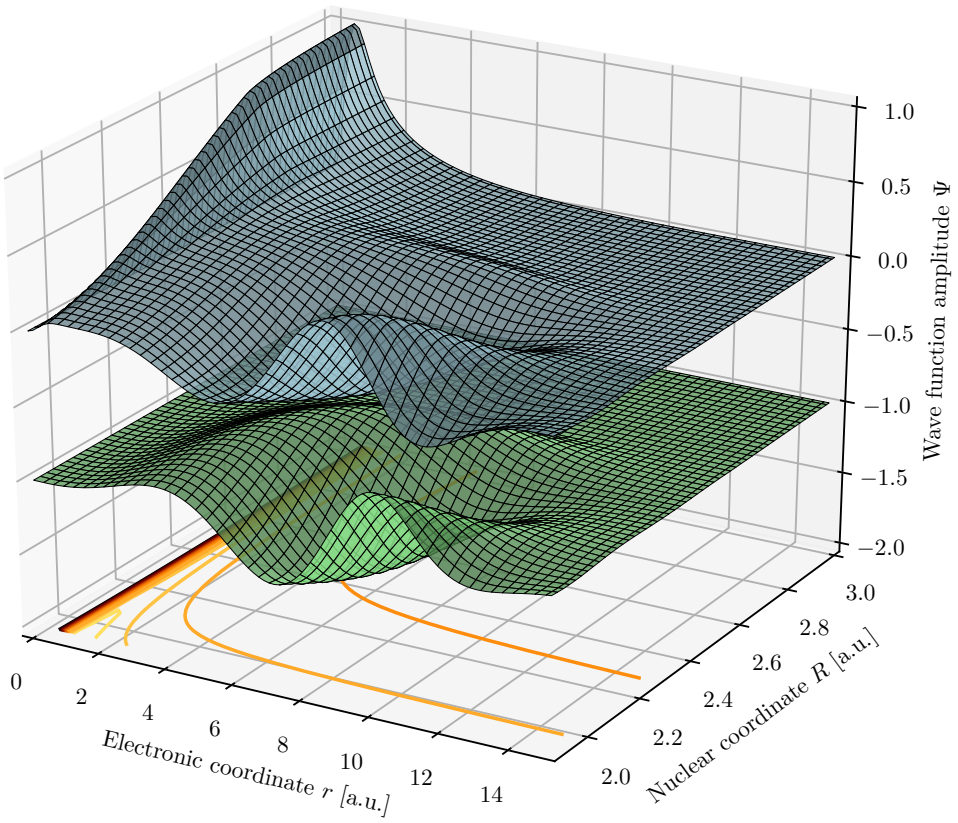

Figure 3.18: The discrete state $\phi_d(R, r)$ as described in Sec. 1.6. The blue surface is the real part and green surface is the imaginary part shifted by -1 on the z-axis. The discrete state is chosen to be real for large values of nuclear coordinate. As it approaches interaction region the nonzero imaginary part emerges Note that the right panel axes are rotated from Fig. 3.15 for better visibility.

jected the 2D wave function on the discrete state, which is shown in Fig. 3.18. It is clear that this state changes rapidly with decreasing internuclear distance once the potential energy $E_{\text{res}}(R)$ crosses the neutral molecule potential $V_0(R)$.

The interference described above in the 2D dynamics is also clearly visible in the evolution of the projection on the discrete state in Fig. 3.19 where its comparison with the LCP wave function is shown. Note that there is no interference in the LCP approximation, which is natural since the interaction with the electronic continuum is approximated by a simple imaginary part of the local potential $V_{\text{res}}(R)$. As the evolution continues and the interference in the projections disappears, the wave packets seem to be similar although the projection is much wider than the LCP wave function. Since the width of the trapped wave packet is strongly dependent on the initial 2D wave packet, there is no physical significance in this difference.

Since the motion is aperiodic the cutoff time $t_c = 15000$ was chosen simply to be large enough for the outgoing waves to leave the real region of the grid. The cross sections in Fig. 3.20 show again a good accordance of the time-dependent results with the time-independent ones for almost all energies. Only for very low

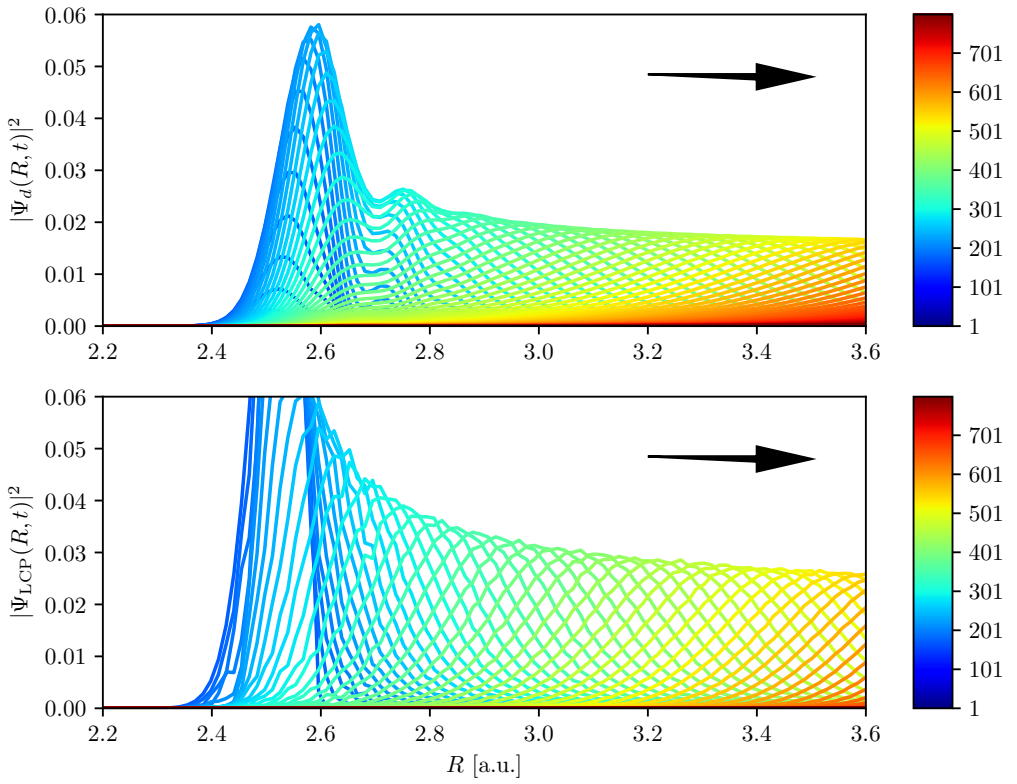

Figure 3.19: Comparison of the 2D wave function projection on the discrete state with the LCP wave function for the F_2-like model. The LCP wave packet was synchronized with the projection to match in the beginning of the outgoing motion by $\Delta_t^{LCP} = 177$. The LCP wave packet was rescaled for better comparison. The evolution time is marked by the color of the curve corresponding to the color bar on the right side of the panels.

energies the elastic and DA cross sections are slightly distorted. These inaccuracies are due to the initial setup of parameters and finite integration time and could be further improved with cost of the computational resources. Again, since we did not expect any new information to be obtained we have not pursued this goal any further.

The comparison of the 2D model cross sections with the LCP approximation results was already deeply investigated in Houfek et al. [2008a] and therefore we leave the topic with a simple comment that the interference during the evolution of the 2D wave function manifests the nontrivial nature of the motion, i.e. it is a direct result of breaking the Born-Oppenheimer approximation. It also reveals the inability of the LCP approximation to describe such systems where the process of the penetration through the barrier and initial repulsion is not sufficiently separated in time, i.e. where there is a non-negligible overlap between the outgoing waves to the VE channels and DA channel already in motion.

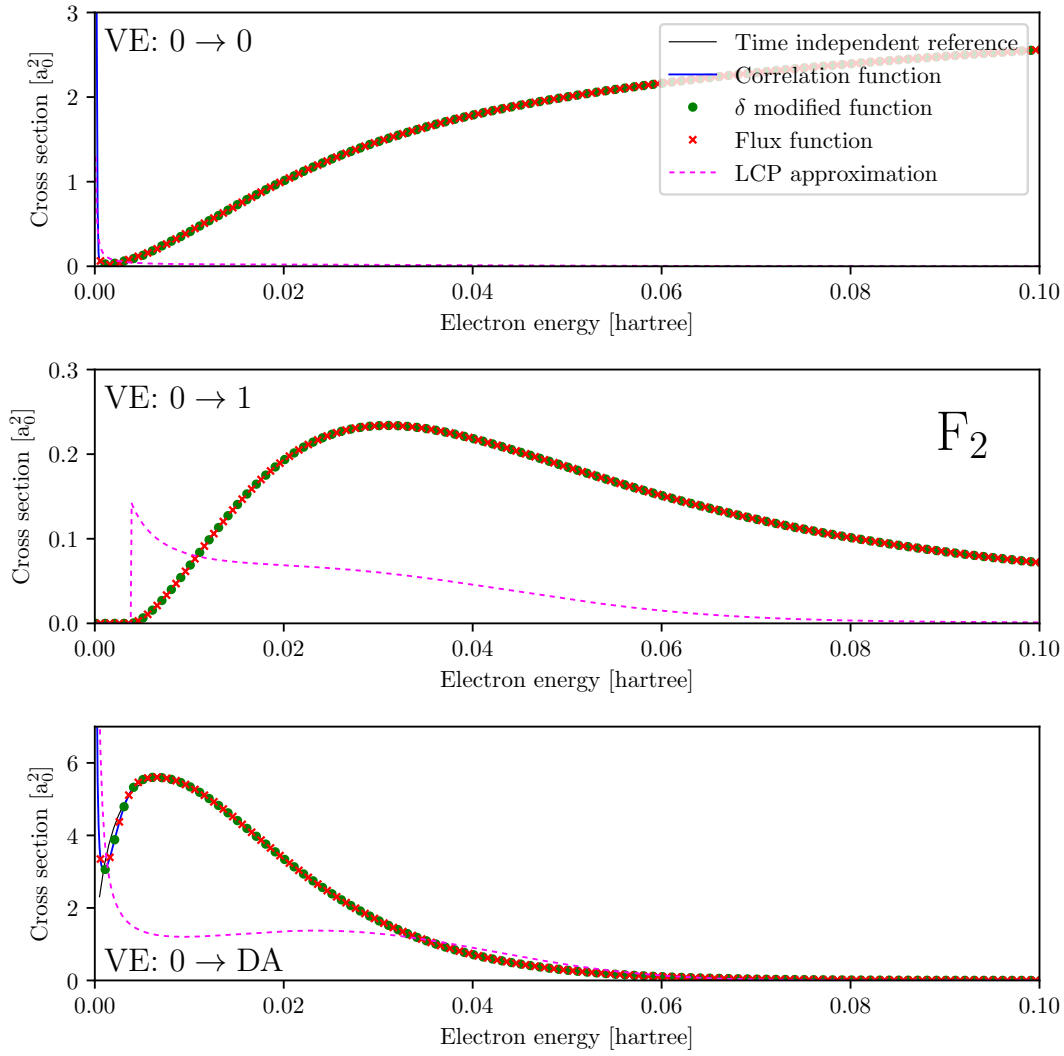

Figure 3.20: The elastic, VE $0 \rightarrow 1$ and DA cross sections for the F_2-like model at the cutoff time $t_c = 15000$ obtained by three approaches to the S-matrix evaluation.

3.4 Interpretation of the cross sections

The actual vibrational excitation cross sections of resonant collisions of electrons with diatomic molecules N_2 (Berman et al. [1983], Huo et al. [1987], Allan [1985, 2005a]) and NO (Trevisan et al. [2005], Allan [2005b]) are very similar to ones obtained using the N_2-like and NO-like models shown in Fig. 3.6 and 3.14. The oscillatory structures appearing in the VE cross sections are often explained as an interference of the fast direct decay of the electronic resonant state of the negative molecular ion in the autodetachment region (to the left from the crossing point of the potential energy curves of the neutral molecule and the anion, see Fig. 3.2 and 3.9) with the time-delayed decay of this state due to vibrational motion out of the autodetachment region and back. This mechanism is usually referred to as the *boomerang* model (Birtwistle and Herzenberg [1971], Dubé and Herzenberg [1979]) which is a valid explanation of oscillatory structures in the VE cross sections for certain systems (for example for H_2 molecule Horáček et al. [2006]), but it does

not explain the origin of irregularities in these structures. Most of the calculations on real systems are actually performed within the time-independent framework in which the explanation of the structures and especially of appearance of the asymmetric peaks is much more complicated (see e.g. Houfek et al. [2008b]).

Here we take an advantage of the time-dependent formulation of the two-dimensional model to study in detail the origin of the oscillatory structures including the asymmetric peaks appearing in the VE cross sections in Fig. 3.6 and 3.14. We will demonstrate that the simple *boomerang* mechanism provides an explanation only to a regular oscillatory structure but to explain asymmetry of peaks one has to consider further vibrational motion of the negative molecular ion and even long-lived states in the potential well outside the autodetachment region.

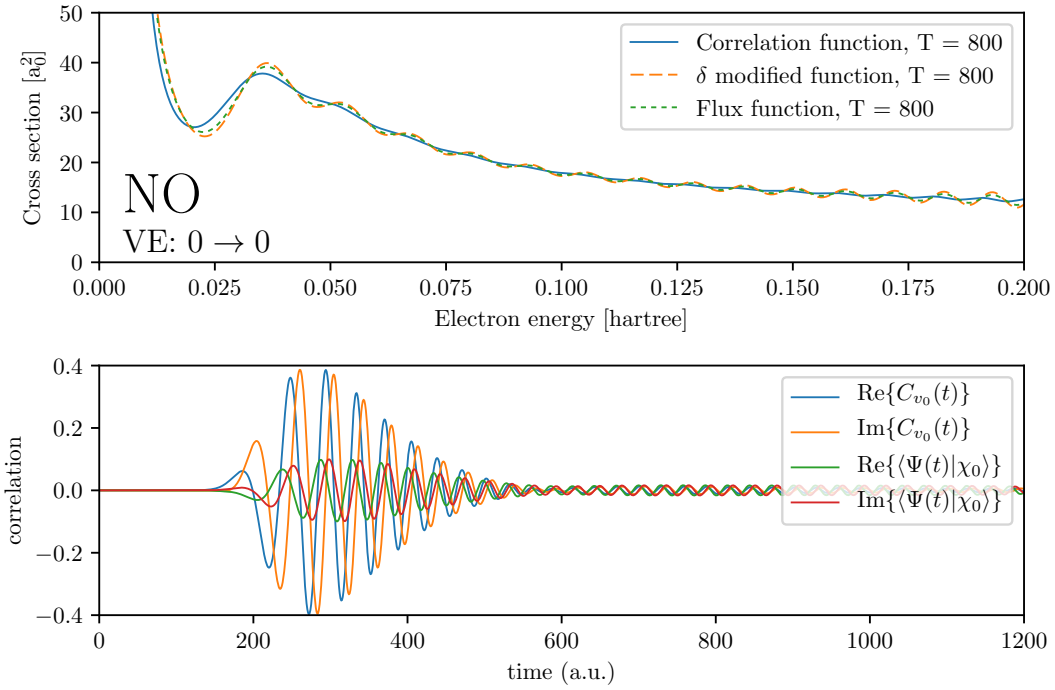

Figure 3.21: Comparison of the elastic scattering cross sections obtained by three investigated methods at time $t = 800$ for the NO-like model (top panel) and comparison of correlation function $C_{v_0}(t)$ and δ-modified correlation function $\langle\Psi(t)|\chi_{v0}\rangle$ generating the cross sections.

Before we proceed with the interpretation of the cross sections we discuss the comparison of the approaches to the S-matrix computation. Up to this point we have treated all three investigated methods equally since the results at the cutoff time were practically the same. The key difference arises once we try to compare the results at early times. As an example we show the elastic cross section evaluated at $t = 800$ for the NO-like model in Fig. 3.21 along with two examples of generating correlation functions up to the time of the evaluation of these cross sections. Note that this time there is a significant difference between the three methods. Both the Tannor & Weeks method with the δ-function and the probability flux approach oscillate while the original method of the Tannor & Weeks oscillates only at higher energies. It is even possible to further improve the results

of Tannor & Weeks method by modifying the parameters of the test functions or of the initial state. We conclude that the time-energy Fourier transform in the Tannor & Weeks method is much smoother. Therefore it is more suitable for the early cutoff time computations and in this section we will show results only for this method.

3.4.1 N_2-like model

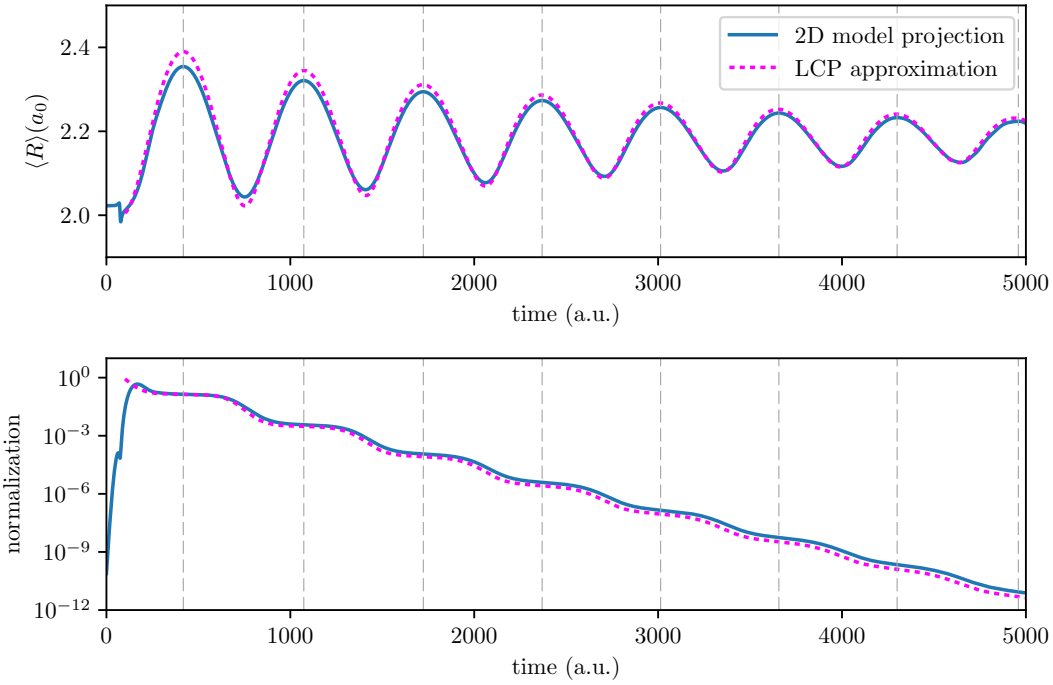

Figure 3.22: The mean internuclear distance of the projections and the LCP wave packet (top panel) and their normalization (bottom panel) as functions of the evolution time for the N_2-like model. The vertical dashed lines mark the positions of the maxima of the mean internuclear distance. The position of the first maximum at $t = 419$ was used to synchronize the evolution within the LCP approximation by $\Delta_t^{LCP} = 101$ and also to adjust normalization of the LCP wave packet for better comparison.

We start with results for the N_2-like model. In Fig. 3.22 we show the evolution of the mean internuclear distance and the normalization of both the projections onto the discrete state and the LCP approximation wave packet. We have used the position of the maximal value of the mean internuclear distance (marked by vertical dashed lines) to synchronize the motion of the projections with the LCP wave packet and we rescaled the normalization of the LCP wave packet for better comparison. It is clear that the motion in the nuclear coordinate resembles the motion of a damped harmonic oscillator. From the distance between two maxima of the mean internuclear distance we were able to determine the period of the nuclear motion to $T \approx 655$ a.u. ≈ 16 fs. The normalization curves (bottom panel of Fig. 3.22) show decrement only in the moments of minimal mean internuclear distance. This behavior corresponds to the fact that the wave packet can tunnel

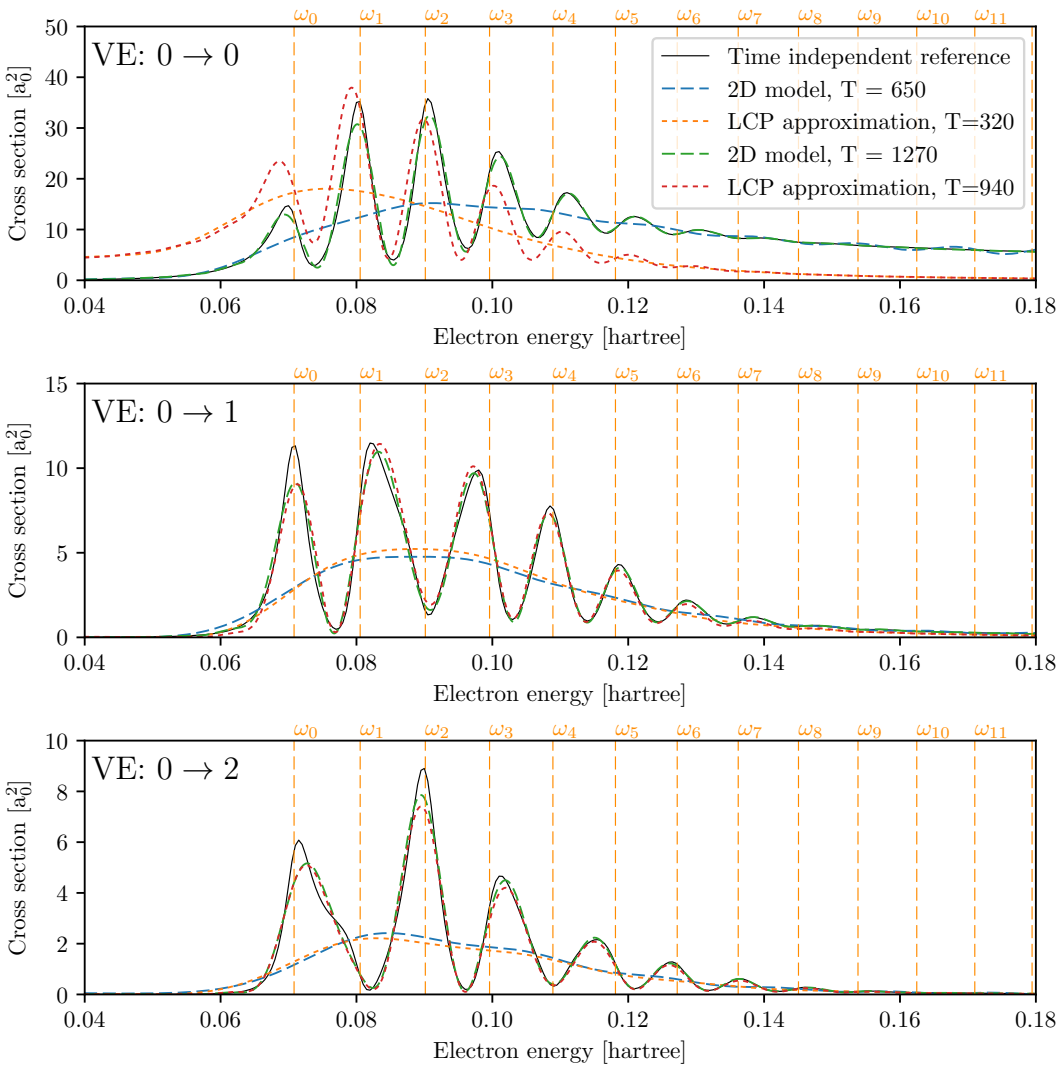

Figure 3.23: The elastic and VE cross sections for two chosen transitions evaluated at significant values of the evolution time for the N_2-like model. The dashed lines stand for the 2D model, the dotted lines for the LCP approximation.

through the potential barrier back to the VE channels only in the autodetachment region close to the minimum of the neutral molecule potential $V_0(R)$, in this case at $R \sim 2$. Since at the time around $t \sim 400 - 500$ the wave packet is at its maximum mean internuclear distance around 2.4 and the normalization is almost constant, forming a wide plateau, we may assume the contribution to the cross sections from the passed evolution to be well separated from the subsequent contributions. The cross sections of the full 2D model evaluated at the end of the plateau at $t = 650$ are marked by dashed blue lines and for LCP at $t = 320$ by orange dotted lines in Fig. 3.23. As we can see the initial reflection of the wave function produces one wide and smooth peak in all VE cross sections except unphysical peaks at threshold energies due to slower motion of corresponding outgoing waves. A similar shape appears in the LCP cross sections although it is slightly misplaced for the elastic scattering.

As the evolution continues another contribution from the so called *boomerang*

motion is added to the cross sections. Since it is again well separated from the subsequent contributions we may take a look at the updated cross sections at the moment of the maximal mean internuclear distance at $t = 1270$ for the 2D model and at $t = 940$ for the LCP approximation. The results are shown in Fig. 3.23 by the green dashed and red dotted curve for the 2D and LCP model, respectively. This time a series of symmetrical peaks appears modulating the previously obtained shape. Note that the time-independent results are still slightly different from the ones obtained after the first vibrational period, mostly where the structures are asymmetrical. Apparently at least one more contribution (after another vibrational period) is needed to form the proper shape of the cross sections.

During the further evolution the normalization quickly decreases. As the normalization drops by 8 orders of magnitude around the time $t_c = 4000$ further contributions to the cross sections become negligible and there is no point in evolving the wave functions any further. Thus we set t_c as the cutoff time. The resulting cross sections were already discussed in Sec. 3.1. The animation with the above described process is attached as Att. 2.

3.4.2 NO-like model

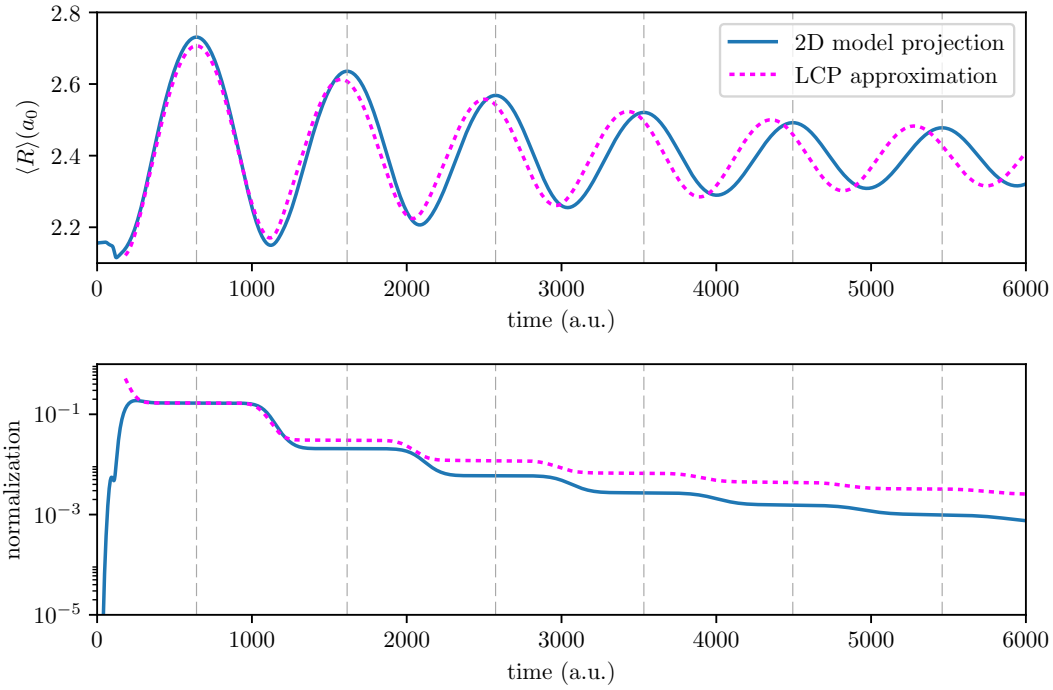

Figure 3.24: The mean internuclear distance of the projections and LCP wave packet (top panel) and their normalization (bottom panel) as functions of the evolution time. Both mean internuclear distance and normalization curves were synchronized by the position of the first maximum of the mean internuclear distance at $t = 637$, with $\Delta_t^{LCP} = 176$.

Again we start with the comparison of mean internuclear distances and normalization for both the projection of the 2D wave function onto the discrete

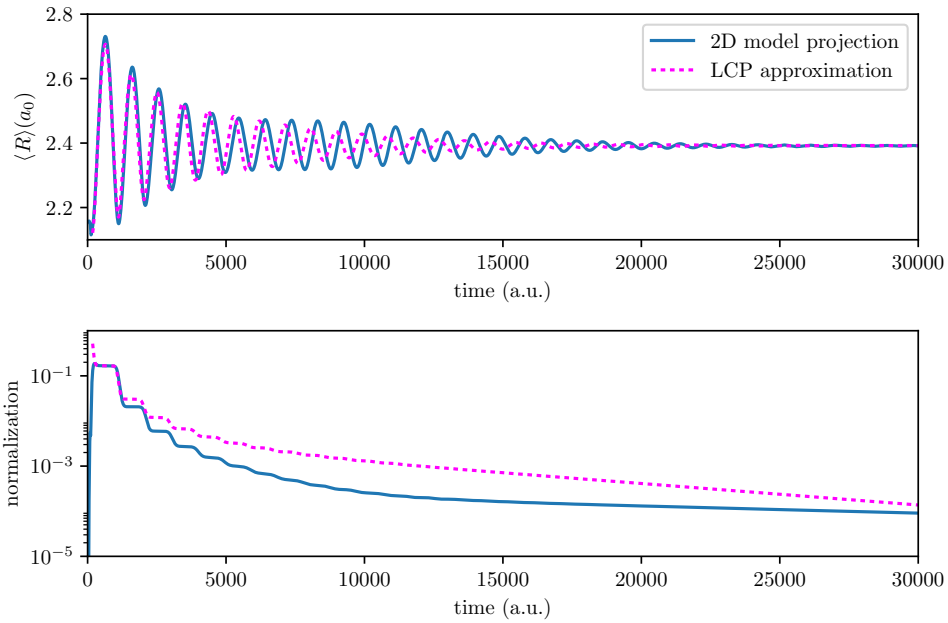

Figure 3.25: The same as in Fig. 3.24 but for times up to 30000 a.u.

state and the LCP wave packet, which are arranged in Fig. 3.24 and 3.25. Note that the motion in both models again resembles the damped harmonic oscillator. Also note that this time the frequency of the oscillations and the speed of the normalization decrement differ significantly for the 2D model and the LCP approximation which means that the nuclear dynamics for this system is not properly described by the LCP approximation and leads to a failure of the LCP approximation at lower energies (see Fig. 3.14). We have determined the period of the nuclear motion of the 2D wave packet to $T \approx 971$ a.u. ≈ 23 fs. The motion takes place at distances from $R \sim 2.1$ to $R \sim 2.8$. The positions of the maximal mean internuclear distance again served as the separation points of the contributions to the cross sections. Decrease of the normalization in the NO-like model is much slower than in the N_2 case and thus much more contributions have to be included to obtain the converged cross sections. Another striking feature in Fig. 3.25 is a long, linear (in logarithmic scale) tail of both 2D and LCP curves. Such behavior points to an existence of a long-lived state which, as we will see, is responsible for a high, narrow peak in the elastic cross section.

For clarity of figures we omit results obtained within the LCP approximation in the following discussion. The interpretation of the structures within the LCP approximation would be very similar. As in the N_2 case the initial reflection contribution to the cross section at $t = 900$ produces a wide smooth peak in each VE channel shown as solid blue curves in Fig. 3.26 where the elastic (upper panels) and VE $0 \rightarrow 1$ (lower panels) cross sections integrated up to particular times are presented. The results obtained for short times show pronounced threshold peaks due to slow motion of corresponding outgoing waves. These peaks later disappear as more contributions from slower outgoing waves are included.

At the time $t = 1800$ there are two contributions in the cross sections (orange dashed curve), the initial reflection of the wave packet without nuclear motion is interfering with the wave packet leaving the autodetachment region after the

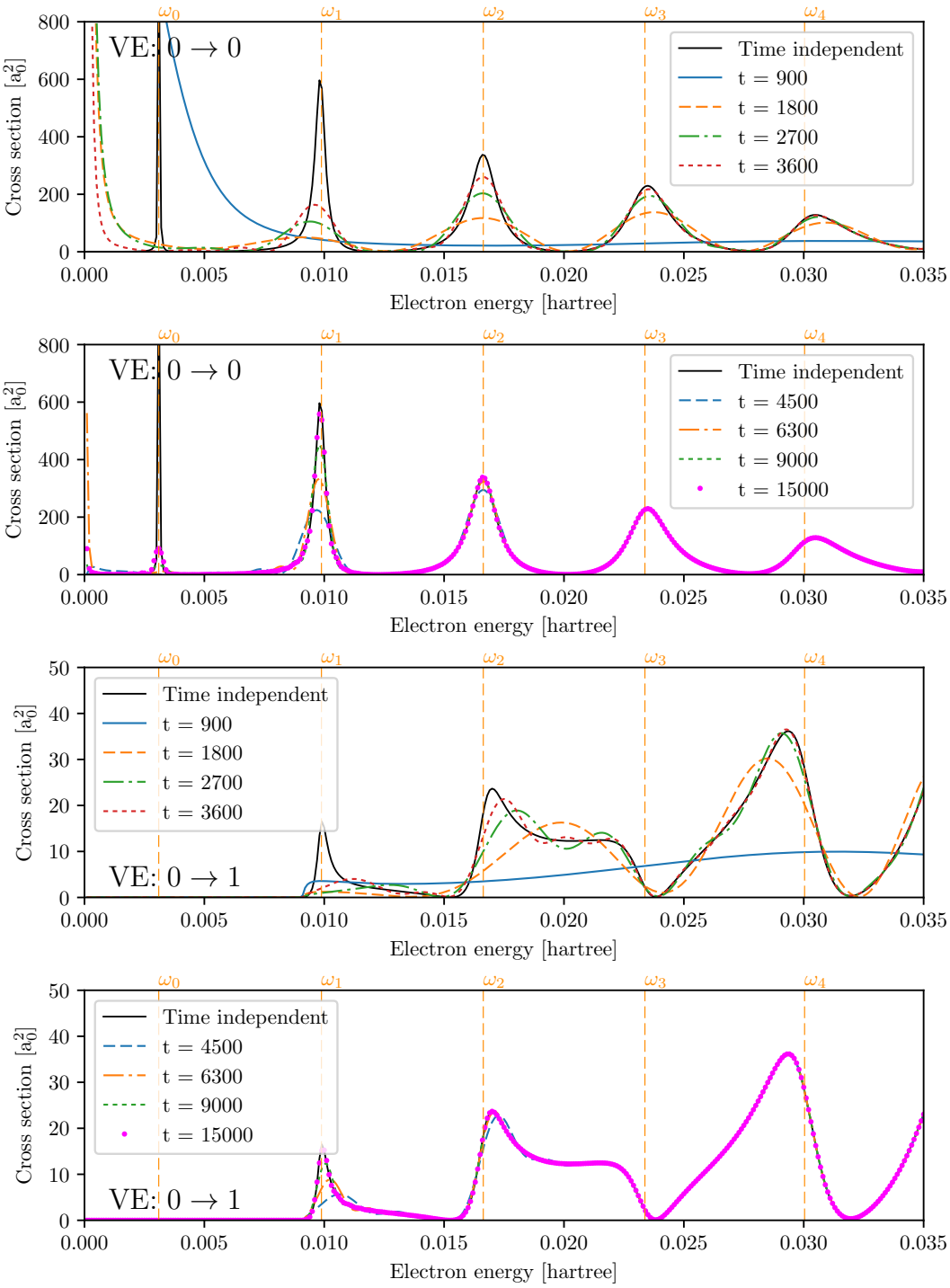

Figure 3.26: The elastic and VE transition $0 \to 1$ cross sections at significant values of the evolution time. All results are for the full 2D NO-like model. See also Chap. Attachments. for videos of the cross sections as functions of time.

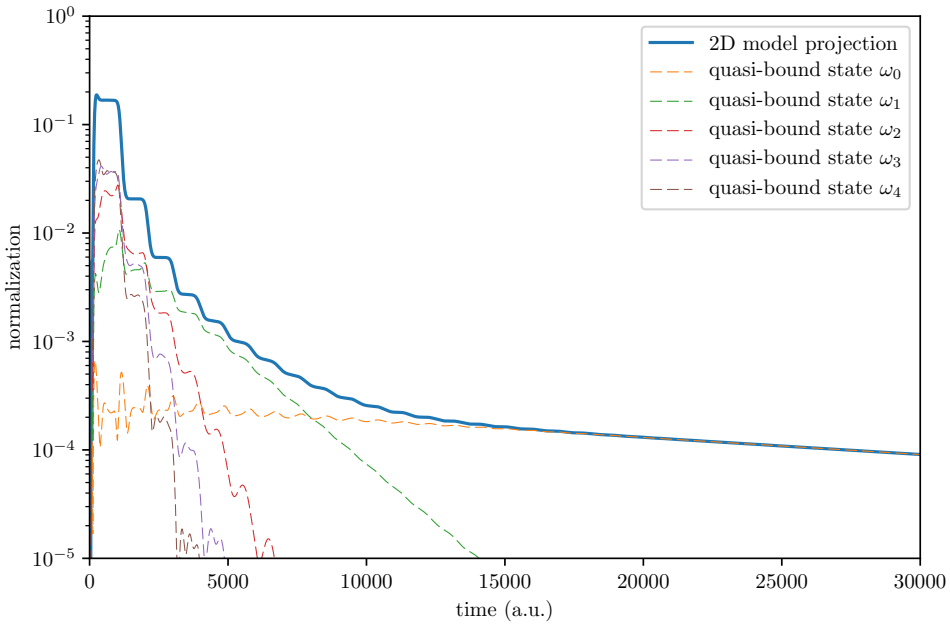

Figure 3.27: The normalization of the projection of the 2D wave function on the discrete state for the NO-like model and contributions to this normalization of the first four quasi-bound vibrational states of the molecular negative ion as functions of the evolution time.

boomerang motion. If there were no other contributions the resulting cross sections would consist of pure regular boomerang oscillations, but unlike in the N_2 case there are significant differences from the final (time-independent) cross sections, especially the peaks at lower energies in the elastic cross section are much narrower and higher and structures in the VE $0 \rightarrow 1$ cross section are very asymmetrical.

As the evolution continues and more contributions are integrated we can observe formation of these asymmetrical and narrow structures. Each narrow peak in the cross sections corresponds to a quasi-bound vibrational state of the molecular negative ion (states in the dashed blue potential in Fig. 3.9). The lower the energy of the state, the smaller its width, the larger its lifetime and the narrower the corresponding structure. In the elastic cross section the maxima of *boomerang oscillations* ($t = 1800$) are more or less at the same energies as the quasi-bound states and peaks are rather regular. On the other hand in the VE $0 \rightarrow 1$ cross section the maxima of *boomerang oscillations* are at different energies than these quasi-bound states which results in highly asymmetrical structures. Their forming in time can be observed in Fig. 3.26 from which we can estimate lifetimes of quasi-bound vibrational states. For example the first peak in the VE $0 \rightarrow 1$ cross section forms fully at $t > 10000$ and corresponds to the second vibrational state in the potential $V_{\text{res}}(R)$ of the NO-like model. The lowest lying state (the first peak in the elastic cross section) has a lifetime of more than 30000. In Fig. 3.27 we show populations of quasi-bound vibrational states of the negative molecular ion (eigenstates in the potential energy $V_{\text{res}}(R)$) in the projection of the 2D wave function on the discrete state as a function of time which we computed as $|\langle\omega_i|\Psi_d(t)\rangle|^2$. We show only results for the first four vibrational states for clarity,

populations of higher states behave similarly as the population function for ω_4 but decay even faster). We can observe in Fig. 3.27 that the higher lying vibrational states are more populated at the beginning but decay rapidly, on the other hand the low lying states survive for much longer time in accordance with the long formation time of peaks in the VE cross sections. The animation with the described process is attached as Att. 4.

4. Model of dissociative recombination of H_2^+

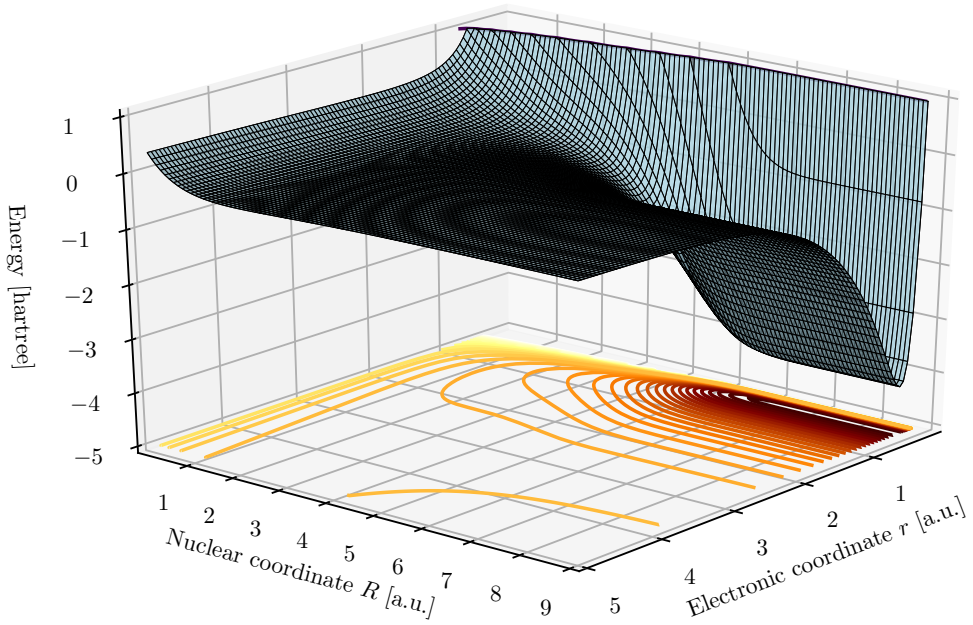

Figure 4.1: The full 2D potential energy surface of the H_2^+ model shown at short distances.

The model of the dissociative recombination for H_2^+ is significantly different in comparison to the electron-molecule collision models due to the presence of the long-range interaction given by the Coulomb term $-\frac{1}{r}$. We show the detail of the potential energy surface in Fig. 4.1. The potential forms a deep well for larger nuclear distances $R \gtrsim 5$ close to the origin of the electronic coordinate $r \sim 0.2$. From $R \sim 10$ the potential almost does not change. As a consequence to the presence of the Coulomb interaction the electron energy spectrum obtained by the fixed nuclei calculation should contain an infinite number of bound states for any value of the internuclear distance R. For large values of the internuclear distance, when the atoms are far from each other, the electron energy spectrum should correspond to the spectrum of Rydberg states in the hydrogen atom. The energy of the Rydberg state is given by the formula

$$E_n^{\mathrm{Ryd}} = \frac{1}{2(n+l+1)^2} \tag{4.1}$$

provided that n is the electron radial quantum number and l the orbital quantum number (in our case $l = 1$). We have arranged several calculated values of the asymptotic electron energy labeled with index Ry_n compared to the energies of the Rydberg states in the hydrogen atom corresponding to the quantum number

Table 4.1: Comparison of the asymptotic electron energy spectrum for recombination channels with the Rydberg states with the radial quantum number shifted by one.

n	E_{n-1}^{Ryd}	Ry_n	relative difference
0	-	-1.38492776	-
1	-0.12500000	-0.12499996	0.00%
2	-0.05555556	-0.05481037	1.34%
3	-0.03125000	-0.03083211	1.34%
4	-0.02000000	-0.01976167	1.19%
5	-0.01388889	-0.01374327	1.05%
6	-0.01020408	-0.01010943	0.93%
7	-0.00781250	-0.00774780	0.83%
8	-0.00617284	-0.00612677	0.75%
9	-0.00500000	-0.00496609	0.68%
10	-0.00413223	-0.00410657	0.62%
20	-0.00113379	-0.00113000	0.33%
30	-0.00052029	-0.00051911	0.23%
40	-0.00029744	-0.00029693	0.17%
50	-0.00019223	-0.00019189	0.18%
51	-0.00018491	-0.00018499	0.05%
52	-0.00017800	-0.00017891	0.70%
53	-0.00017147	-0.00017150	1.87%
67	-0.00010813	-0.00000825	99.77%

$n-1$ in Table 4.1. The values are very similar and therefore it is quite natural to refer to the bound electronic states within this model as to Rydberg states.

The values in Table 4.1 were computed with the discretization specified in Sec. 2.5. The first value, denoted as Ry_0 is apparently unphysical and it is clearly an artefact of the model potential. However, as stated by Hamilton [2003], the energy of the state is so low, that it does not influence significantly the dynamics in higher Rydberg states we are interested in. The model potential is chosen in such a way to reproduce very closely the energy of first excited state $2p$ of H and also the higher Ryberg states, which can be observed in Tab. 4.1 up to $n \sim 40$ for which the relative difference is smaller than for $n = 2$. The value Ry_1 is very close to the first exited state of the hydrogen atom. The next few values show a relative difference around 1% and with increasing quantum number n the difference decreases, up to a certain point, where it starts to increase rapidly. For states with $n > 50$ the energies are more and more incorrect due to the finite discretization and there are actually only 67 bound states instead of infinity. Moreover, for $n \gtrsim 30$ a non-negligible imaginary part arises in the energies Ry_n, because of the exterior complex scaling, which results in absorption of the wave function and therefore in inaccuracies of the computed cross sections. We expect the size of the affected energy region to be roughly $\Delta_E^{\mathrm{err}} \approx 0.001$, which leaves us with around twenty well described Rydberg states. The energy potential curves of these states obtained via fixed-nuclei calculations are shown in Fig. 4.2

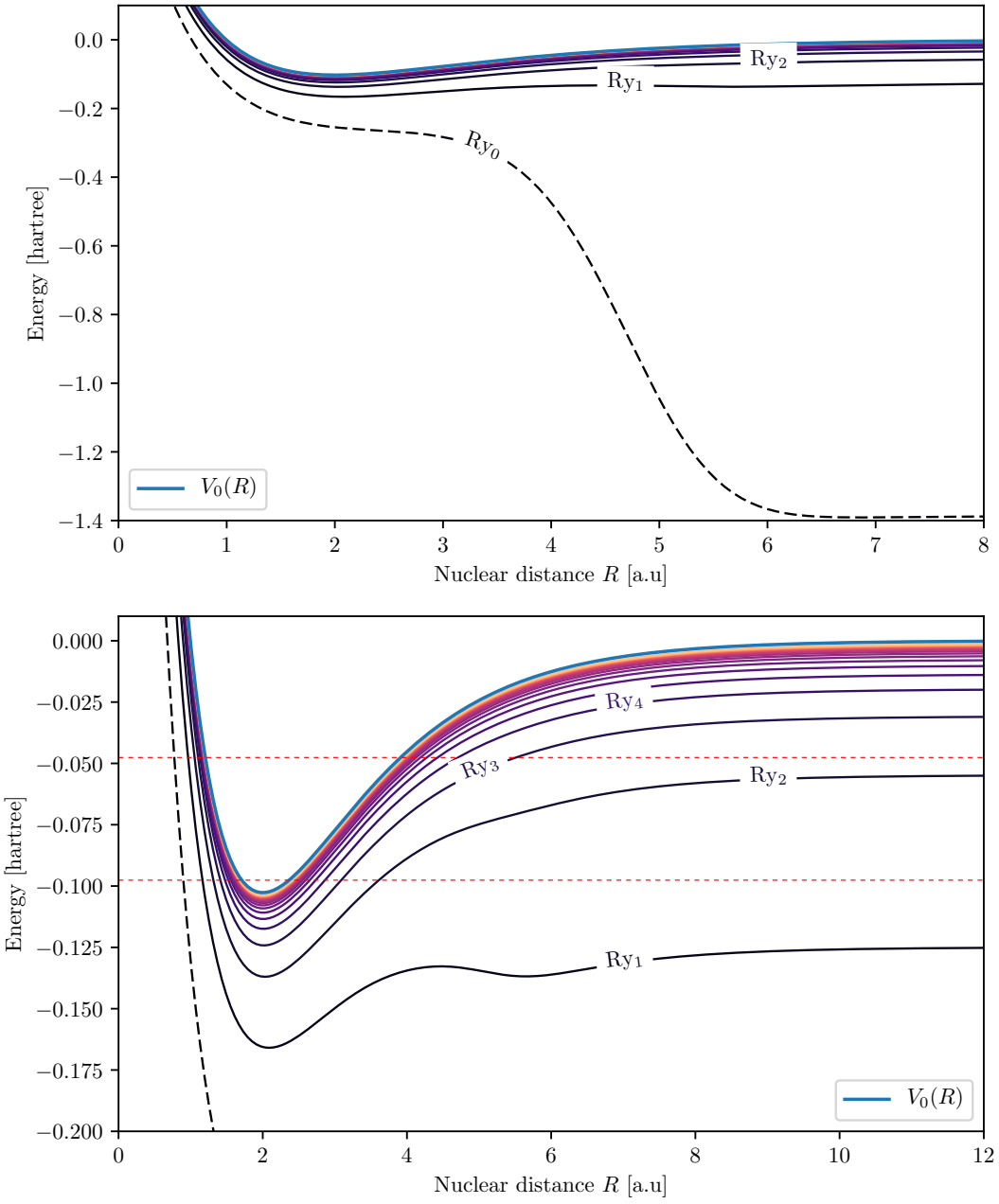

Figure 4.2: The electron energy curves $E_{\mathrm{Ry}_n}(R)$ obtained via fixed-nuclei calculations, labeled with Ry_n for the first few states. The top panel shows the overview of the potential curves. The dashed curve is the unphysical ground state Ry_0. The bottom panel shows the same curves in more detailed energy region. Note that the first Rydberg state curve Ry_1 has lower asymptotic energy than the minimum of $V_0(R)$ suggesting the corresponding recombination channel DR_1 will be opened for any value of kinetic energy of the incoming electron. The investigated energy range is marked as space between the two red dotted lines.

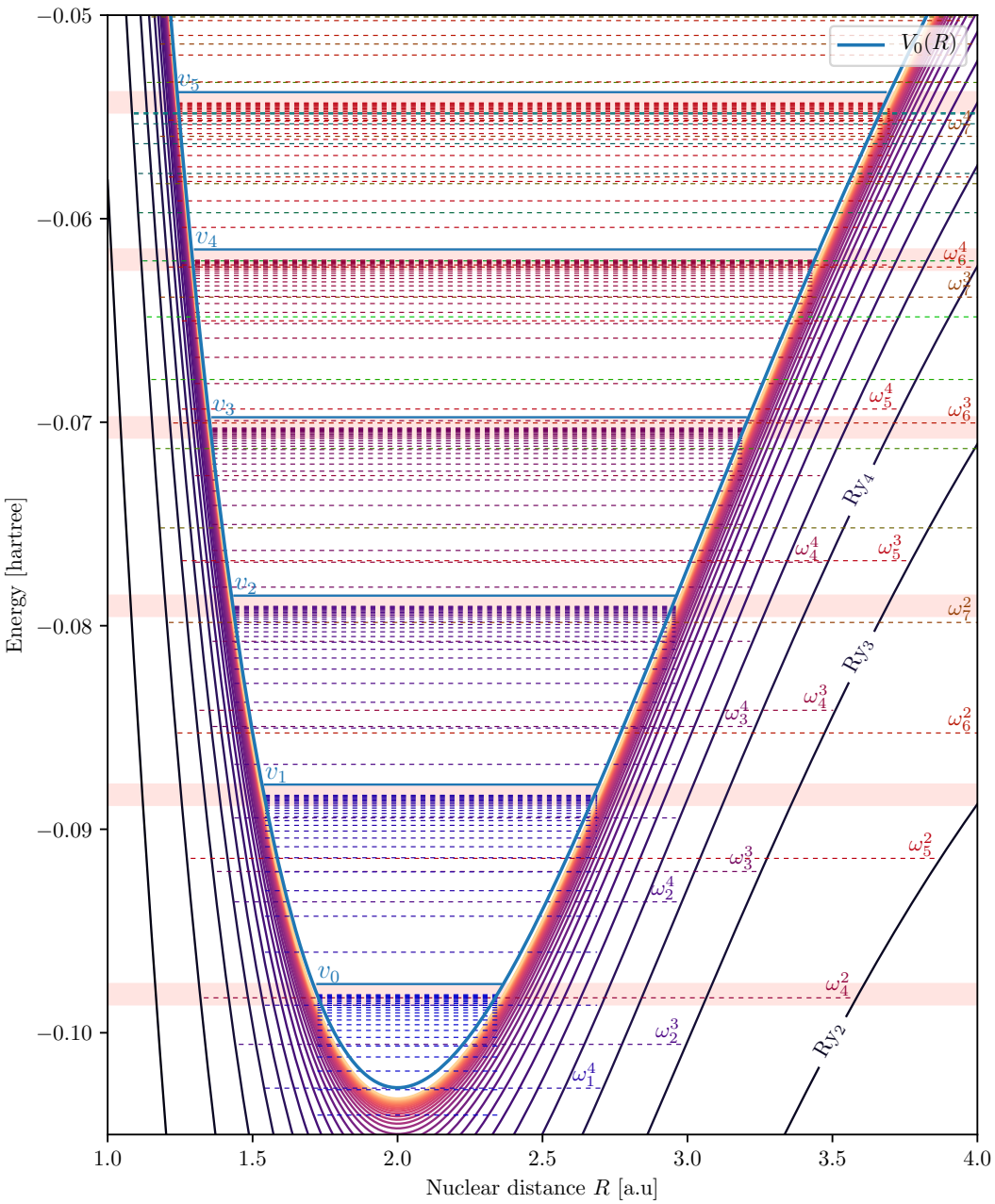

Figure 4.3: A detailed picture of the electron energy curves $E_{\mathrm{Ry}_n}(R)$ for short nuclear distances and within investigated energy range. The solid blue curve is the cation potential energy $V_0(R)$, the horizontal solid blue lines show the positions of the cation vibrational energy levels labeled with v_i. The dashed horizontal lines are the vibrational levels in the electron energy potential E_{Ry_j} labeled with ω_i^j, where i is the vibrational level and j stands for the corresponding Rydberg state number. The pink shaded areas depict regions Δ_E^{err} (see text) where we expect inaccurate results due to the finite discretization.

and in detail with marked vibrational levels in Fig. 4.3. Note that in this model of dissociative recombination there is no crossing of the fixed-nuclei potential energy curves with the cation vibrational potential $V_0(R)$ and thus no simple approximation such as LCP can be applied.

4.1 Wave function evolution

We have set the incoming wave packet to be a product of the cation vibrational ground state χ_{v_0} and the Gaussian wave packet located at $r_0 = 800$ with $p_0 = 0.25$ and $\sigma = 8.0$. The wave packet is located quite far from the interaction region since we intend to keep the initial overlap between the incident wave packet and the lower electronic Rydberg states as little as possible. The electronic coordinate discretization had to be extended anyway to properly describe as many Rydberg states as possible and therefore there is no significant computational resource cost. The mean impulse p_0 corresponds roughly to kinetic energy $E_0^{\mathrm{kin}} \simeq 0.026$ which is located near the middle of the investigated energy range $E^{\mathrm{kin}} \in (0, 0.05)$. Note that the actual kinetic energy differs from the value $E_0 = \frac{p_0^2}{2} \doteq 0.031$ since the actual energy eigenstate basis is not given by planar waves but with Coulomb functions and therefore the actual energy distribution also depends on the wave packet position r_0, however this does not have any effect on the dynamics of the recombination process.

The parametrization of the evolution operator was set as described in Sec. 2.5. The general idea behind this setting is that the correlation functions will be much smoother than in the models of electron-molecule collisions since the investigated range of energies is four times smaller. Therefore a more rough discretization in time may be applied without loss of accuracy.

We show a few snapshots of the wave function evolution in Fig. 4.4 and Fig. 4.5. At the beginning of the evolution the incoming wave packet moves in the Coulomb potential towards short electronic distances. Naturally the wave packet becomes very wide since the higher energies reach the interaction zone earlier than the lower energies. As the wave packet hits the interaction zone a dominant part of the wave packet is reflected back to the channel of elastic scattering. Unlike the electron-molecule collision models the dissociative recombination model has no potential barrier for the incoming electron to penetrate and therefore there is no process of tunneling and trapping behind such a barrier. However not the whole wave packet is reflected back. A smaller part of the wave packet starts to move towards larger nuclear distances due to the interaction potential $V_{\mathrm{int}}(R, r)$ coupling the two coordinates. Part of the wave packet then escapes to the vibrational excitation channels and a very small part of the remaining wave packet is transmitted directly to the recombination channels forming the scattering background in time $t \sim 2000 - 5000$, dependent on the incoming electron energy. Because of the redistribution of the kinetic energy into both coordinates the wave packet is mostly captured in a temporary state given by a superposition of Rydberg states in the electronic coordinate and vibrational states in the nuclear coordinate. The wave packet cannot easily escape to neither the vibrational excitation channels nor the dissociative recombination channels, since the kinetic energy distributed to their respective coordinates is too low. At this time the

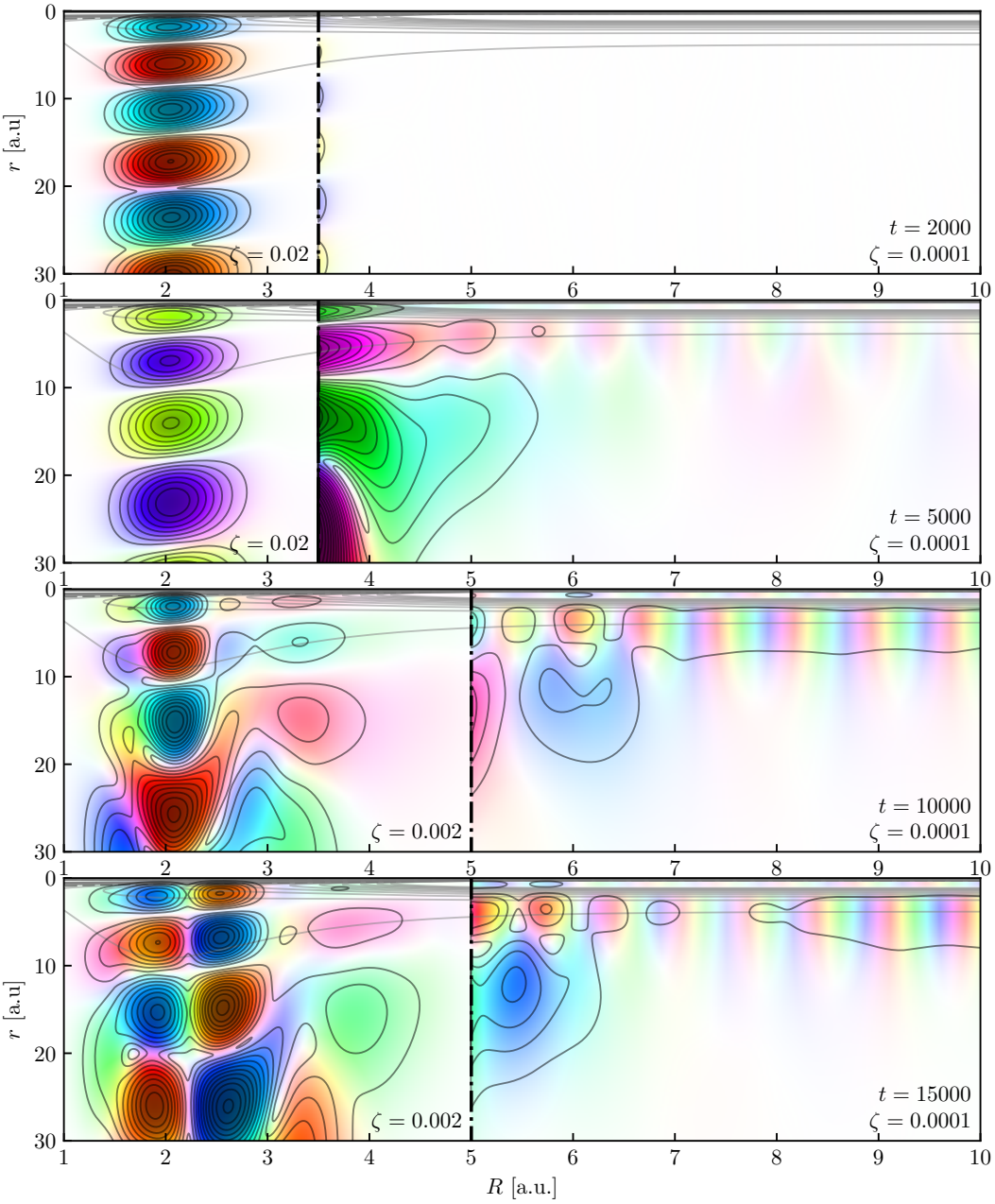

Figure 4.4: Snapshots of the full two-dimensional wave function $\Psi(R, r; t)$ at few moments of the evolution, in the HSV image model. The thick black dash-dotted line marks splitting of the image for HSV magnification via parameter ζ. The top panel shows the initial reflection, where outgoing waves to DR channels are negligible. The second panel from top shows the wave function penetrating directly to DR channels, forming the background shape of the cross sections. The third panel from top shows the first significant vibrational motion in the nuclear coordinate. The bottom panel shows the wave function no longer dominated by cation vibrational ground state and a small wave packet leaving to DR channels.

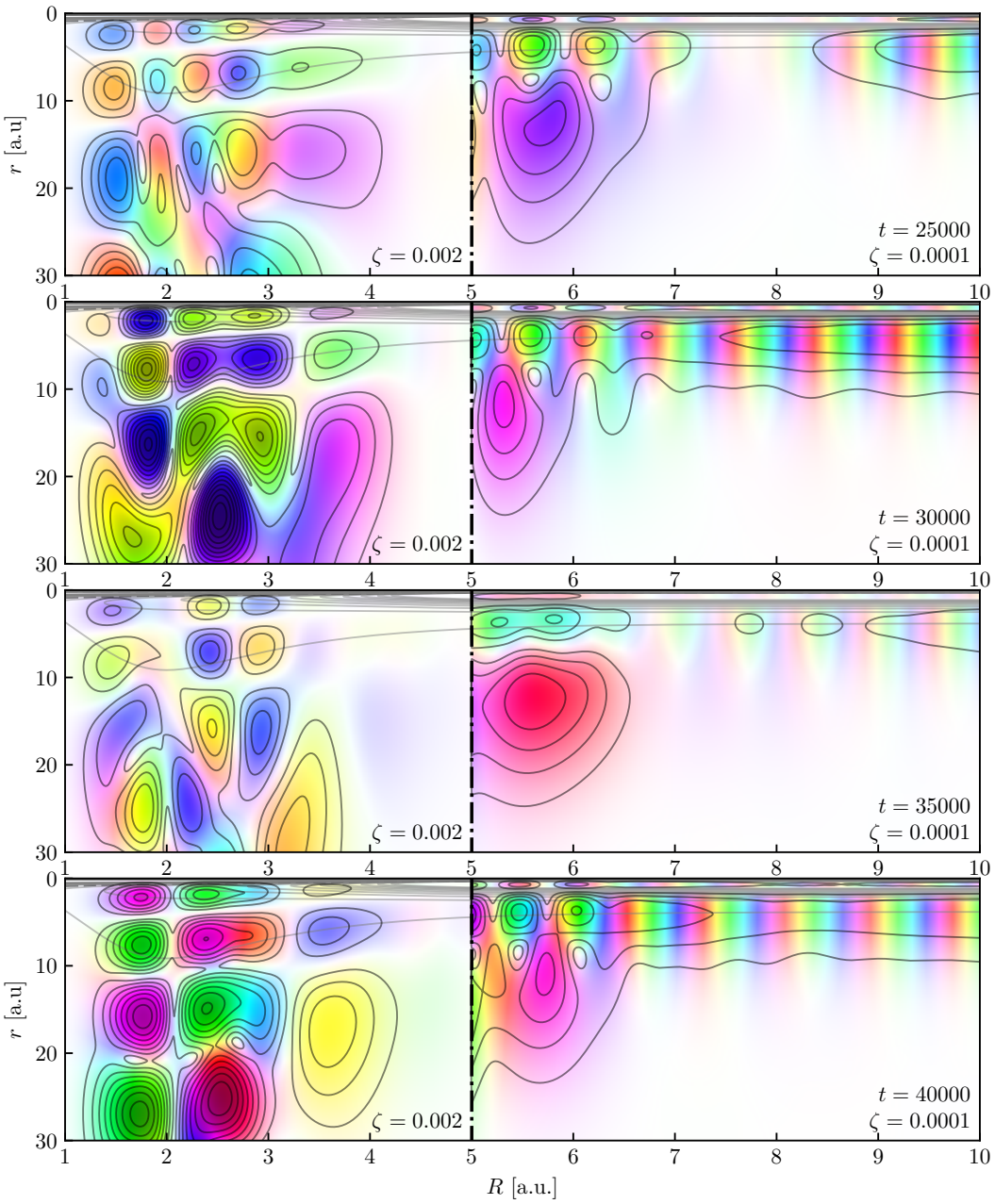

Figure 4.5: The second part of the full two-dimensional wave function $\Psi(R, r; t)$ snapshots in the HSV image model. The top snapshot shows the wave packet leaving to the recombination channels, while the rest of the wave function is located further in the electronic coordinate leaving only a smaller part in the interaction region. The second panel from top shows the wave function located at shorter electronic distances while penetrating to the recombination channels. The third and fourth panels show the repetition of this motion.

state of the system looks like an electronically and vibrationally excited state of a neutral hydrogen molecule H_2^*.

As the time passes the wave function reaches larger nuclear distances meaning the higher molecular vibrational states are excited. Consequently the wave packet exhibits more pronounced oscillations in the nuclear coordinate, while the motion in the electronic coordinate becomes more compact. Once the wave function reaches the region $R \gtrsim 10.0$ a part of the wave function escapes to the recombination channels. This *double-oscillation* process will repeat over and over for a very long time. The shape of oscillations varies in time since the motion period differs in the electronic and the nuclear coordinate, dependent on which quasi-bound states ω_i^j are currently occupied.

Note that the outgoing wave packets to the recombination channels are dominated by the electronic state Ry_1. The presence of the lower channel Ry_0 is not visible and the presence of the higher state Ry_2 can be only estimated from the slight oscillations in the electronic coordinate in the region beyond $R \sim 8$. Higher states than Ry_2 are not visible, since they are not accessible in the given energy range. The shape of the outgoing waves is however strongly dependent on the setting of the initial wave packet and therefore we do not expect the shape itself to bear much of the physical relevance.

4.2 Cross sections

To calculate the cross sections using the Tannor&Weeks method, we have placed the test functions into three accessible recombination channels, even though the lowest channel is unphysical. It is convenient to calculate the cross sections of the unphysical state to validate the proposition that only negligible flux goes to this channel and the other results are not disturbed by its presence. The position $R_0 = 12.0$ and wave packet thickness $\sigma = 0.4$ were set the same for all test functions. The mean impulse was set to $q_0 = 60.0$ for the DR_0 channel and $q_0 = 12.0$ for the DR_1 and DR_2 channels. We show the absolute value of correlation functions in logarithmic scale for the first 10^7 atomic units of time in Fig. 4.6. The correlation functions oscillate quite wildly and chaotically. The decrement of the correlation functions amplitudes is very slow and therefore the evolution of the wave function had to be computed up to $t_c = 8 \times 10^7$ atomic units of time to get the converged cross sections. With the evolution time step set to $\Delta t = 10$ it results in 8×10^6 iterations. An important observation which can be made from Fig. 4.6 is that the correlation amplitude of the unphysical channel DR_0 is roughly six orders of magnitude below the first physical channel DR_1, validating the statement that the unphysical channel cannot significantly influence the model dynamics in the channels of interest.

We present the cross sections computed at the cutoff time t_c by the time-dependent method in comparison to the time-independent reference results in Fig. 4.7 and Fig. 4.8. Unlike the results of the electron-molecule collision models we present the cross sections in logarithmic scale since the values often differ by many orders of magnitude and in the linear scale the comparison would be quite difficult.

Note that for the very low energies the cross sections of the DR_0 and DR_1 channels obtained by the time-dependent approach are still oscillating and in some

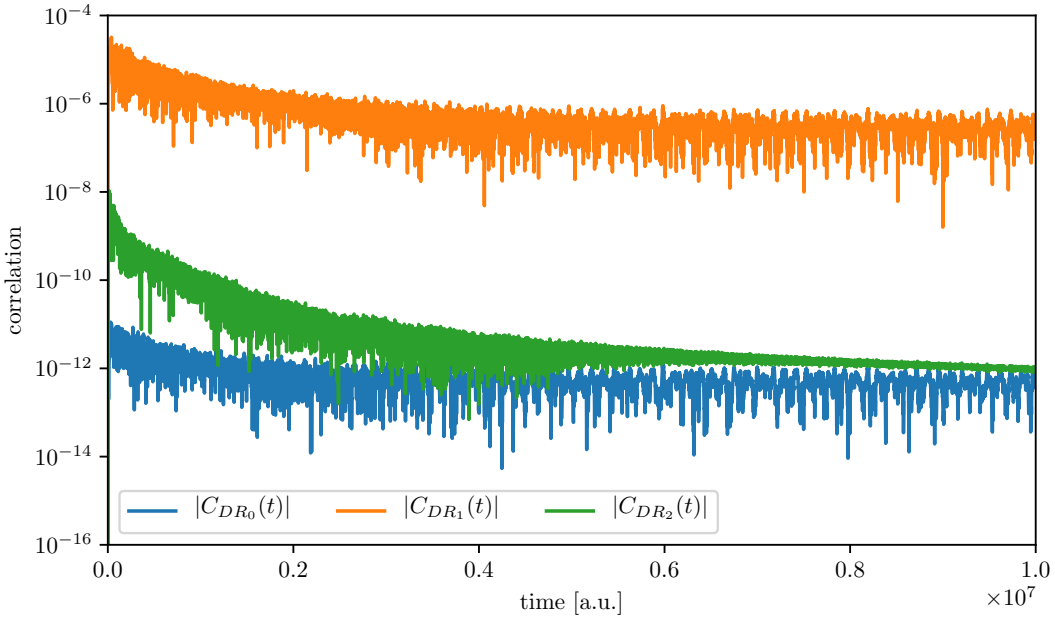

Figure 4.6: The absolute value of the correlation function for the three investigated dissociative recombination channels. All functions show heavy oscillations from early evolution time. The frequency of the oscillations is reducing with time as larger parts of the wave function leave the system.

places the values are still not converged. The DR_0 channel cross section is mostly of the same or a very similar shape as the DR_1 channel however it is roughly four orders of magnitude smaller and even in the areas where the shape changes wildly the DR_0 cross sections does not get closer than two orders of magnitude to the DR_1 channel cross sections. For energies grater than 0.037 the cross sections of DR_0 obtained by time-dependent calculation becomes different from the time-independent reference. This difference originates from a poor choice of the test function parametrization and it could be improved by tweaking the parameters. However since we are not interested in this channel we did not attempt to improve it.

The shapes of the cross sections show various interesting features, sharp local maxima and minima, wider plateaus without any structures, double or even triple peaks or cusps. In many cases the position of the feature coincides very well with the position of some quasi-bound state energy level ω_i^j and therefore we can interpret such a feature as a resonance corresponding to this level, however not all features seem to directly correspond to some resonances and more complex analysis is required for their explanation.

Some of the features which do correspond to resonances are slightly shifted, e.g. peaks near $E \sim 0.006$, and for some features the shifting is so large that it is nearly impossible to identify them with any nearby quasi-bound state solely by its position, e.g. features near ω_4^4 and ω_5^3 at $E \sim 0.021$. However the displacement of these features may be expected since the energies of the quasi-bound states are calculated in one-dimensional potential curves obtained from the fixed-nuclei calculations. The actual resonance energies may be quite different, especially in regions where several vibrational levels of different electronic states almost

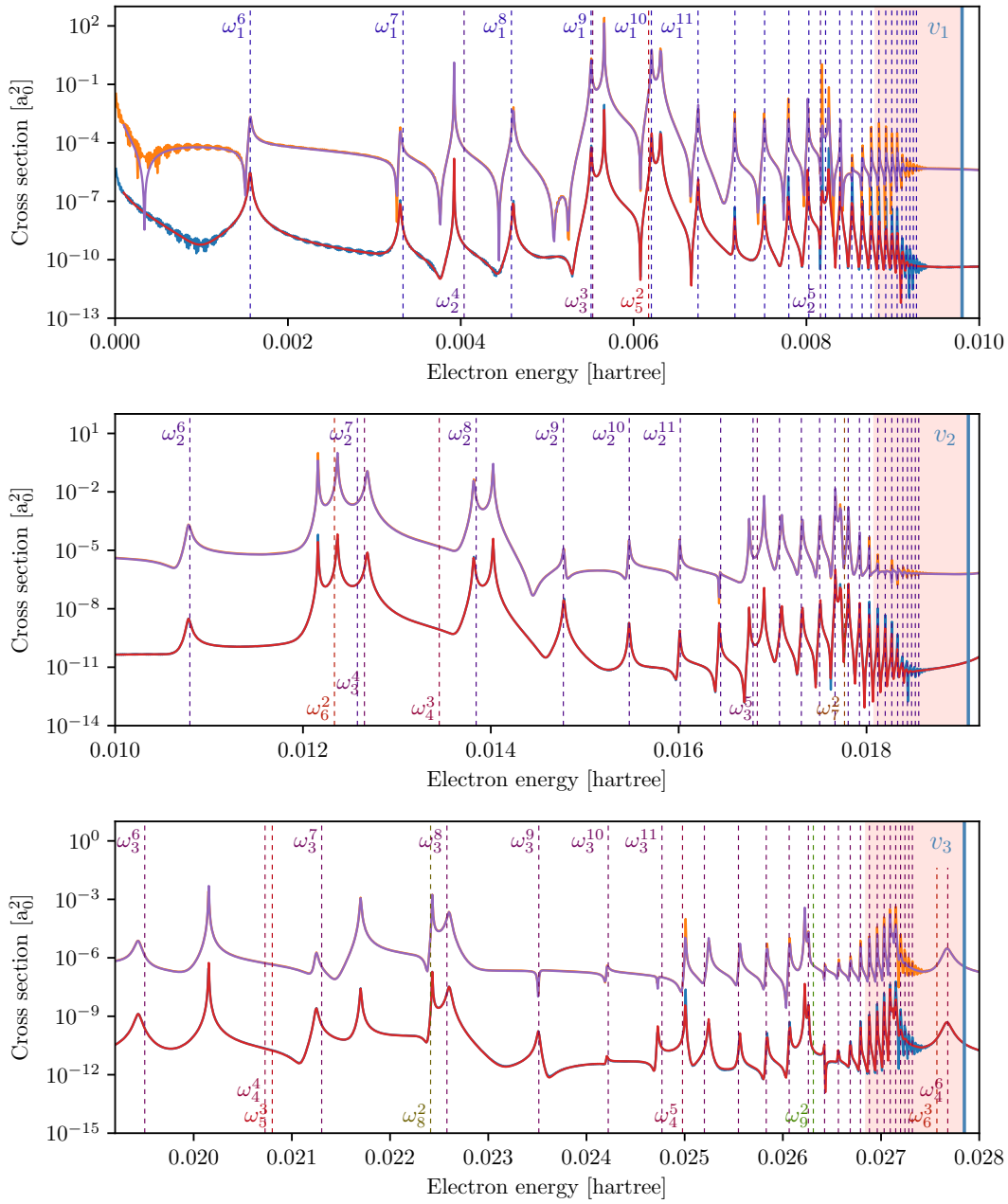

Figure 4.7: Comparison of the DR cross sections for the H_2^+-like model computed by the time-dependent (blue for DR_0, orange for DR_1) and the time-independent (red for DR_0, purple for DR_1) approach for the first three parts of the investigated energy range. The curves from the time-dependent calculations show good accordance to ones from the time-independent calculations except at very small energies where the time-dependent results are not fully converged (left part of the top panel). The dashed vertical lines mark the positions of the vibrational levels ω_i^j (see Fig. 4.3 for details).

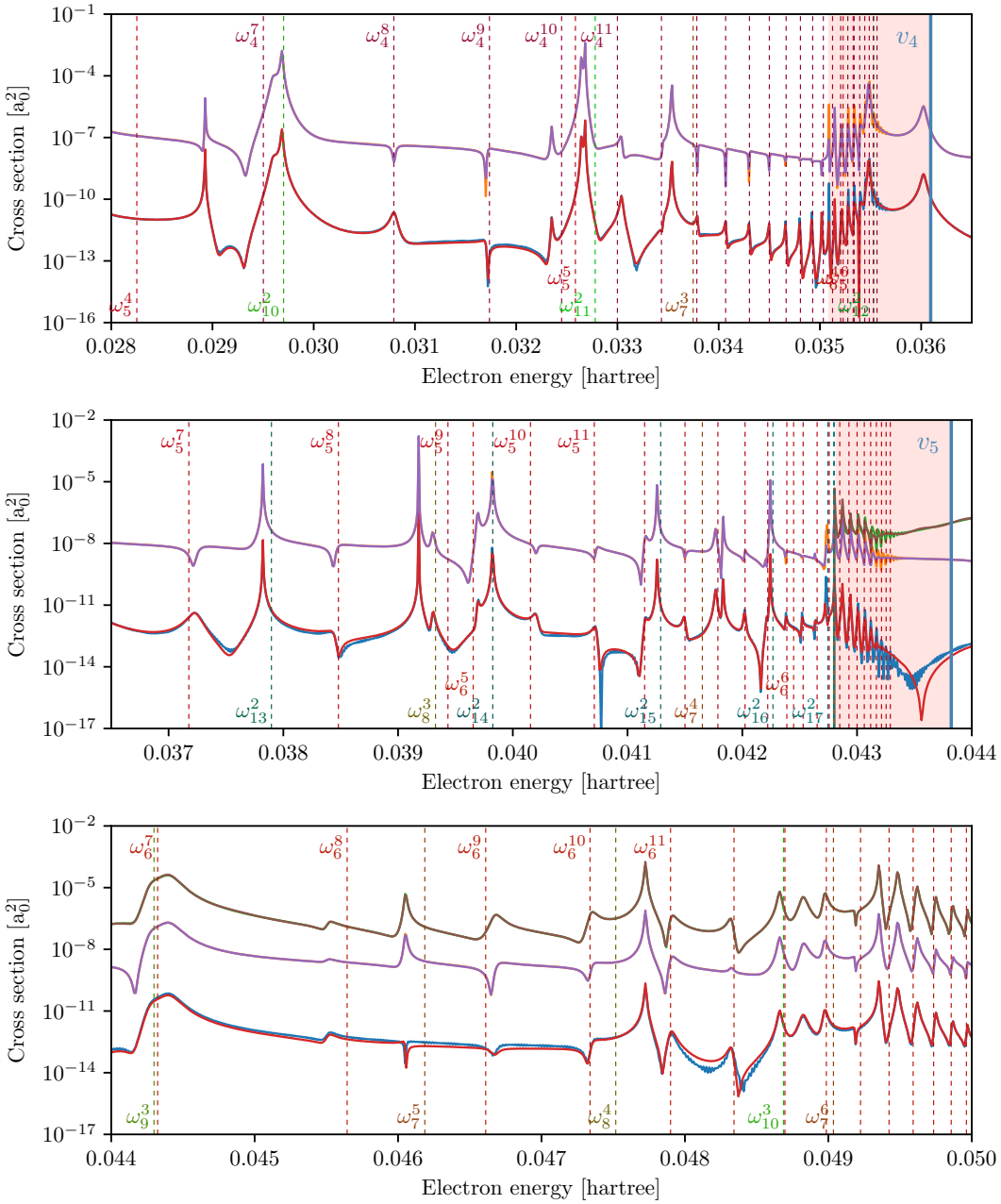

Figure 4.8: The second part of the comparison of the DR cross sections for the H_2^+-like model computed by the time-dependent (blue for DR_0, orange for DR_1, green for DR_2) and the time-independent (red for DR_0, purple for DR_1, brown for DR_2) approach for the last three parts of the investigated energy range. The time-dependent results show a good accordance to the time-independent ones except for the DR_0 channel at higher energies (middle and bottom panels) where the cross section is very small. The dashed vertical lines mark the positions of the vibrational levels ω_i^j (see Fig. 4.3 for details).

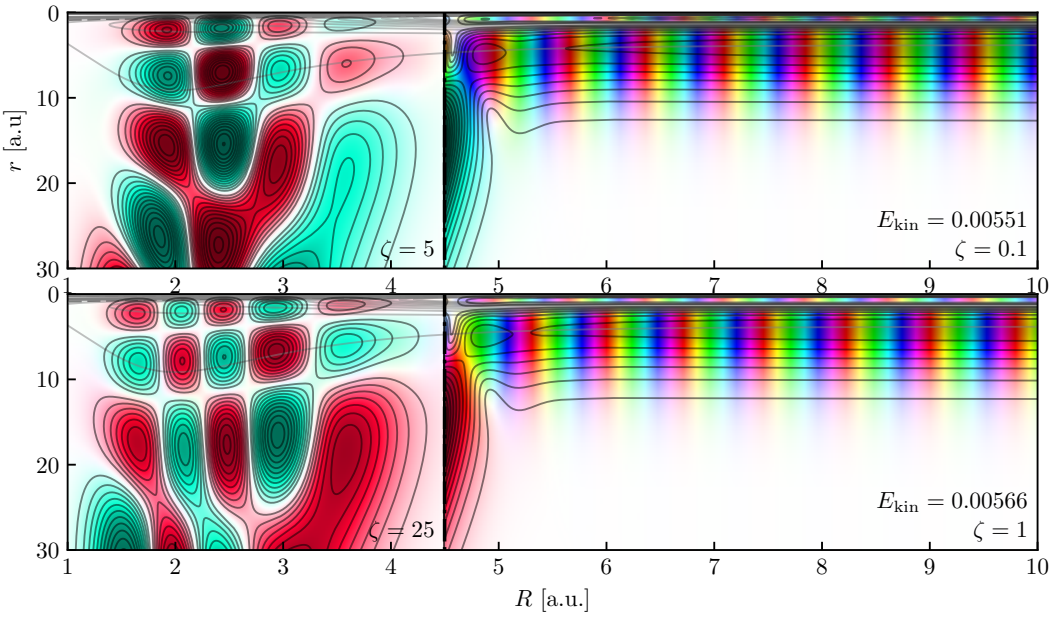

Figure 4.9: The wave function $\Psi^+(R, r; E)$ shown at short distances for two energies corresponding to the sharp peaks in the DR cross section.

coincide.

As one approaches the vibrational excitation thresholds v_i the density of the features increases significantly. However at some point the cusps become suppressed and vanish. These regions are marked by the red shading and correspond to the regions Δ_E^{err} in Fig. 4.3, where the results are inaccurate. It is obvious that the density of the features should increase up to the threshold, however due to the lack of the electronic bound states in this region, because of the finite grid in our calculations, these features are entirely missing.

4.3 Interpretation of the results

Even though the model dynamics is quite complicated, some of the interesting features in the DR cross sections may be easily explained with use of the time-independent calculation results. The structures which are rather displaced from the positions of the quasi-bound state energy levels ω_i^j may be sometimes associated to these states simply by looking at the full two-dimensional physical wave function $\Psi^+(R, r; E)$ at the energy E of the investigated feature. As an example we investigate the double resonance near the energy levels ω_1^9 and ω_3^3. We show the full two-dimensional wave functions for energies of the peaks near these levels in Fig. 4.9. Apparently the wave function $\Psi^+(R, r; E = 0.00551)$ oscillates slightly less in the nuclear coordinate and slightly more in the electronic coordinate than the wave function $\Psi^+(R, r; E = 0.00566)$. This leads to proposition that the state ω_1^9 should be associated to the peak at $E = 0.00551$ and the state ω_3^3 to the peak at $E = 0.00566$. To validate this observation we simply perform a scalar product of the full wave functions and the wave functions corresponding to the considered levels. The comparison of the absolute values of the scalar products is shown in

Table 4.2: Comparison of the absolute values of the scalar product of the full two-dimensional wave functions $\Psi^+(R, r; E)$ at given energies with the quasi-bound states ω_i^j.

state	$\lvert\Psi^+(R, r; 0.00551)\rangle$	$\lvert\Psi^+(R, r; 0.00566)\rangle$
$\langle\omega_1^9\rvert$	207.77	63.82
$\langle\omega_3^3\rvert$	43.31	232.92

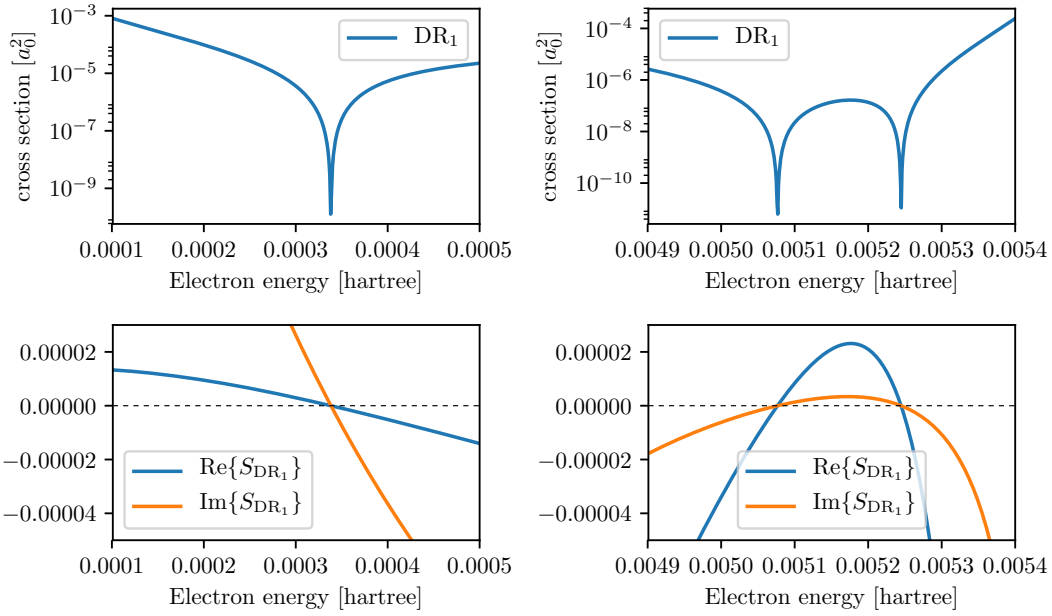

Figure 4.10: Comparison of the cross sections and S-matrix elements at energy regions near the minima of the cross sections. Both the S-matrix elements and cross sections were obtained from time-independent calculations.

Table 4.2. We conclude that the larger absolute value of the scalar product can serve to identify the resonance with its corresponding quasi-bound state.

Other interesting features of the cross sections are the sharp local minima in the regions where no quasi-bound state energy levels are present, e.g. the very first minimum in the DR$_1$ channel cross sections at $E_{\text{kin}} \sim 0.00034$ or the two minima between the ω_1^8 and ω_1^9 energy levels in the same channel (see the top panel of Fig. 4.7). In both cases the nearby quasi-bound state energy levels are quite far from the investigated features and these levels were already associated with other features.

We do assume that these local minima are of different nature than e.g. the minimum in the DR$_1$ channel near the quasi-bound state energy level ω_3^9 in the bottom panel of Fig. 4.7. We show the detail of the DR$_1$ cross section for two small energy regions near the investigated features in Fig. 4.10 along with the detail of the S-matrix energy dependence. The S matrix is smooth in these regions and the minima result from simple crossing of the zero for both the real and the imaginary part of the S matrix. For comparison we show the DR$_1$ cross section

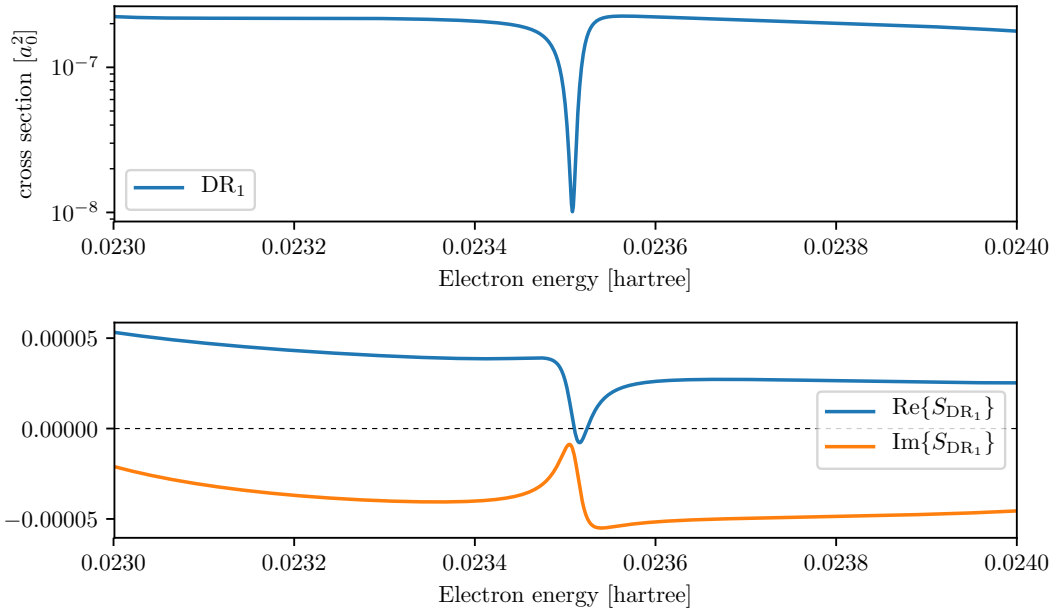

Figure 4.11: Detail of the DR_1 channel cross sections near the quasi-bound state energy level ω_3^9 along with the elements of the S matrix.

along with the S-matrix elements near the local minimum associated with the quasi-bound state ω_3^9 in Fig. 4.11. Note that this time not only the cross section but also the S-matrix elements change wildly close to the position of the local minimum. This behavior is to be expected if the feature is associated with a corresponding quasi-bound state and thus interpreted as a resonance.

We conclude that the local minima which cannot be interpreted as resonances are of a similar nature as the *Ramsauer-Townsend* minima observed in the collisions of the electrons with atoms (see e.g. Townsend and Bailey [1922]).

As previously discussed the evolution of the wave function is quite complicated and this complexity results in the cross sections with many sharp features. In contrast with the electron-molecule collision models no straightforward interpretation is possible if we observe the evolution of the wave packet in the setting from which the complete cross sections may be determined. To obtain the results which provide a more detailed insight into the evolution of the wave function, we confine the incident wave packet to much smaller range of the incoming electron energies. We have tested two more parametrizations of the incident Gaussian wave packet in the initial state (1.41). We show the sets of wave packet parameters (II and III)

Table 4.3: Comparison of different parametrizations of the incident wave packet in the electronic coordinate.

	r_0	p_0	σ
I	800	-0.25	8.0
II	600	-0.11	25.0
III	600	-0.1	50.0

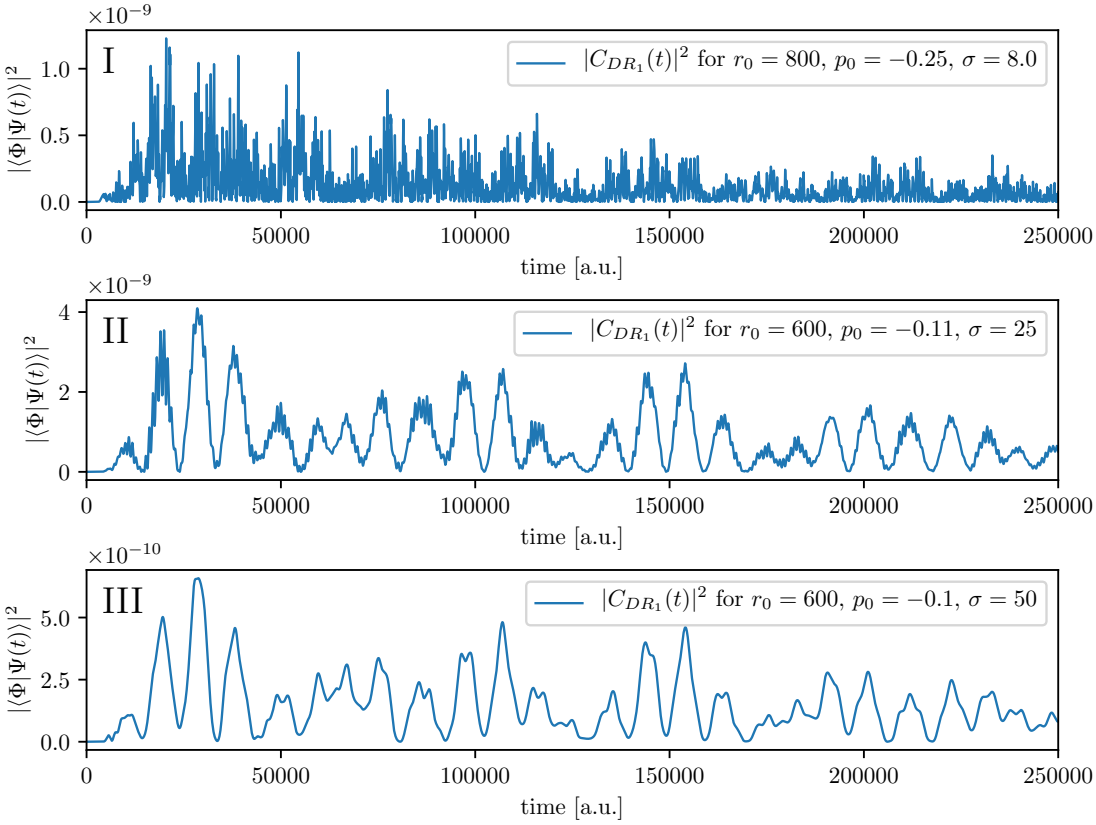

Figure 4.12: Comparison of the correlation functions for different parametrizations of the incident wave packet.

compared to the original values (I) in Table 4.3. The parametrization II covers the region of the incoming electron energy $E_{\text{kin}} \in (0, 0.01)$, the parametrization III covers only a part of this region $E_{\text{kin}} \in (0, 0.007)$. Note that we do expect different shapes of the evolved wave function and correlation functions, however we do not expect significant differences in the final cross sections. The only possible difference may occur in the partial time-integration of the correlation functions due to the change of the initial position of the wave packet. This should however affect only the positioning of the significant contributions in time, not their shape. We show the comparison of the correlation functions during the early part of the evolution for the three different initial state parametrizations in Fig. 4.12. From this comparison it is obvious that the original setting is not suitable for the interpretation due to the vast amount of overlapping processes. We choose the parametrization III to investigate the motion of the wave function, since the correlation function is smooth enough.

To study the motion we have determined the population functions for the first four vibrationally exited quasi-bound states in several electronic Rydberg potentials. The population functions $|\langle\omega_i^j|\Psi(t)\rangle|^2$ compared to the shape of the correlation function in the recombination channel DR_1 are shown in Fig. 4.13. Apparently the initial scattering populates mostly the lowest possible vibration. The vibrational levels are however coupled together and the higher vibrations become quickly populated as well. The system then oscillates between these coupled states.

From the population functions we can make several other observations. Only

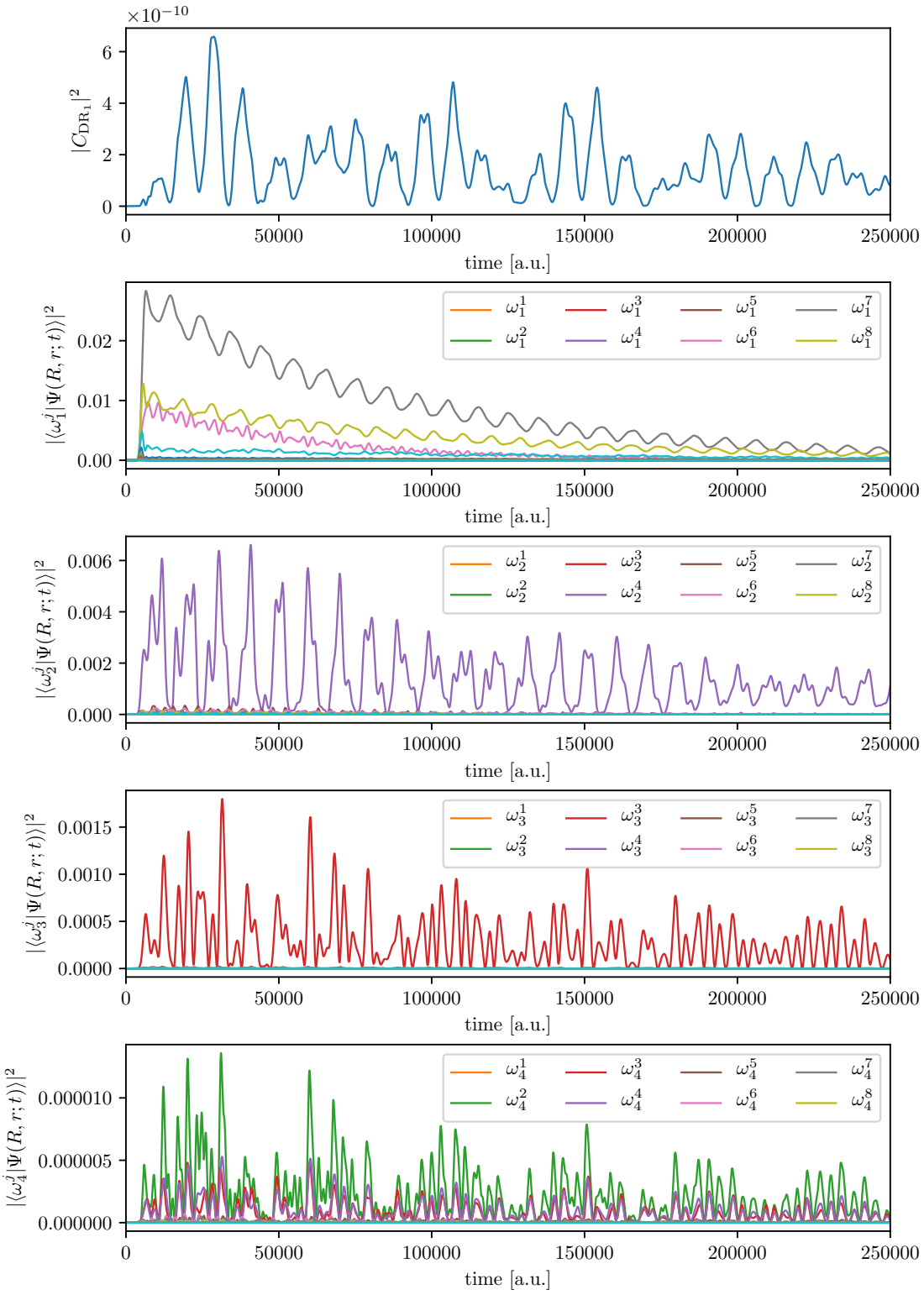

Figure 4.13: Population functions of the quasi-bound states ω_i^j for first four vibrations and several Rydberg states compared to the shape of the DR_1 channel correlation function.

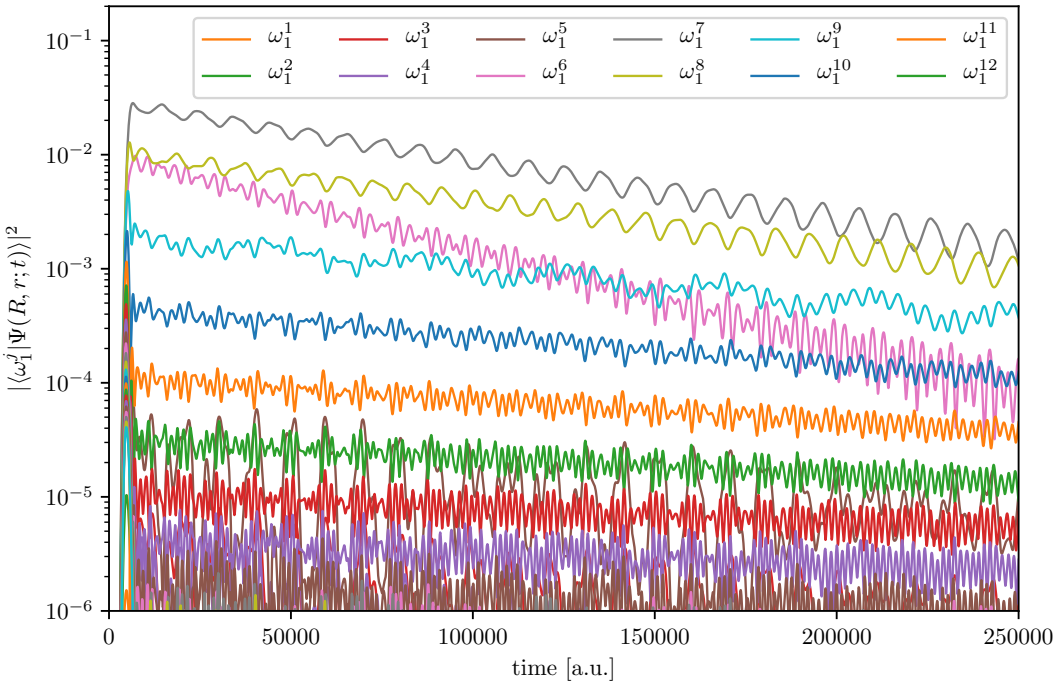

Figure 4.14: Detail of population functions of the quasi-bound states ω_1^j for the first vibration in several Rydberg states in logarithmic scale.

the states with first vibrationally excited level are significantly populated from the direct interaction with the incoming wave packet and during the rest of the evolution these populations are exponentially decaying as the wave function escapes to the vibrational excitation channels. For convenience we show the ω_1^j populations in the logarithmic scale in Fig. 4.14. The exponential decay is however modulated by oscillations which are in counter phase to the oscillations in population functions of higher vibrationally excited states. We conclude that these states are populated mainly by the coupling to the lower vibrationally excited states and the oscillations result from presence of the reverse process repopulating the lower vibrationally excited states. We also believe that the system is more likely to dissociate from the higher vibrationally excited states. Together these observations partially support the interpretation of the motion as so called *ladder mechanism* of the dissociative recombination suggested by C.H. Greene [personal communication, 2017]. Within this mechanism the electron subsequently excites the higher molecular vibrations while descending to lower Rydberg states up to the point where the system can dissociate. However in our observation also the reverse process is visible and the motion is mostly dominated by repeated oscillations between the quasi-bound states. This mechanism of the dissociative recombination could be described as *multiply indirect*. The evolution of the wave function along with few population levels in time are arranged in animation, provided as Att. 6.

To give the complete picture of the features provided by the time-dependent approach we also present the cross sections computed up to some significant times of the evolution, which are shown in Fig. 4.15. For this purpose we have chosen the initial state parametrization II since it covers well the whole region

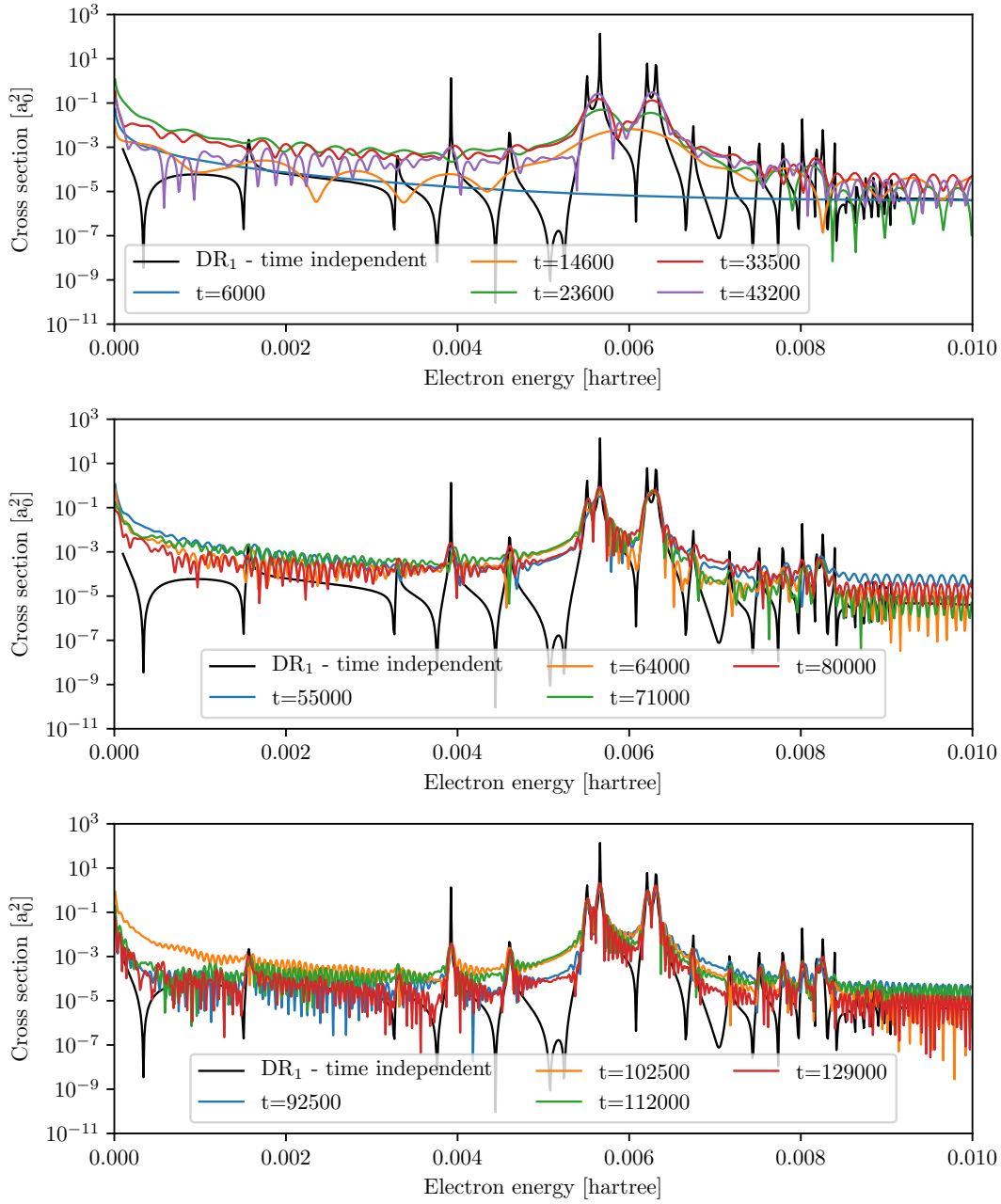

Figure 4.15: Comparison of the DR_1 channel cross sections calculated by the correlation function for several chosen times of the evolution. The top panel shows the shapes for early moments, with recombination background evaluated at time $t = 6000$ (blue line) and few first contributions from the initial oscillations, forming the base shape of the structures. The second panel shows further contributions, where the splitting of the overlapping resonances is visible. The third panel shows the contributions from further evolution, revealing that even after more than 120,000 units of time the structures are still very different from the time-independent reference.

of $E_{\mathrm{kin}} \in (0, 0.01)$. The times of the evaluation were chosen to correspond to the local minima of the correlation function amplitude for the DR_1 channel. As in the electron-molecule collision models the first contribution creates a smooth background, provided by the direct mechanism of the dissociative recombination. In the following contributions series of mostly smooth peaks appear, forming the basic shape of the cross sections. The further contributions modulate this shape to form the more narrow peaks. Even after more than hundred thousand atomic units of time the shapes of the cross sections are far from converged. It takes several millions of time units to provide the shape which resembles the time-independent calculation cross section.

Conclusion

We have investigated the two-dimensional model of the collisions of electrons with diatomic molecules and the two-dimensional model of the dissociative recombination of the electron with the hydrogen cation H_2^+. We have solved the model dynamics numerically in both time-independent and time-dependent approach. The application of the time-dependent approach to the model dynamics of the dissociative recombination model revealed the stability and accuracy of the generalized Crank-Nicloson method for large number of iterations. To extract the elements of the S matrix from the time-dependent wave function we have tested three different methods on the electron-molecule collision models and all results for energies of interest are in a perfect agreement with the cross sections obtained within the time-independent framework. The correlation function method was also tested on the model of the dissociative recombination.

The results of the low-energy electron collisions with diatomic molecules provided a deep insight into the model dynamics and enabled us to find out the origin of all structures in the vibrational excitation cross sections, discussed in details in Sec. 3.4. For real systems one could perform similar time-dependent calculations within the local complex potential approximation or the nonlocal resonance model and thus interpret the results in the same way. As we have shown, the vibrational excitation cross sections for diatomic molecules quite often result from several contributions separated in time and their shape is given by the interference between these contributions. More importantly the asymmetrical shapes in the cross sections are produced by more than two contributions, thus the terms *boomerang motion* and *boomerang oscillations* are not quite accurate. The terms *oscillatory motion* and *oscillatory structure* are in this context more appropriate.

The results of the dissociative recombination model for the H_2^+ cation provides a deep insight into the dynamics of the indirect mechanism of the dissociative recombination process. The results confirm the proposition that the most populated final state is in the highest possible dissociative recombination channel accessible for the given electron energy. The results also provide the explanation of the many observed structures in the cross sections and allow the identification of the resonant structures with corresponding quasi-bound states, discussed in Sec. 4.3. The time-dependent approach to the model dynamics of the dissociative recombination model reveals the presence of long-living states or presence of paired states between which the system oscillates for very long time.

As we have shown in Sec. 4.3 the observation of the Rydberg states population during the evolution allowed us to interpret the recombination process as *multiply indirect* mechanism, i.e. as dissociative recombination through repeated transitions between many quasi-bound states in the Rydberg electronic potentials. This interpretation also partially confirms the proposed *ladder mechanism* (see Sec. 4.3 for details).

The results of both time-independent and time-dependent approach to the dissociative recombination model dynamics allowed us to observe the populations of the final states for the first time within theoretical calculations. As a result we may confirm that the highest recombination channel possible for a given energy of the incoming electron is also the most populated channel, which is in agreement

with general experiments, e.g. measurements of the dissociative recombination with LiH^+ by Krohn et al. [2001].

The results of the dissociative recombination model of H_2^+ will serve as a benchmark for testing the approximative methods and are currently being prepared for publication in collaboration with the group of R. Čurík, where they will be compared to the results of the frame transformation approximation.

Bibliography

M Abramowitz and I. Stegun. *Handbook of Mathematical Functions with Formulas, Graphs, and Mathematical Tables*. Dover Publications, New York, 1972.

M. Allan. Experimental observation of structures in the energy dependence of vibrational excitation in H_2 by electron impact in the $^2\Sigma_u^+$ resonance region. *Journal of Physics B*, 18:4511–4517, 1985.

M. Allan. Near-threshold vibrational excitation and elastic electron scattering from N_2. *Journal of Physics B*, 38:3655–3672, 2005a.

M. Allan. Electron collisions with NO: elastic scattering, vibrational excitation and $^2\Pi_{1/2} \rightleftharpoons ^2\Pi_{3/2}$ transitions. *Journal of Physics B*, 38:603–614, 2005b.

M. Berman, M. Estrada, L. S. Cederbaum, and W. Domcke. Nuclear dynamics in resonant electron-molecule scattering beyond the local approximation: The 2.3-eV shape resonance in N_2. *Physical Review A*, 28:1363–1381, 1983.

D. T. Birtwistle and A. Herzenberg. Vibrational excitation of N_2 by resonance scattering of electrons. *Journal of Physics B*, 4:53–70, 1971.

E. S. Chang and U. Fano. Theory of electron-molecule collisions by frame transformations. *Physical Review A*, 6:173–185, 1972.

W. Domcke. Theory of resonance and threshold effects in electron-molecule collisions: The projection-operator approach. *Physics Reports*, 208:97, 1991.

L. Dubé and A. Herzenberg. Absolute cross sections from the "boomerang model" for resonant electron-molecule scattering. *Physical Review A*, 20:194–213, 1979.

The Editors. Editorial: Uncertainty estimates. *Physical Review A*, 83:040001, 2011.

A. I. Florescu-Mitchell and J. B. A. Mitchell. Dissociative recombination. *Physics Reports*, 430:277–374, 2006.

M. Formánek, M. Váňa, and K. Houfek. Efficient numerical solution of coupled radial differential equations in multichannel scattering problems. *AIP Conference proceedings*, 1281:667, 2010.

E. L. Hamilton. *Photoionization, Photodissociation, and Long-Range Bond Formation in Molecular Rydberg States*. PhD thesis, University of Colorado, Boulder, 2003.

A. Herzenberg. Oscillatory energy dependence of resonant electron-molecule scattering. *Journal of Physics B*, 1:548–558, 1968.

J. Horáček, M. Čížek, K. Houfek, P. Kolorenč, and W. Domcke. Dissociative electron attachment and vibrational excitation of H_2 by low-energy electrons: Calculations based on an improved nonlocal resonance model. II. vibrational excitation. *Physical Review A*, 73:022701, 2006.

K. Houfek, T. N. Rescigno, and C. W. McCurdy. Numerically solvable model for resonant collisions of electrons with diatomic molecules. *Physical Review A*, 73:03721, 2006.

K. Houfek, T. N. Rescigno, and C. W. McCurdy. Probing the nonlocal approximation to resonant collisions of electrons with diatomic molecules. *Physical Review A*, 77:012710, 2008a.

K. Houfek, M. Čížek, and J. Horáček. On irregular oscillatory structures in resonant vibrational excitation cross-sections in diatomic molecules. *Chemical Physics*, 347:250–256, 2008b.

W. M. Huo, M. A. P. Lima, T. L. Gibson, and V. McKoy. Correlation effects in elastic e-N_2 scattering. *Physical Revue A*, 36:1642–1648, 1987.

D. Hvizdoš. Two-dimensional model of dissociative recombination. Master's thesis, Charles University in Prague, 2016.

C. Johnson. *Numerical solutions of partial differential equations by the finite element method*. Cambridge University Press, The Pitt Building, Trumpington Street, Cambridge CB2 1RP, 1987.

S. Krohn, M. Lange, M. Grieser, L. Knoll, H. Kreckel, J. Levin, R. Repnow, D. Schwalm, R. Wester, P. Witte, A. Wolf, and D. Zajfman. Rate coefficients and final states for the dissociative recombination of LiH^+. *Physical Review Letters*, 86:4005, 2001.

M. Larsson and A. E. Orel. *Dissociative Recombination of molecular ions*. Cambridge University Press, The Edinburgh Building, Cambridge CB2 8RU, UK, 2008.

C. W. McCurdy and C. K. Stroud. Eliminating wavepacket reflection from grid boundaries. *Computer Physics Communications*, 63:323–330, 1991.

C. W. McCurdy, M. Baertschy, and T. N. Rescigno. Solving the three-body coulomb breakup problem using exterior complex scaling. *Journal of Physics B*, 37:R137, 2004.

T. N. Rescigno and C. W. McCurdy. Numerical grid methods for quantum-mechanical scattering problems. *Physical Review A*, 62:032706, 2000.

Shandilya, Sarma, Adhikari, and Mishra. Time dependent wave packet treatment of $^2\Pi_g N_2^-$ and $^3\Sigma^- NO^-$ shape resonances using two-dimensional surfaces for electron-N_2 and NO interactions. *International Journal of Quantum Chemistry*, 113:130, 2012.

D. Tannor and D. E. Weeks. Wave packet correlation function formulation of scattering: The quantum analog of classical S-matrix theory. *Journal of Chemical Physics*, 98:3884, 1993.

J. R. Taylor. *Scattering Theory: The Quantum Theory on Nonrelativistic Collisions*. University of Colorado, Wiley & Sons Inc., New York, 1991.

I. J. Thompson and A. R. Barnett. Coulcc: A continued-fraction algorithm for Coulomb functions of complex order with complex arguments. *Computer Physics Communications*, 36:363–372, 1985.

J. S. Townsend and V. A. Bailey. The motion of electrons in argon and hydrogen. *Philosophical Magazine*, 44:1033–52, 1922.

C. S. Trevisan, K. Houfek, Z. Zhang, A. E. Orel, C. W. McCurdy, and T. N. Rescigno. Nonlocal model of dissociative electron attachment and vibrational excitation of NO. *Physical Revue A*, 71:052714, 2005.

W. van Dijk and F. M. Toyama. Accurate numerical solutions of the time-dependent Schrödinger equation. *Physical Review E*, 75:036707, 2007.

M. Váňa and K. Houfek. Time-dependent formulation of the two-dimensional model of resonant electron collisions with diatomic molecules and interpretation of the vibrational excitation cross sections. *Physical Review A*, 95:022714, 2017.

R. Čurík and P. Čársky. *Low-Energy Electron Scattering from Molecules, Biomolecules and Surfaces*. CRC Press, Boca Raton, 2012.

List of Abbreviations

VE Vibrational excitation.

DA Dissociative Attachment.

DR Dissociative Recombination.

FEM Finite Element Method.

DVR Discrete Variable Representation.

ECS Exterior Complex scaling.

Attachments

Attachment 1. N2_complex.mp4 A short animation showing the evolution of the full 2D complex wave function in the interaction region of the N_2-like model. The wave function is displayed using the complex plane mapping to HSV color space described in Sec. 2.6, with inverted radial mapping. The molecule is initially in the ground state, i.e. the system incident wave function comes from the $v_i = 0$ vibrational excitation (VE) channel.

Attachment 2. N2_cs_formation.mp4 An animation showing multiple quantities determined from the evolution of two-dimensional model of N_2-like system starting from the initial ground state of the molecule (i.e. $v_i = 0$). The top left panel shows the mean internuclear distance of the projection onto the discrete state (see the paper for details). The dotted line marks the position in time. The bottom left panel shows the two-dimensional probability distribution given by the complex wave function (Att. 1). Note that the z-axis is rescaled multiple times during the evolution as visible on the z-axis tics. The rest of the panels shows the current state of the VE cross sections integrated up to the given time, i.e. the contribution of the part of the wave function which already left the real part of the two-dimensional discretization grid. The forming of the structures in the cross sections is nicely visible in all channels.

Attachment 3. NO_complex.mp4 An animation showing the evolution of two-dimensional complex wave function within the NO-like model displayed through HSV mapping from Sec. 2.6, with inverted radial scale. The molecule is initially in the vibrational ground state, i.e. $v_i = 0$.

Attachment 4. NO_cs_formation.mp4 An animation showing multiple quantities from the evolution of two-dimensional model of NO-like system starting from initial ground state of the molecule (i.e. $v_i = 0$). The top left panel shows the mean internuclear distance of the projection onto the discrete state of the system. The dotted line marks the position in time. The bottom left panel shows the two-dimensional probability distribution given by the complex wave function (Att. 3). Note that the z-axis is rescaled multiple times during the evolution as visible on the z-axis tics. The rest of the panels shows the current state of the VE cross sections integrated up to the given time, i.e. the contribution of the part of the wave function which already left the real part of the two-dimensional discretization grid. The forming of the structures in the cross sections is nicely visible in all channels.

Attachment 5. F2_coplex.mp4 An animation showing the evolution of two-dimensional complex wave function within the F_2-like model displayed through HSV mapping from Sec. 2.6, with inverted radial scale. The molecule is initially in the vibrational ground state, i.e. $v_i = 0$.

Attachment 6. H2p_complex.mp4 An animation showing the evolution of two-dimensional complex wave function within the H_2^+-like model of dissociative recombination displayed through HSV mapping from Sec. 2.6, with inverted radial

scale. The molecular cation is initially in the vibrational ground state, i.e. $v_i = 0$.